UNIVERSITAT DE BARCELONA

Noise-correlation force spectroscopy in molecules and cells

Marta Gironella Torrent

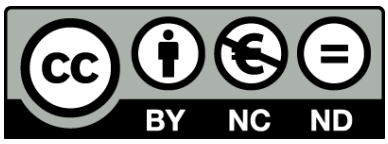

Tesi doctoral:

NOISE-CORRELATION FORCE SPECTROSCOPY IN MOLECULES AND CELLS

Marta Gironella Torrent

UNIVERSITAT DE BARCELONA

NOISE-CORRELATION FORCE SPECTROSCOPY IN MOLECULES AND CELLS

Memòria presentada per optar al grau de doctora per la

Universitat de Barcelona

Programa de doctorat en Física

Marta Gironella Torrent

Director:
Fèlix Ritort Farran

Tutor:
Giancarlo Franzese

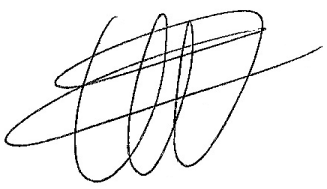

Dedicat a
La Montse i al camí que he recorregut amb ella

Agraïments

Aquesta tesis ha representat cinc llargs, i molt intensos, anys de la meva vida i encara em costa fer-me a l'idea de que ja s'està acabant. Ha estat un camí ple d'obstacles i aventures el qual he tingut la immensa sort de compartir amb desenes de persones meravelloses a les quals els hi dedico aquest apartat. En primer lloc, gràcies al meu supervisor/director de tesis, Fèlix Ritort, per la seva entrega absoluta a la recerca, el seu entusiasme inesgotable i la seva curiositat infinita. Quan en aquell últim any del grau de física vaig escollir l'assignatura de Biofísica, no em podria imaginar pas tot el què representaria per mi. Jo estava molt perduda respecte el què volia fer després del grau, però varen fer falta poques classes perquè, la seva passió explicant com la termodinàmica, la mecànica de fluids, la mecànica clàssica i l'electromagnetisme, es combinen en una sola disciplina capaç d'explicar els mecanismes que donen lloc a la vida, m'impactes de forma irreversible. Des d'aquella assignatura he tingut clar que la Biofísica més enllà d'una assignatura és una manera de veure el món i viure la vida, em fa feliç. Moltes gràcies Fèlix per fer-ho possible, de tot cor.

En segon lloc, a tota la gent que ha passat per l'SmallBioSystems Lab durant aquests últims sis anys, aquesta família estranya i disfuncional amb un cor enorme. Intentaré anar per ordre cronològic. En primer lloc vull agrair a l'Anna Alemany les classes de problemes de mecànica de segon any del grau de física, quan encara no tenia ni idea de què era la Biofísica. Entre 2011 i 2015, les noies érem aproximadament un 20% de l'alumnat, i el percentatge del professorat era igual o pitjor. Llavors, era difícil identificar-se amb alguna professora, i encara més, veure't en un futur com a catedràtica amb tants pocs referents (continua essent difícil a dia d'avui). L'Anna va ser la primera professora amb qui em vaig identificar, la primera que em va fer pensar

que la carrera acadèmica podria ser una opció per a mi. Qui m'havia de dir que dos anys més tard estaria seguint els seus passos ocupant el que va ser el seu despatx! Gràcies també a en Joan Camuñas, el qual, igual que l'Anna, ja estava en la recta final de la seva tesis quan jo vaig arribar al laboratori. Els inicis sempre són intensos, recordo les meves primeres vegades amb les optical tweezers intentant atrapar beads sense aconseguir-ho, només veient ombres massa ràpides en la immensitat grisa de la càmera microfluídica. El sentiment de frustració és elevat i no sempre fàcil de gestionar. Per aquest motiu, i amb perspectiva, agraeixo infinitamnet a totes les persones que s'han pres el seu temps per ajudar-me en els meus inicis. En particular recordo que en Joan va ser clau en unes mesures amb la bomba de flux un divendres a altes hores de la tarda. Merci Joan! M'és difícil començar a parlar d'en Marco Ribezzi, ja que li tinc un apreci profund d'aquells que són de per vida. Ell va ser el meu postdoc durant els meus primers sis mesos al laboratori. Recordo clarament que al principi pensava que jo no li queia bé, a les reunions sempre estava molt seriós i les seves contestacions eren força seques. A més a més, era molt exigent i a vegades tenia la sensació de que els resultats que li presentava no li agradaven tot i que no m'ho digues directament. Amb el temps vaig anar veient que, conscient o inconscientment, m'estava preparant per poder ser autònoma i ser capaç de lidiar amb les reunions amb en Fèlix jo sola, ja que ell se n'aniria a París. Gràcies a ell vaig aprendre molt ràpid a defensar el què creia que era correcte, a presentar els resultats d'una forma clara i entenedora, i a ser independent a l'hora de decidir quins experiments són més interessant que uns altres per un determinat projecte. Quan se'n va anar el vaig trobar a faltar molt, però ja estava preparada per seguir la meva tesis amb confiança.

Quan ells van marxar, el laboratori es va quedar una mica buit, però ràpidament van arribar altres persones que el van omplir amb molt de cor i bon rotllo durant una sempre massa curta temporada. Em refereixo a la Carmina, l'Aurelien, en Vegard, en Fabio, la Carla, en Teo, la Laura, l'Aleix i en Javi. La Carmina, sense ella, l'estiu de 2017 hagués sigut molt pitjor del que va ser. Recordaré sempre estrenar al pis de Sants amb tu sense aigua ni electricitat, aquelles dues setmanes varen ser com estar de colònies amb una amiga. Gràcies per les xerrades, per l'spinning a les 7 del matí, per les "risas", per les festes, per la Magdalena i per tot, et desitjo el bo i millor ara i

sempre. L'Aurelien, el Salvador Dalí Junior amb qui vaig provar la millor "fondue" i amb qui discutir sempre era un plaer. En Vegard, amb el qual varem aprendre a fer esquí de muntanya a Noruega mentre ens relaxàvem al "hot tube" a la nit i el qual va tarda un mes a saludar-nos pel passadís perquè: com ens havia de saludar si no ens coneixia? A en Fabio, per regalar-me sempre un somriure d'orella a orella i estar disposat a afogar les penes en qualsevol moment. A la Carla, per les hores interminables fent càmeres de PROSEQO amb bon rotllo sense perdre l'esperança. A en Teo, per redescobrir les pinces tot comentant capítols de Suits. A la Laura, per la seva energia positiva i per veure el got sempre mig ple. A l'Aleix i en Javi, per ser uns nois meravellosos sempre disposats a donar una mà a qui fes falta.

Als meus companys de despatx. A l'Àlvaro, per la confiança tot i ser persones tant diferents, per les discussions argumentades des del respecte, però sobretot per poder compartir les coses que no són tant fàcils i sentir el suport en els moments complicats. Ha estat un plaer enorme compartir una part d'aquesta etapa amb tu. T'envio una abraçada ben gran. A en Marc, per rebre'm amb afecte quan començava al laboratori i tot era un xic difícil, pels riures i per els nostres blancs i negres que mai són grisos. A en Paolo, que ha arribat més tard però que és tot cor i bona fé i que sempre transmet calma i tranquil·litat. Grazie mille!

Als companys de l'SmallBiosystems Lab. A en Xavi, per ser el meu suport principal a Barcelona, a Padova i a la Xina, per totes les converses, per els beer o'clock dels divendres, per les festes a Plataforma, per les calçotades al més pur estil Age of Empires, per les esquerres i l'anarquia. Et mereixes el bo i millor cuki, no ho oblidis mai. A en Jaime/Jaume, per ser una persona meravellosa amb un cor enorme tot i que de vegades l'enterri en un catastrofisme apocalíptic, pel teu compromís amb la docència universitària i les condicions laborals de la vida acadèmica, per la teva dignitat en defensar el que creus que està bé i per està allà en els moments complicats. No tinc cap dubte que t'esperen grans coses i que tots necessitem més persones com tu al voltant. Per l'Alejandro, que acaba de començar però que amb la seva tenacitat arribarà molt lluny. Molts d'ànims! A l'Isabel, per provar la gastronomia espanyola a través de les Jornades CIBER-BBN, pels consells i per les converses sobre el futur i la recerca. A la Maria, pel maleït PROSEQO, per les xerrades des de l'afecte, per tenir una visió

de la recerca i de les prioritats divergent la qual crec imprescindible perquè la carrera acadèmica sigui sostenible.

A les persones de dinars condensats, Joan, Carlos, Mariona i Elis. En especial gràcies a en Joan per recordar-se sempre del meu aniversari i fer-me pensar que també és el seu. Gràcies a la Mariona per les discussions sempre interessants sobre activisme, per un coneixement bàsic de llengua dels signes i, sobretot, per ajudar-me amb la mudança, igual que l'Elis i en Xavi, no sé com encara em parleu, espero haver-vos subornat correctament amb el què tenia. Gràcies de tot cor.

A tota la gent que ha format part d'aquesta estada a Padova. Primerament, i en lloc molt important, l'Anna Maria. Gràcies per ser una cuki de cap a peus, per els anàlisis infinits de les Lorentzianes, per ser una "currante" i per haver fet possible aquesta estada. Ha sigut una experiència meravellosa de la qual em sento infinitament agraïda. A la Chiara, per els spritzs, els mezo-mezo, les birres i els tramezini a l'Amici, per les converses profundes i sinceres de temes complicats que no pots tenir amb tothom. Et desitjo el bo i millor, ara i sempre. A la Linda, la Bolognese més agradable i simpàtica que he conegut mai, gràcies per la conversa fàcil i fluida, per les rialles i les passejades per Padova després de la feina. A en Giulio, per la seva amabilitat, per fer-me sentir part del grup des del minut zero, i perquè ens queda pendent una nit de jocs de taula asimètrics (que m'has d'explicar què significa perquè no ho sé). A la Paola i a en Mateo, per els aperitivos al Giardini dell'Arena i les rialles. A en Giacomo, per la visita guiada al taller mecànic de prototips i els farts de riure a l'Amici. A la Sílvia, per les converses existencials i perquè trobis el teu lloc allà on tu escullis. A l'Ivan, per l'etern projecte de les variances, per les discussions, la paciència i l'entusiasme. I per últim, a la propia ciutat de Padova que m'ha recollit amb afecte i m'ha donat l'espai i el temps per retrobar-me a mi mateixa entre el soroll.

A les persones que m'han acompanyat en la meva vida universitària anterior al doctorat però sense les quals hagués estat tot més avorrit. A la Hiza, per aquell primer any de grau intens i convuls. A en David Royo, l'Enric, en Jordi i en Sospi, per fer de les nostres desgràcies somriures en aquells quatre anys eterns de grau, pels festivals de primavera i per remar tots junts en la mateixa direcció. Als meus companys de Màster de Advanced Physics, Laia, Manuel, Jonas, Sergi i Carlo, per els nostres sopars italians, les nostres bir-

res després de classe per compartir les penes dels treballs infinits poc proporcionals a la carrega de certes assignatures, per les derivacions eternes, per els estats de l'aigua, per les simulacions Monte Carlo i per aquella nit de micro obert que ens vam marcar en aquell bar del Raval on vam deixar a tothom amb la boca oberta.

A les meves magnífiques companyes de futbol amb les quals vam guanyar el campionat europeu de futbol 7 al setembre del 2018, vam participar al Mundial de futbol 7 a Curitiba, Brasil, al desembre del 2018 i vam guanyar el campionat internacional Marco Polo a Roma, Itàlia, a l'Estiu de 2019. A la Julià, per ser la millor portera del món i, tot i així, voler-me a la seva línia defensiva, per el sushi i totes les festes a la Fira. A la Carla, per introduir-me al món de Celebreak que m'ha aportat tantíssim, per ser una persona preciosa amb un cor que no li cap al pit, per les teves abraçades que ho curen tot, et mereixes totes les coses meravelloses que et passin. A l'Indi, pel "petardeo" i per ser una companya 10 tant dins del camp com fora. A la Lana, per les converses de vegades massa sinceres i per els partit de futbol femení. A l'Assiri, per orientar-me una mica a la lliga mixta quan no recordava ni com xutar una pilota i per ser una companya en defensa fenomenal. A la Clara, per ser una persona 10, com la seva "prima" l'Indi, per ser la millor defensa central i perquè ens poguem tornar a veure molt aviat. A la Louise, per ser la personificació del somriure i de la motivació i per tirar del carro sempre que faci falta. A la Brit, per ajuntar-nos a totes en aquell cap de setmana estrany de setembre i fer possible tota aquesta aventura. A la Belen i a la Maria per ser les millors centrecampistes de futbol sala convertides a futbol 7 que he vist mai. A la Sandra i la Natalia per ser unes fenomenes amb majúscules. A la Nikkita, la Sonja, la Rikkie, la Dana, la Linnéa, per formar part d'aquesta aventura quan els hi ha sigut possible.

A les companyes del Bàsquet Vilafant per fer d'aquesta recta final un camí més planer i per acompanyar-me en el retrobament d'aquest esport que estimo tant.

Als de Londres amb qui vaig compartir un viatge únic i inoblidable. A la Maria, per ser una de les dones més intel·ligents, curioses i observadores que conec, per els seus whatsapp aleatoris després de segles sense parlar fent preguntes importantíssimes sobre temes invisibilitzats. A en Max, per estimular la meva lògica com ningú parlant de qualsevol tema quotidià o transcendental, per les visites guiades a

Sant Pere de Rodes, per les discussions filosòfiques i per introduir-me, a mi i a molts, al complexe món d'Alexandre Deulofeu. A l'Àdria, per les passejades per Barcelona al primer any de carrera quan tot era nou i incert, per la seva transparència i valentia en expressar els seus sentiments.

A totes les persones que he conegut a congressos i m'han aportat tant científica com personalment. En especial al merevellos grup que vam fer a París, França, al novembre del 2016 i a la triple M que vam crear a Aspen, Colorado, EE.UU, al gener del 2019. Desitjo que tots vosaltres estigueu bé.

A totes les persones amb qui vaig compartir els quatre anys als Col·legis Majors Universitaris (CMU). En especial al grupet Opera Singers: Ari, Cèlia, Selin, Carme, Roser i Inés, gràcies per les "pizza parties", per tots els dinars i sopars juntes, per Ses Verges, per els carnavals, per les hores infinites d'estudi a la Biblioteca i per ser unes amigues magnífiques. A l'Idoia, per els projectes al PenyaLab, per totes les converses existencials, per tots els merders, per tots els plors i les rialles, per els concerts de piano, per les partides al ping-pong amb el "mosquetier", perquè estàs com una cabra i, sobretot, perquè amb tu, u més u fan més que dos. A l'Alex, per ser un amic meravellós, pacient, sempre disposat a escoltar, afectuós i amable, per els nostres inicis accidentats, però encara més per l'amistat que en va néixer, per els estius a Mallorca i a l'Empordà, per els billars durant exàmens finals, per les partides conjuntes a "Zombis VS Plantes" després de la lesió de turmell, per la sinceritat tot i que no sigui agradable, perquè t'estimo molt i tenir-te a la meva vida és un regal. A en Marc, per ser una persona genial en tots els sentits, per la passió que posa a tot el què fa, per les seves conviccions i la seva concepció de justícia, per la seva coherència i entrega, perquè les converses amb tu sempre expandeixen el temps. A en Xavi, per ser el millor mentor del món, per la seva motivació màxima en els projectes, pels seus "caxarritus" útils que canvien vides, per haver-me donat l'oportunitat de treballar colze a colze amb l'Idoia, pels correus aleatoris posant-nos al dia sempre amb el degut rigor científic i perquè ets una persona meravellosa a qui la providència ha tingut el gran detall de posar en el meu camí. I finalment, a la persona que, a través del seu lideratge, ha fet possible la creació d'aquest espai tant ric i ple d'oportunitats que són els CMU, la seva directora, Montse Lavado. Et vull expressar el meu sincer

i profund agraïment per la teva confiança en mi, per les converses que m'han permès veure els grisos entre els extrems, per les persones increïbles que he conegut gràcies a la teva feina i entrega i per poder considerar-te una referent, però sobretot, una amiga.

A la Comissió d'Igualtat dels CMU, en present, per la feina imprescindible que realitzeu, però sobretot en passat, en els seus inicis, per fer-m'hi particip. Gràcies Miquel i Mireia, per el vostre compromís per revolucionar el vostre entorn, per l'iniciativa i per l'entrega. A la Laura i l'Àngela, pel relleu i les noves perspectives tant necessàries. A la Comissió de Protocol, la Nerea, la Natàlia i la Júlia, per les vostres ganes de crear espais segurs dins dels CMU, per les hores i hores d'skypes als caps de setmana pensant i repensant en totes les possibilitats, per posar-hi el cor, que no sempre és fàcil.

A l'Assamblea feminista de la UB, per la seva feina magnífica i absolutament necessària, per el cor i l'energia que hi posa cadascuna de les persones que en formen part. A l'associació AMIT, pel seu compromís amb la visibilització de la dona en la ciència i per crear un espai de trobada en terrenys tant àrids.

A l'associació Alumni Penyafort-Montserrat-Llull, en espacial als membres de la primer junta amb qui he compartit aquesta gran aventura: Joana, Pep, Fernando, Mª Luisa, Xavi, Abel i Cuca. Moltes gràcies per estimar als Col·legis tant com ho feu i per dedicar el vostre temps de forma desinteressada a retrobar aquesta gran família d'antics col·legials. També voldria fer una menció especial a la Marta Anton, que va fer possible el programa de mentoratge SteMatEsElla el qual em va obrir tantes portes i em va posar en contacte amb dones extraordinàries. Com la meva mentora, Mònica Espinosa, a qui li agraeixo els cafès, els consells i els ànims per poder arribar on em proposi. O com l'Anna Mentuy, gràcies a la seva xerrada inspiradora vaig ser capaç d'obrir horitzons al meu futur professional més enllà del món acadèmic.

A la família que jo he escollit. A la Laura, per ser una de les persones més importants a la meva vida, per conèixer-me com ningú, per veure la meva llum i la meva foscor i, tot i així, quedar-se al meu costat, perquè sempre puc comptar amb tu i perquè t'estimo més enllà del que puc expressar amb paraules. A la Nora, per un dels millors estius de la meva vida, per la nostra historia complicada però que no s'ha trencat en cap moment, per les nostres cerveses del dilluns desit-

jant que ja sigui divendres, per les pelis clàssiques que no sé com no conec, per l'amor i cura que poses a tot el que fas tot i que el més important, recorda, sempre ets tu, i pels infinits moments màgics que sé que ens queden per viure juntes. T'estimo moltíssim. A en Francesc, o xof, o xemeneia, per tot el què hem viscut, per els inicis accidentats i difícils, per la teva perseverança que t'ha portat on ets ara, per el teu afecta que m'ha acompanyat en moments increïblement durs i perquè espero que segueixis al meu costat tant temps com sigui possible, una abraçada enorme. A l'Elisa, per retrobar-nos després de tant de temps, per el whatsapp que mai m'hagués pensat que m'enviaries, i per seguir compartint amb tu d'ara en endavant. A l'Alex G., per els nostres sopars de "gordos", per la Mercé, pels cinemes a la fresca, pels mamuts, per Estocolm i per les nostres abraçades trenca costelles, espero que tot es vagi meravellosament bé, t'ho mereixes tot. A la Carla, per aquell 15M dormint a la Rambla de Figueres a la nostra tenda batejada com a "Pituflina", per les patates fregides plenes d'amor a Garriguella juntament amb els plats d'embotits i formatges de la Cooperativa, pel BangBang amb moscatell, per les visites a Leeds i per seguir rient i gaudint de la vida com només nosaltres ho sabem fer. T'estimo bonica.

A la meva germana, per més concerts de Tribade amb tu, per les nits de pizza/entrepà i cervesa al pis de Collblanc i perquè ens mereixem el bo i millor ara i sempre, perquè t'estimo com a ningú i perquè una de les coses que més desitjo en aquesta vida és que siguis feliç. Al meu pare, per el seu afecte desinteressat i sincer i per acceptarme tal com sóc en tot moment. A la meva mare, per llegir-me tots els llibres de la biblioteca de Figueres quan era una nena, per tots els reptes intel·lectuals que m'ha ofert i que m'han ensenyat a gaudir de la lògica i la deducció, i sense els quals avui no estaria on estic. A la meva tia Fina, per les partides a les dames, per els panets torrats, per les croquetes de carn i per aquest amor genuí que poses a tot el què fas. A la meva padrina Roser, per ser una de les dones més intel·ligents que conec i que segur que, si hagués pogut accedir a la universitat, no seria jo la primera de la família en doctorar-me. Us estimo molt i sempre us portaré amb mi.

A la Gina, la meva companya de vida, pel nostre camí juntes, que no ha sigut gens fàcil però que ha valgut cadascun dels k_BT invertits, per la nostra sinceritat i valentia, per el nostre compromís amb una

mateixa i perquè seguim descobrint noves i millors maneres d'estimar-nos. Et porto al cor.

Finalment a la meva terapeuta, Montserrat Crehuet, a qui està especialment dedicada aquesta tesis. Per visibilitzar la salut mental com quelcom fonamental, sobretot en entorns tant competitius i estressants com el món acadèmic. Necessitaria un llibre sencer per agrair-te l'acompanyament en aquest camí tant complicat que és conèixer-se a una mateixa, espero que t'arribi el meu profund i sincer agraïment per tots aquests anys compartits. Sense ells, aquesta tesis no hauria estat possible. Gràcies de tot cor.

Agosto 2021, Padova

Resum de la Tesis en català

Aquesta tesis tracta de l'estudi experimental i teòric de les fluctuacions en molècules d'ADN de cadena doble (dsDNA) i de glòbuls vermells (GV). La tesi introdueix l'espectroscopia de mesures de soroll utilitzant pinces òptiques, com una metodologia experimental per caracteritzar processos biofísics en sistemes moleculars i cel·lulars.

La primera part de la tesis es concentra en les propietats mecàniques i els processos de fora de l'equilibri dels GV. A través de mesures actives (aplicant perturvacions externes) i passives (espectres de potències en condicions estacionàries), s'estudien els processos de relaxació i dissipatius dels GV. Pel què fa als processos de relaxació, el GV presenta tres escales de temps diferenciades que relacionem amb les diferents parts de la cèl·lula (membrana lipídica i xarxa bidimensional d'espectrina i actina). Per altre banda, la mesura de les fluctuacions de membrana dels GV, ens permet mesurar l'activitat (energia dissipada) del GV. Les dades experimentals de mesures actives són reproduïdes modelitzant el GV a través d'un model de reologia de sistemes tous.

La segona part de la tesi consisteix en la demostració experimental d'una nova relació de fluctuacions, que a diferència del teorema de fluctuació-dissipació, es calcula a través de mesures únicament passives. Aquesta relació és vàlida per sistemes en estats estacionaris de no equilibri subjectes a qualsevl tipus de potencial (no necessariament quadràtics). Fins ara, les relacions analítiques publicades respecte a la producció d'entropia són límits inferiors d'aquesta. Per primera vegada, la relació presentada en aquesta tesis dona lloc a dos límits superiors per a la producció d'entropia. Aquesta relació és verifica experimentalment per a diferents sistemes i aporta una nova metodologia per calcular la producció d'entropia de sistemes fora de l'equilibri.

La tercera part de la tesi estudia l'acoblament torsió-deformació de molècules de dsDNA a través de mesures passives d'espectroscopia

de forces. Aquest estudi es basa en la caracterització de l'espectre de potències interpretat a través del model de barra elàstica del qual el model cucoide (worm-like chain en anglés) és un cas particular. Aquest estudi permet observar una dependència del mòdul de deformació respecte a la longitud de contorn de la molecula estudiada, essent més petit com més curta és la molècula. Finalment, introduïm per primera vegada la idea de que aquest efecte podria estar relacionat amb una dependència de l'acoblament torsió-deformació respecte la longitud molecular.

Objectives of the thesis

In 1827, botanist Robert Brown observed the motion of pollen grains suspended in water under a microscope. Although he thought their motion was life-related, we now know that these pollen grains were not much alive. In fact, the pollen grains motion was caused by the constant impact of the water molecules. This effect is commonly known as thermal fluctuations, and leads to random deviations from the average state. We observe these deviations in small systems where energies are on the same order than the bath energy scale ($\sim k_B T$).

In contrast to the pollen grains, living systems normally operate out of equilibrium as there is a net exchange of energy and matter with the environment. One of the most challenging issues in the field of nonequilibrium biophysics is the quantification of how far from equilibrium life is. Physicists address this question by measuring the rate of entropy production which is defined as the rate at which the system dissipates energy to the environment.

It is crucial to distinguish between passive fluctuations and active fluctuations due to life processes as for example metabolic processes, molecular motors activity, cell motility, etc.

From an experimental point of view, passive fluctuations from the environment are related to energy exchange processes operating at short times, while active fluctuations operates by the concert of many molecular processes and show higher characteristic timescales. In equilibrium, the fluctuation-dissipation theorem (FDT) holds. The FDT states that dissipation is the natural consequence of fluctuations. In other words, system's relaxation after a passive spontaneous fluctuation cannot be distinguished from system's relaxation after an active external perturbation (Onsager dix(t)). For example, in the pollen grains case, the friction with water dissipates heat at a rate equal to the kinetic energy rate delivered to the grains by the Brownian motion

of the water molecules.

Besides FDT, the study of the power spectrum of the signal is a useful tool to discriminate thermal from active fluctuations. THe measurements of fluctuations in frequency space is useful to distinguish processes with different timescales.

In the present thesis, we use Laser Optical Tweezers (LOT) to measure fluctuations of molecular constructs (dsDNA molecules and DNA hairpins) and red blood cells. LOT have the advantage of a high resolution in both displacement ($\sim$ 1nm) and force ($\sim$ 0.1pN), being versatile to perform experiments in molecular and cellular systems.

Fluctuations measurements depend on the experimental configuration, the number of elements involved in the system and how these are connected. In the LOT setup, a bead is used as a probe that is attached to the system of interest. For the DNA constructs, the bead is attached to a dsDNA handle which is linked to the DNA molecule. For red blood cells, the bead is directly attached to the RBC membrane. In both cases two are the contributions to the fluctuations: the bead in the optical trap and the system of interest.

Therefore, we aim that noise-correlation measurements are a powerful and precise tool to obtain valuable physical quantities (friction coefficients, molecular and cellular stiffness, nonequilibrium effective temperatures, entropy production rates etc.) quantifying nonequilibrium processes in living matter.

Contents

List of Figures

List of Tables

Part I

Introduction

Chapter 1

Molecular and Cellular Biophysics

Erwin Schrödinger (1887-1961), an Austrian physicist who shared the Nobel Prize with Paul Dirac for their ground-breaking insights in quantum mechanics, wrote a small book in 1944 under the title *What is life?*. This book was a summary of a course of public lectures aimed to answer the following question: *How can the events in space and time which take place within the spatial boundary of a living organism be accounted for by physics and chemistry?* [1]. In this book, E. Schrödinger advanced a simple and powerful hypothesis about the molecular structure of genes. This hypothesis inspired many biologists to think about genetics in innovative ways, consolidating molecular biology. However, all the amazing discoveries of the following decades were not enough to fully understand and answer Schrödinger's question. In words of Sydney Brenner, one of the most important molecular biologists in the 20th century: *I think in the next twenty-five years (after the sixties) we are going to have to teach biologists another language still. I don't know what it's called yet; nobody knows. But what one is aiming at, I think, is the fundamental problem of the theory of elaborate systems. Especially, elaborate systems that arise under conditions of natural selection. And here there is a grave problem of levels: it may be wrong to believe that all the logic is at the molecular level. We may need to get beyond the clock mechanisms* [2].

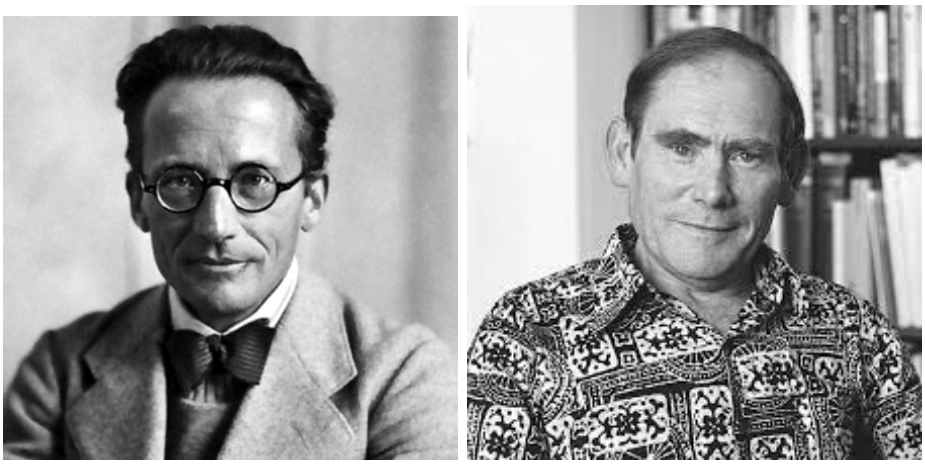

Figure 1.1: (**a**) Erwin Schrödinger (**b**) Sydney Brenner.

Indeed, new disciplines had appeared in order to explain the high complexity of living systems as non-linear dynamics, network dynamics, complexity theory, theory of dynamical systems etc. [3] giving place to concepts as dissipative structures, self-organization, or chaotic attractors. All these new perspectives arise to understand the mechanisms underlying living matter and, somehow, we could group them under the general term of Biophysics.

Biophysics is an interdisciplinary science that studies biological processes and structures from a physics point of view. It assumes that physical laws govern all living organisms. Therefore, it has a broad range of applications from the molecular world to whole communities of living organisms that interact with each other (ecosystems). The study of the present thesis will focus on molecular and cellular systems, particularly in investigating the non-equilibrium behaviour of double-stranded DNA (dsDNA) and Red Blood Cells (RBC).

1.1 Molecular systems

In the 1930s, molecular biology was established as an official branch of natural science due to the technological advances that significantly increased the spatial resolution of imaging. In particular, X-ray crystallography played a central role in one of the most important discoveries of the last century: the double helix structure of the DNA.

The discovery of Watson and Crick was possible thanks to the experimental work of Rosalind Franklin and her graduate student Raymond Gosling (Fig. 1.2). They took the *Photo 51*, which was critical evidence in identifying the DNA structure. This groundbreaking result is considered a historic milestone as it yielded the first steps to studying the genetic code and protein synthesis. Both fields being the key to understand how life works.

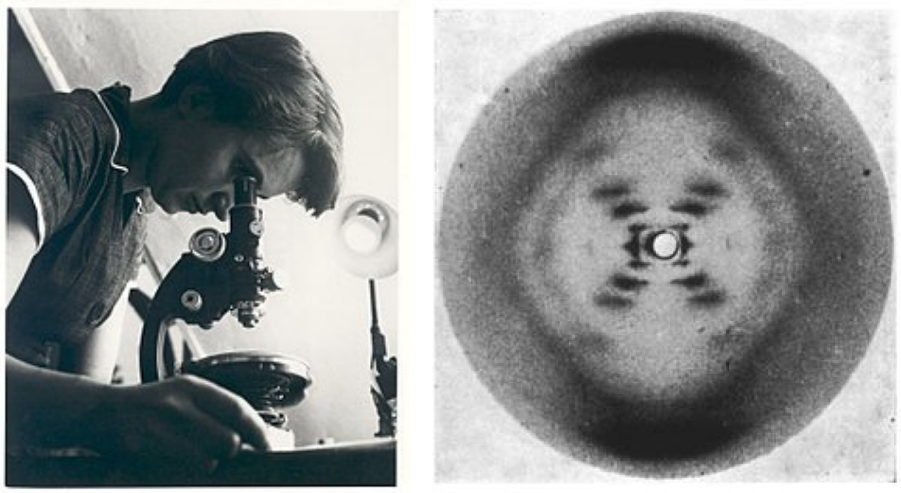

Figure 1.2: (**a**) Rosalind Franklin (**b**) Photo 51, the X-ray diffraction image of a paracrystalline gel composed of DNA fibers taken by Raymond Gosling, a graduate student working under the supervision of Rosalind Franklin in May 1952 at King's College London.

1.1.1 Nucleic Acids

The nucleic acids (DNA and RNA) are the molecules responsible for storing, transmitting, and expressing genetic information. The basic units of the nucleic acids are the nucleotides, which perform a broad amount of different functions inside the cell, such as energy transfer (ATP), intracellular signaling, oxidative-reduction functions, and many others. The nucleotides are composed by three components:

- **Nitrogenous bases** are planar, aromatic, and heterocyclic molecules derived from the purine or the pyrimidine (Fig. 1.3). Adenine,

guanine, and cytosine are found in both DNA and RNA, while thymine is only found in DNA, and uracil is only found in RNA.

- **Pentose** is a monosaccharide with five carbon atoms (5-carbon sugar), and their chemical formula is $C_5H_{10}O_5$. In the case of RNA, the pentose is the D-ribose, while for DNA is the 2′-deoxy-D-ribose.

- **Phosphate group** is a functional group or ester derived from a phosphoric acid H_3PO_4.

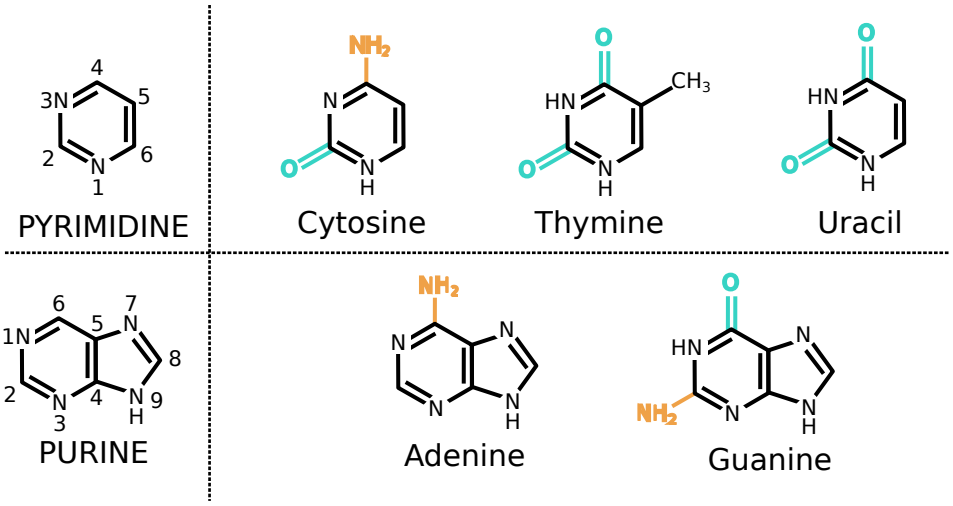

Figure 1.3: Nitrogenous Bases. More common nitrogenous bases in DNA and RNA divided in the ones derived from pyrimidine (top) and the ones derived from purine(bottom).

The nitrogenous bases bind to the pentose through an N-β-glycosidic bond that joins the C′-1 of the pentose with the N-1 of the pyrimidines and the N-9 of the purines (Fig. 1.4a). Notice that the atoms of the pentose are distinguished from the nitrogenous bases or the phosphate group by adding a ′ symbol. Usually, the phosphate group joins to the 5′ position of the pentose as shown in Figure 1.4b.

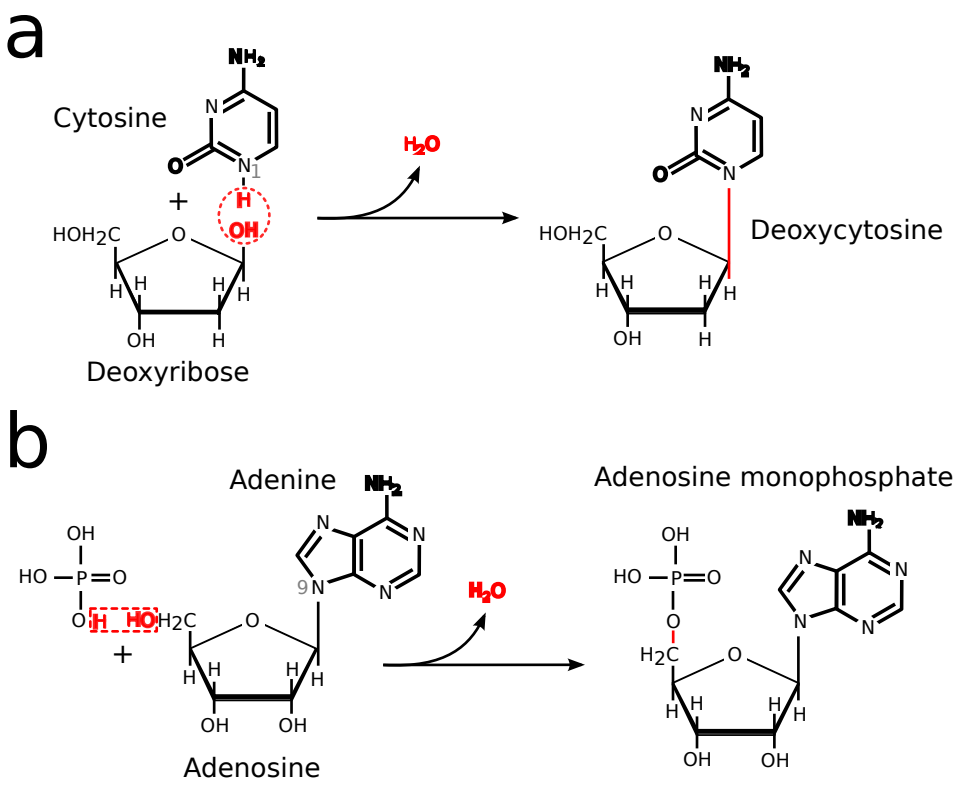

Figure 1.4: Nucleotide formation. (**a**) Formation of a Deoxycytosine by the combination of a cytosine (nitrogenous base) with a deoxyribose (pentose). (**b**) Formation of an adenosine monophosphate (nucleotide) by the combination of a Deoxycytosine (nucleoside) with a phosphate group.

The nucleotides assemble in order to form the single strands of DNA or RNA. Specifically, they join to one another through phosphodiester linkage, which bounds the -OH group at the 5′-end of one nucleotide to the -OH group at the 3′-end of the following one (Fig. 1.5a). All the phosphodiester bonds have the same orientation along the strand; for that reason, the linear chains have a directionality characterized by a 5′ and 3′ end. The terminal residue of a DNA or RNA strand in which the fifth carbon of the pentose is not bound to another nucleotide is defined as the 5′-end. While the terminal residue in which the third carbon of the pentose is not bound to another nucleotide is known as 3′-end.

In Figure 1.5b, it is shown how the two single strands coiled around an axis, forming a double helix of ∼2nm of diameter. The two strands

are antiparallel, meaning they are orientated in opposite directions ($5' \rightarrow 3'$ and $3' \rightarrow 5'$). The molecule presents two distance periodicities, the first one of 0.34nm, which corresponds to the distance between two consecutive nitrogenous bases and, the second one, around 3.4nm (10 base pairs), corresponds to one-helix turn. The bases are placed at the central region of the helix (orange), while the sugar and the phosphate group are placed at the outer part (light blue). This configuration minimizes the repulsion between the charged phosphate groups. The structure also presents two grooves designated as minor and major depending if the backbones are close together or not, respectively.

Each base is bound to another base of the opposite strand by hydrogen bonds (dash lines between bases in Fig. 1.5c). However, the linkage between two bases only occurs if they are complementary to each other. In DNA, the base pair complementarity is composed of two couples: Adenine(A) with Thymine(T) which forms two hydrogen bonds, and Guanine(G) with Cytosine(C), which bounds through three hydrogen bonds.

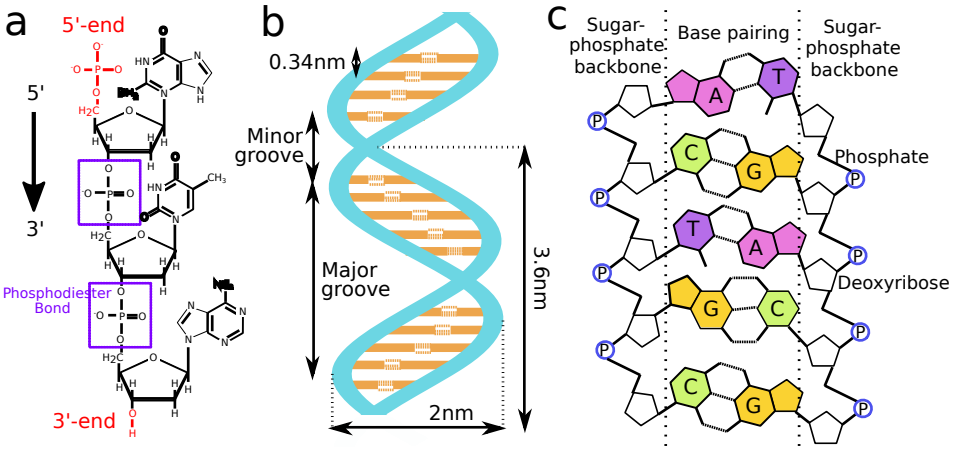

Figure 1.5: dsDNA structure. (**a**) Formation of DNA strand through the phosphodiester bond reaction between nucleotides. (**b**) Dimension and grooves of double-stranded DNA. (**c**) Schematics of the dsDNA structure differentiating the three components: phosphate group (blue circles), sugar (empty pentagrams) and nitrogenous bases (colored pentagrams and hexagons). Within each base paring region, base complementarity and the number of hydrogen bonds between nitrogenous bases are represented.

1.2 Cellular systems

Cells are the basic units of all known organisms. From the first forms of life on Earth, single prokaryotes cells, to human beings, cellular living organisms show a tremendous variability and function diversification. In particular, human beings present many different cell types, each type having characteristic features that allow it to accomplish its biological function. A critical issue is how complexity arises from a single cell, the zygote (oocyte fertilized by sperm). All the cells of our organism contain the same genetic code, the same instructions. It turns out that, in the early embryonic stages, slightly chemical heterogeneity in the zygote results in different gene expressions and, consequently, in differentiation between cells (Fig. 1.6).

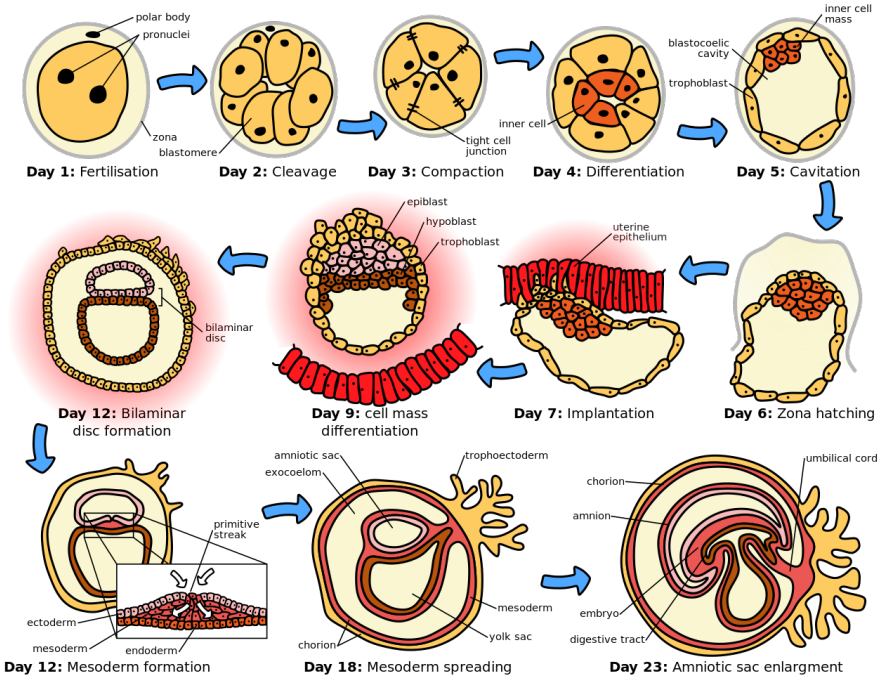

Figure 1.6: Human embryogenesis. Schematics of the embrion evolution during the first 23 days. [1]

[1] HumanEmbryogenesis.svg By Zephyris - SVG version of ., CC BY-SA 3.0,https://commons.wikimedia.org/w/index.php?curid=10811330. No changes were made.

In other words, the zygote is totipotent as its daughters' cells can become all the different cell types; however, its daughters' cells will be pluripotent (Fig. 1.7), meaning that they can become many cell types but not all of them. Hence, as cellular division repetitively takes place, the ability to become a specific type of cell reduces, resulting in cell differentiation.

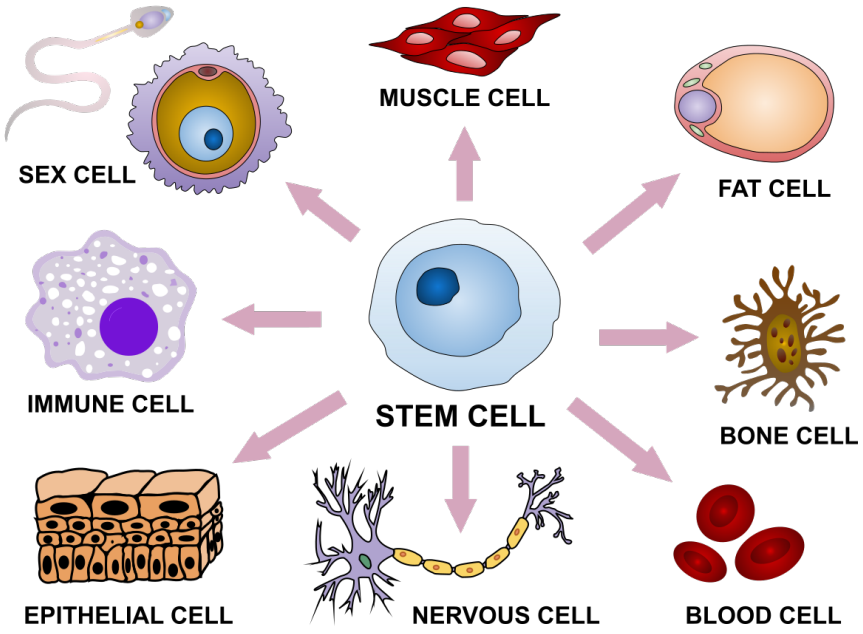

Figure 1.7: Cell differentiation. Schematics of cell differentiation where a stem cell (pluripotent) can become many different cell types. [2]

[2]Final stem cell differentiation (1).svg By Haileyfournier - Own work, CC BY-SA 4.0, https://commons.wikimedia.org/w/index.php?curid=79600426. No changes were made.

1.2.1 Red Blood Cells

As cells are not visible to the naked eye, microscopy also played a central role in their observation and understanding. Due to the larger size of cells respect to the molecules, the first observation of cells was done in the 17th century, three centuries before *Photo 51*. In particular, in 1695, Anton van Leeuwenhoek was the first person to describe and draw red blood cells (RBC) after studying them under a microscope. Although the biological importance of RBC remained unknown at this moment, nowadays, it is well known how their function is vital for most animals. RBCs are responsible for oxygen delivery to the body tissues via the circulatory system. In order to accomplish their function, RBCs present unique characteristics compared to most human cell types.

The RBCs are formed in the bone marrow by the differentiation of the hematopoietic stem cell, which can develop into all types of blood cells, including white blood cells and platelets (Fig. 1.8).

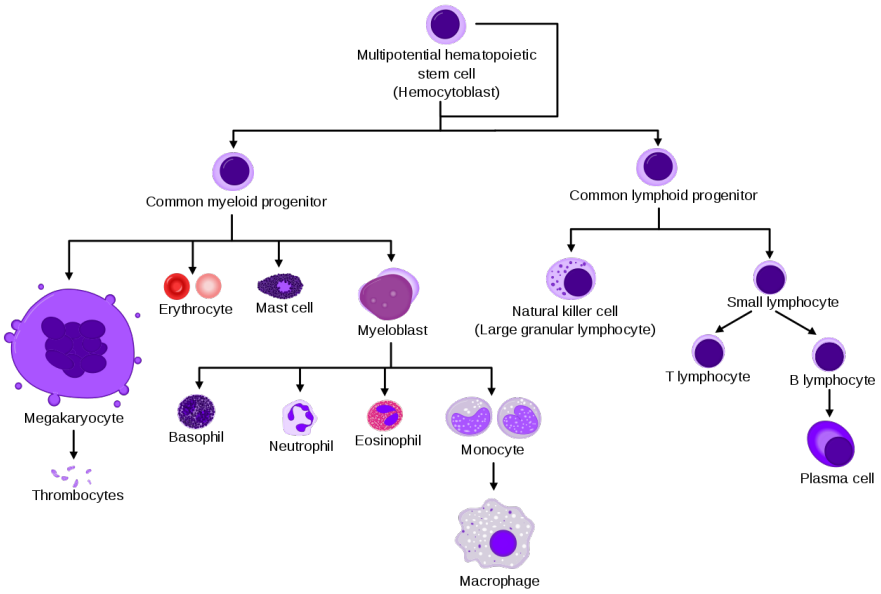

Figure 1.8: Blood cells differentiation. Schematics of blood cells differentiation starting from a multipotent hematopoietic stem cell which divides into the common myeloid, progenitor of red blood cells (erythrocytes) and platelets (thrombocytes), and the common lymphoid, progenitor of white blood cells.[3]

In humans, the mature RBC presents a biconcave shape (Fig. 1.9a) due to the lack of a nucleus that allows more room for hemoglobin (Fig. 1.9b), the iron-containing protein that binds oxygen. The loss of its nucleus also implies the incapacity to duplicate or synthesize proteins. Once a RBC is in the blood flow, its lifespan is approximately 120 days. During this period, the RBC will accumulate physical and chemical damage until it can no longer perform its function. The spleen is the main organ responsible for the RBC removal from the circulatory system, usually due to RBC rigidification.

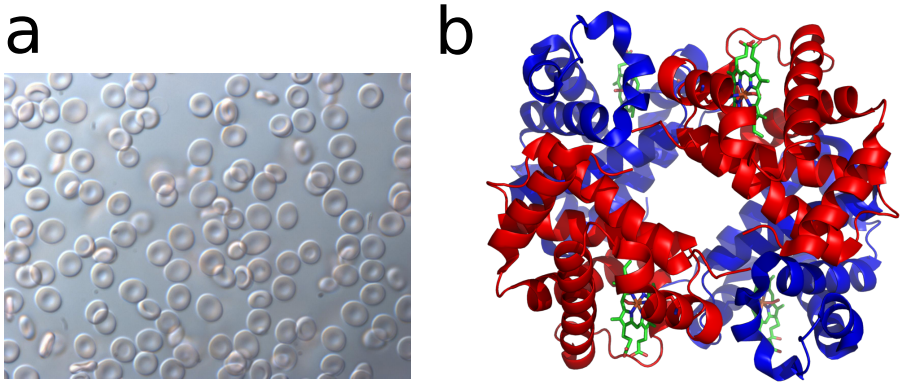

Figure 1.9: RBC microscopy and hemoglobin. (**a**) RBC microscopy image[4] . (**b**) Hemoglobin imagine created by pymol software where the four monomers are represented in red and blue and the binding sites in green[5].

A healthy RBC has a discocyte shape (Fig. 1.10a) with an approximately 8μm of diameter and 2μm of crossection. Unlike most of the other cell types, RBC does not present a tridimensional cytoskeleton;

[3]Hematopoiesis_simple.svg By A. Rad andMikael Häggström, M.D.- Author info- Reusing imagesMikael HäggströmExample citation (in caption or footnote):- & quot;By A. Rad and M. Häggström. CC-BY-SA 3.0 license.& quot; - Image:Hematopoiesis (human) diagram.png by A. Rad, CC BY-SA 3.0, https://commons.wikimedia.org/w/index.php?curid=7351905. No changes were made.

[4]By Kristina Yu, Exploratorium for NISE Network. No changes were made.

[5]1024px-1GZX_Haemoglobin.png by Zephyris at the English-language Wikipedia, CC BY-SA 3.0, https://commons.wikimedia.org/w/index.php?curid=2300973. No changes were made.

instead, its shape is sustained by a two-dimensional skeleton attached to its membrane (Fig. 1.10b,c). RBC 2D skeleton comprises alpha and beta spectrin fibers that form a network with actin protofilaments and 4.1R protein joining sites.

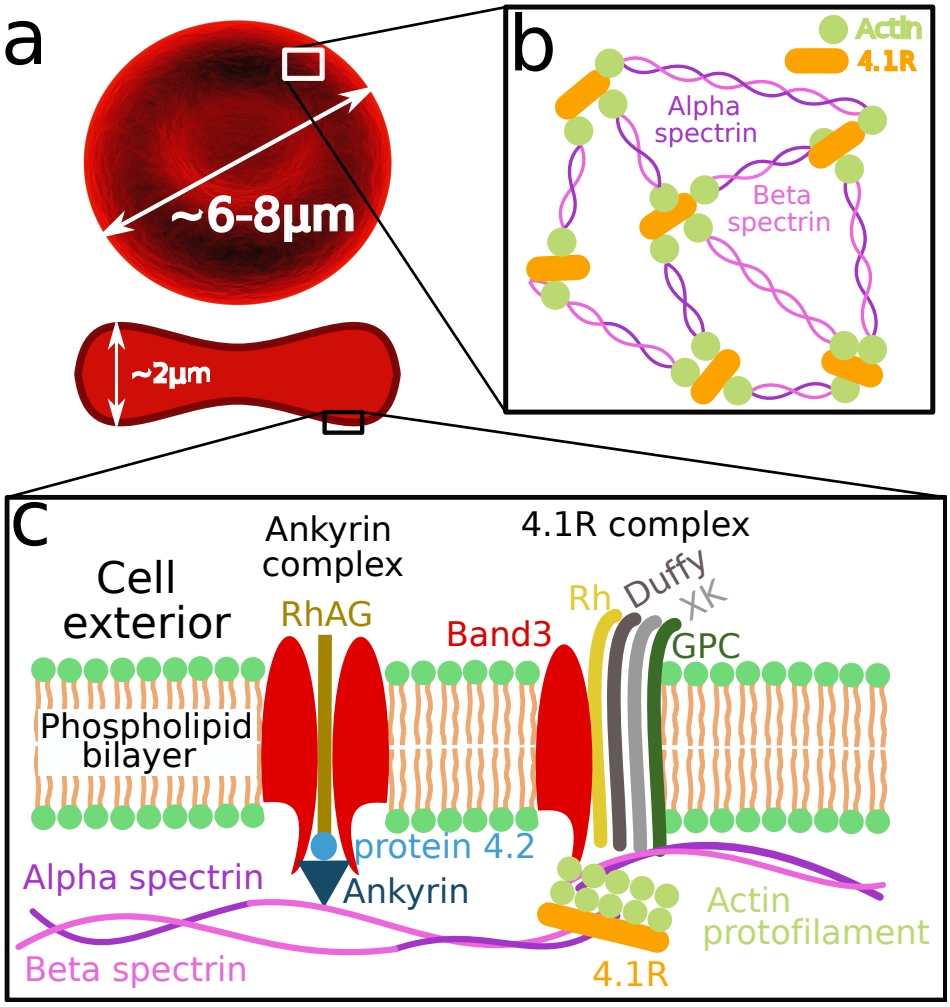

Figure 1.10: RBC dimension and structure. (**a**) RBC diameter (top) and crossection (bottom). (**b**) Schematics of the 2D RBC skeleton mainly composed of spectrin and actin which is attached to the phospholipid bilayer. (**c**) Schematics of the phospholipid bilayer of the RBC together with the 2D skeleton.

1.3 Single cell and molecule experiments

The first cellular observations were carried out by Robert Hooke in 1665 through his improved compound microscope. He observed a huge variety of cells which published in his book *Micrographia*. From that moment, the experimental techniques to observed cellular and even molecular systems have improved in terms of resolution and accuracy being the observation of DNA fiber from Rosaling Franklin one of the most groundbreaking achievements of the last century.

Although the visualization techniques were suffering a revolution, it was not possible to directly manipulate individual cells and molecules. For that reason, the most common approach was to perform bulk measurements where a high number of samples (N) were measured simultaneously. This kind of experiment, as calorimetry, gave access to precise and fundamental quantities of these systems as melting temperatures, heat capacities, etc. However, due to the average over many samples, the information related to the sample heterogeneity was systematically dismissed. It was not until the 1970's when the first techniques to exert and measure forces of microscopic objects were developed. Three of the most relevant setups are laser optical tweezers (LOT) (Fig. 1.11a) , magnetic tweezers (MT) (Fig. 1.11b), and atomic force microscopy (AFM) (Fig. 1.11c).

Nowadays, LOT, MT and AFM are the most common and widely use techniques to perform single-cell and single-molecule experiments. Each setup has a different range of forces and displacements which will suit different experimental systems.

- **Laser Optical Tweezers**: LOT setup is based on optical trapping effect. By extremely focusing laser beams LOT exert forces to tiny dielectric objects as micro-sized beads. There are a lot of different LOT instruments in terms of range of forces and laser power. Although it is more commonly used to perform single-cell experiments, its versatility allow to also work with cells.

- **Magnetic Tweezers**: The magnetic tweezers exert forces and torques to magnetic micro-particles due to an external magnetic field. It is currently used to manipulate biomolecules which are linked to the magnetic beads. To measure the force, magnetic tweezers normally employ a bead tracking system that precisely

monitor the bead position. A force calibration to transform particles position into forces is required.

- **Atomic force spectroscopy**: Atomic force microscopy is a type of scanning probe microscopy that presents the higher position resolution. Measure and exert forces by the deflection of a laser on the tip of the cantilever, which is used as a probe to scan the sample of interest.

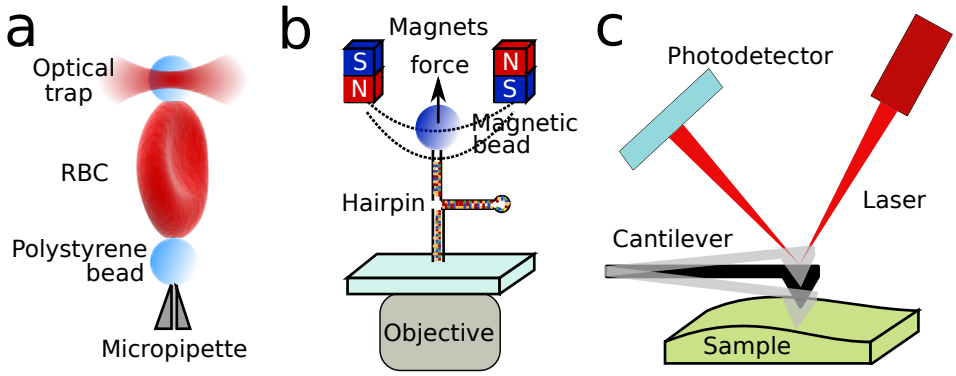

Figure 1.11: Single-molecule and cell techniques. (**a**) **Optical Tweezers**. A RBC is immobilized between two beads, the lower bead is fixed on the tip of the micropipette and the upper bead is controlled by the optical trap. (**b**) **Magnetic Twezeers**. The magnetic bead, controlled by the magnets, applies force to a hairpin fixed at the bottom surface. This configuration has a confocal image. (**c**) **Atomic force microscopy**. The laser deflects on the tip of the cantilever and the displacement, the change respect to the equilibrium positionin, is measured by the photodetector.

Chapter 2

Elastic models for polymers

As we have seen in subsection 1.1.1, nucleic acids are composed of three elements: the phosphate group, the sugar/pentose, and the nitrogenous base. In order to form a polymer, these three elements are combined and assembled through different types of bonds that result in the double-helix geometry. From a physical point of view, we want to model the global deformation of the polymer under an external force. As the scale of the polymer is much larger than the scale of its constituents, the nucleotides, it is possible to reduce its complexity to some effective degrees of freedom.

There are two models widely used in force spectroscopy studies, the freely jointed chain (FJC, Fig. 2.1a) and the worm-like chain (WLC, Fig. 2.1b).

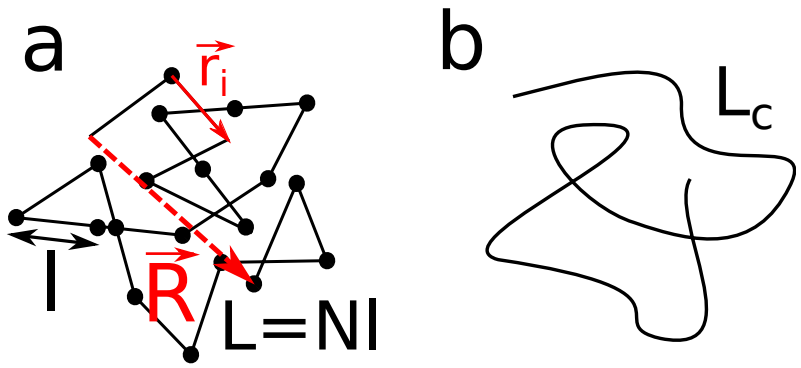

Figure 2.1: Elastic models. a) The freely jointed chain (FJC) models the polymer as a chain of N rigid monomers of length l. (**b**). In the worm-like chain (WLC) model the polymer is a semi-flexible rod.

2.1 Freely jointed chain (FJC)

The Freely jointed chain (FJC) or ideal chain is the simplest model to model polymer deformation. It considers the polymer as a single-chain of N rigid rods or monomers of length, b (b being the Kuhn length) (Fig. 2.1a). The monomers are linked together by free hinges, meaning that they can freely rotate in any direction (excluded volume interactions are not considered).

In the absence of an external force, the FJC acts as a random walk because all the possible conformations have the same energy. However, when a force is applied, there is an entropic cost as the chain gets extended. The energy of the chain in the presence of an external force, f, is expressed as,

$$E_{FJC} = -fb\sum_{i}^{N} cos\theta_i \tag{2.1}$$

where N is the number of monomers, b is the monomer length, and θ_i is the angle of each monomer respect to the applied force direction.

The average end-to-end distance $\langle x \rangle$ is obtained by summing the partition function of the system over all possible configurations.

Therefore, the final expression that relates the extension of the polymer, x_{FJC}, with the external applied force, f, is given by,

$$x_{FJC}(f) = L\left(\coth\left(\frac{fb}{k_BT}\right) - \frac{k_BT}{fb}\right) \tag{2.2}$$

where $L = Nb$ is the polymer contour length.

2.1.1 Extensible Freely jointed chain (exFJC)

In the FJC model the contour length L is a fixed parameter that does not depend on force. In general, polymers such as dsDNA studied in this thesis, show extensibility when stretched, the inextensibility assumption being only an approximation. In order to consider this energetic contribution to the FJC model, Smith et al. proposed the following correction [4],

$$x_{EFJC}(f) = L\left(\coth\left(\frac{fb}{k_BT}\right) - \frac{k_BT}{fb}\right)\left(1 + \frac{f}{S}\right) \tag{2.3}$$

where S is the stretching modulus of the polymer. The FJC and EFJC models successfully reproduce the elastic behaviour of polymers with low bending energy per monomer (see next section) such as ss-DNA, and fail to describe the dsDNA behaviour as it presents higher bending energy.

2.2 Worm like chain (WLC)

The worm-like chain (WLC) model also known as elastic rod model, considers the polymer as a continuous rod. The deformation of a rod can be characterized by three local magnitudes considering ds a segment of this rod (Fig. 2.2),

- **Stretching.** $u(s) = \Delta(ds)/ds$ is a dimensionless scalar field that defines the relative length variation of a segment upon stretching the polymer.
- **Bending.** $\vec{\beta}(s) = d\hat{t}/ds$ is a vector field with dimensions of the inverse of length that describes the variation of the unitary tangent vector of the rod, $\hat{t}(s)$.
- **Twist density.** $w(s) = d\phi/ds$ is a scalar field with dimensions of the inverse of length that defines how the consecutive elements are rotated with respect to the rod axis.

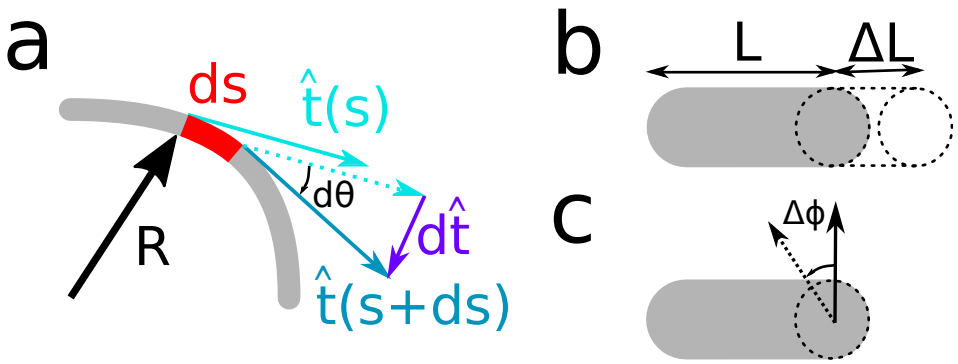

Figure 2.2: Stretching, bending and twisting. Schematic representations of (**a**) bending deformation where $\vec{\beta}(s) = d\hat{t}/ds$. (**b**). Stretching deformation characterized by $u = \Delta L/L$, and (**c**) Twisting deformation defined by $\omega = \Delta\phi/\Delta s$.

For small deformations, the elastic energy dE of an individual segment ds is a quadratic function of the fields,

$$dE = \frac{1}{2}k_BT(A\beta^2 + Bu^2 + C\omega^2 + 2Du\omega)ds \tag{2.4}$$

where Ak_BT is the bending stiffness, Bk_BT is the stretching stiffness, Ck_BT is the twisting stiffness, and Dk_BT is the twist-stretch coupling. In particular, A is the bending persistence length (generally expressed as p), and C is the twisting persistence length.

2.2.1 Inextensible Worm-like chain (in-WLC)

In order to build the simplest model, we only consider the bending contribution to the energy. Therefore, the polymer is treated as an inextensible rod as u is considered negligible. For that reason, this model is known as the inextensible worm-like-chain (in-WLC), and its energy in the presence of an external force is expressed as,

$$E = \frac{1}{2}k_BT\int_0^L dsA\beta^2 - xf \tag{2.5}$$

Calculating the partition function from Eq. 2.5 is not straight forward. In 1995, Marko and Siggia [5], solved Eq. 2.5 in the limits of low and high forces and obtained an interpolation formula,

$$f_{inWLC}(x) = \frac{k_BT}{4p}\left(1 - \frac{x}{L_c}\right)^{-2} - \frac{1}{4} + \frac{x}{L_c} \tag{2.6}$$

The in-WLC model reproduces the experimental data for ssRNA and ssDNA; however, it fails with dsDNA. In order to overcome this problem, it is necessary to introduce the stretching contribution in the model.

2.2.2 Extensible Worm-like chain (exWLC)

As in the case of the EFJC, it is necessary to introduce the stretching contribution to describe real polymers. The correction $L = L(1+f/S)$ is introduced in the interpolation formula Eq. 2.6,

$$f_{exWLC}(x) = \frac{k_B T}{p}\left[\frac{1}{4}\left(1 - \frac{x}{L} + \frac{f}{S}\right)^{-2} - \frac{1}{4} + \frac{x}{L} - \frac{f}{S}\right] \tag{2.7}$$

where S is the stretch modulus, also referred to as Y, the Young modulus and have dimensions of a force.

Equation 2.7 reproduces the experimental data for dsDNA until $\sim$ 35pN, where the force-extension curve presents a change in curvature indicating the onset of twist-stretch coupling. Above $\sim$ 35pN, the exWLC model does not reproduce the data, and such coupling has to be considered.

2.2.3 Twistable Worm-like chain (tWLC)

The twistable worm-like chain (tWLC) model considers all the contributions in Eq. 2.4. An interpolation formula for the whole range of forces can be also derived. However, for high forces, Groos et al. [6], derive an expression valid at $f > 35pN$,

$$x_{tWLC}(f) = L_c\left(1 - \frac{1}{2}\sqrt{\frac{k_B T}{fp}} + \frac{C}{SC - g(f)^2}f\right) \tag{2.8}$$

where $g(f)$ is the twist-stretch coupling,

$$g(f) = g_0 + g_1 f \tag{2.9}$$

where $g_0 = -637\text{pN}\cdot\text{nm}$, $g_1 = 17\text{nm}$, and,

$$g(f) = \begin{cases} g(30) & f < 30 \\ g_0 + g_1 f & f \geq 30 \end{cases} \tag{2.10}$$

The expression in Eq. 2.8 is compatible with the ex-WLC model (Eq. 2.7) for only $f < 30$pN as the twisting-stretch coupling contributes for $f > 30$pN (Eq. 10.12). Therefore, the tWLC model reproduces the experimental data of dsDNA until $\sim$ 60pN forces.

Part II

Noise measurements with optical tweezers

Chapter 3

Power spectra analysis

This section shows the derivation of the power spectrum of a bead diffusing inside an optical trap from its Langevin equation using the Fourier transform of the autocorrelation function. From the obtained result, we will characterize the hydrodynamics effects arising from the bead-surface and bead-bead proximity.

3.1 Power spectrum derivation

The power spectrum is defined as the Fourier transform of the autocorrelation function R_{xx} of a signal,

$$S_{xx}(\nu) = F_t[R_{xx}(t)] \tag{3.1}$$

The Langevin equation for a particle moving inside a one-dimensional harmonic potential and subjected to an external force $f(t)$ is expressed as,

$$m\frac{d^2x}{dt^2} + \gamma\frac{dx}{dt} + kx = f(t) \tag{3.2}$$

where m is the particle's mass, γ is the friction coefficient, and k is the stiffness associated with the optical trap's harmonic potential. In the overdamped limit ($m = 0$) when $f(t) = 0$, Eq. (3.2) simplifies,

$$\gamma\frac{dx}{dt} + kx = 0 \tag{3.3}$$

Solving the differential Eq.(3.3) the following expression for the position of the bead is obtained,

$$x(t) = x(0)e^{-kt/\gamma} \tag{3.4}$$

The autocorrelation function is defined as,

$$R_{xx}(\Delta t) = \frac{1}{T}\int_0^T x(t)x(t+\Delta t)dt =< x(t)x(t+\Delta t) > \tag{3.5}$$

Introducing Eq.(3.4) in Eq.(3.5),

$$R_{xx}(\Delta t) =< x(0)e^{-kt/\gamma}x(0)e^{-k(t+\Delta t)/\gamma} > \tag{3.6}$$

$$R_{xx}(\Delta t) =< x^2(0) > e^{-k\Delta t/\gamma} \tag{3.7}$$

For the equipartition theorem is known that $< x^2(0) >= k_BT/k$, so,

$$R_{xx}(\Delta t) = \frac{k_BT}{k}e^{-k\Delta t/\gamma} \tag{3.8}$$

then Fourier transform is performed in Eq.(3.8),

$$\hat{R}_{xx}(\omega) = \int_{-\infty}^{\infty}\frac{k_BT}{k}e^{-k\Delta t/\gamma}e^{-i\omega t}dt \tag{3.9}$$

$$\hat{R}_{xx}(\omega) = \frac{2k_BT\gamma}{\gamma^2\omega^2 + k^2} \tag{3.10}$$

In terms of the angular corner frequency $\omega_c = k/\gamma$, we get,

$$\hat{R}_{xx}(\omega) = \frac{2k_BT\gamma}{\gamma^2(\omega^2 + k^2/\gamma^2)} = \frac{2k_BT}{\gamma(\omega^2 + \omega_c^2)} \tag{3.11}$$

Finally, from the relation $\omega = 2\pi\nu$ the power spectrum in terms of frequency ν is expressed as,

$$S_{xx}(\nu) = \frac{k_BT}{2\pi^2\gamma}\frac{1}{(\nu^2 + \nu_c^2)} \tag{3.12}$$

Notice that, in the case of a bead optically trapped, the force power spectrum is related with the position one as,

$$S_{ff}(\nu) = k_b^2 S_{xx}(\nu) \tag{3.13}$$

where k_b is the stiffness of the bead. As the power spectrum's integral is the signal's variance, and the optical trap creates a harmonic potential with a linear force-displacement relation $f = k_b \Delta x$, their variance relation will be $\sigma_f^2 = k_b^2 \sigma_x^2$. Therefore, as $\sigma_f^2 = k_B T k_b$, the variance of the position will be $\sigma_x^2 = k_B T / k_b$.

3.2 Measuring the friction coefficient

In hydrodynamics fluid, the friction coefficient of a spherical object in an incompressible fluid, has the following expression,

$$\gamma = 6\pi\eta r \tag{3.14}$$

where η is the fluid viscosity, and r is the radius of the bead.

In order to measure the friction coefficient from passive measurements, it is necessary to record a zero force signal at a high sampling frequency. The ideal sampling frequency depend on the particular system. It is necessary to record at a sampling frequency at least five times bigger than the characteristic corner frequency. In our case we normally record at 40kHz. The force power spectrum is expressed as,

$$S_{ff}(\nu) = \frac{k_B T k_b^2}{\gamma 2\pi^2} \frac{1}{(\nu^2 + (k_b/\gamma)^2)} \tag{3.15}$$

with k_b and γ as free parameters. Then, the friction coefficient can be obtained by fitting Eq.(3.15) to the power spectrum of the experimental signal at zero force.

Unlike the Stokes test, this method does not move the fluid around the bead, avoiding possible noise sources as bubbles or fluid heterogeneities. For that reason, the power spectrum method will be used in order to experimentally obtain the dependence between the friction coefficient, γ, on the bead-surface and bead-bead distance, y.

3.3 Bead-surface proximity

As introduced in the previous section, for a single bead optically trapped, the power spectrum follows a Lorentzian shape. In Figure 3.1 a,b the raw power spectrum is represented in grey, a boxcar average filter is represented in black circles, and the fit to Eq. 3.15 in red. From fitting Eq. 3.15 to experimental data, we obtain the friction coefficient γ together with the trap stiffness k_b. In order to study the hydrodynamic effects due to the proximity of a planar surface (Fig. 3.2a), we will measure force signals at different distances respect to the coverslip. Figures 3.1a,b correspond to power spectra 90μm and 1μm away from the coverslip respectively. In Figure 3.1c their comparison is shown. Although the boxcar for $z = 90\mu$m and $z = 1\mu$m are almost equal, the fitting parameter γ increases a 40% its value.

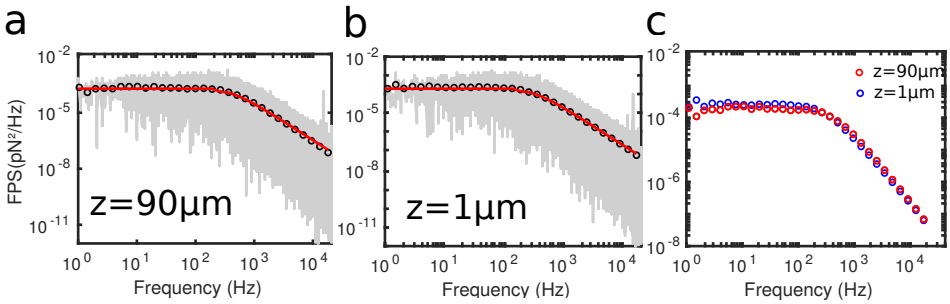

Figure 3.1: Power spectra and box car average filter. (**a**) Power spectra in logarithmic scale of a single bead 90μm away from the coverlip (grey), with its corresponding box car average (black circles) and the fit to Eq. 3.15 (red). (**b**) Power spectra in logarithmic scale of a single bead 1μm away from the coverlip (grey), with its corresponding box car average (black circles) and the fit to Eq. 3.15 (red) (**c**) Box car average comparison of the power spectra taken at 90μm and 1μm respect to the coverslip.

As reported in the literature [7, 8], at first order, the friction coefficient of a sphere near a planar surface follows the relation,

$$\gamma(z) = \gamma_0 + \frac{A}{z} \tag{3.16}$$

where γ_0 is the friction coefficient when there is no hydrodynamic effect of the surface, A is a geometric factor, and z is the distance to the surface.

In Figure 3.2b, γ values for three different 3μm diameter beads at different distances z respect to the coverslip are represented in circles of different colors together with the fit to Eq. 3.16 (black).

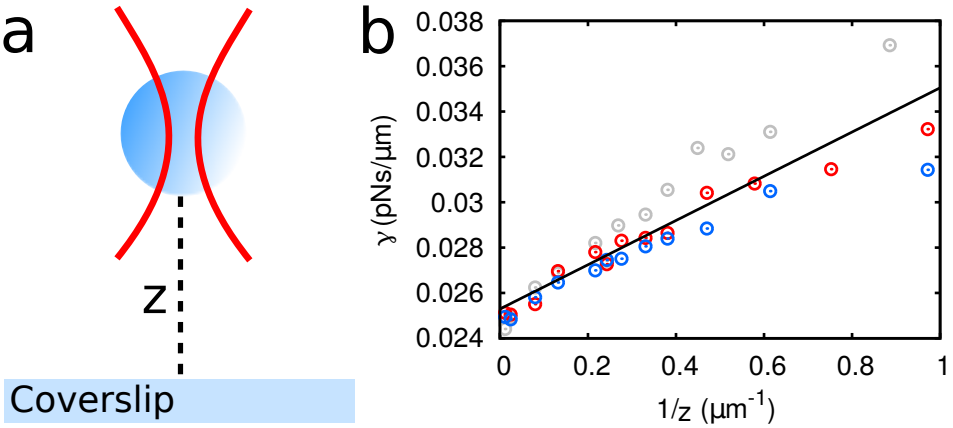

Figure 3.2: Bead-surface effects on hydrodynamics and friction. (**a**) Scheme of $3\mu m$ bead optically trapped close to the planar surface of the coverlip. (**b**) Friction coefficient plotted versus the inverse of the bead-coverslip distance for three different $3\mu m$ beads, each one represented with a different color. A fit over the three data sets is shown (black line).

The obtained results of the dependence between the friction coefficient and the bead distance to the surface are,

$$\gamma_0 = 0.0253(3)\text{pNs}/\mu\text{m} \qquad \text{A} = 0.0098(7)\text{pNs}$$

The friction coefficient for a 3μm diameter bead in mQ water at 25°C can be computed using Eq. 3.17,

$$\gamma = 6\pi \cdot 8.94 \cdot 10^{-4}\text{Pa} \cdot \text{s} \cdot 1.5\mu\text{m} = 0.0253(4)\text{pNs}/\mu\text{m} \qquad (3.17)$$

As expected, the friction coefficient for large z, γ_0, is compatible with the theoretical prediction of the single bead friction coefficient.

3.4 Bead-bead proximity

The hydrodynamic effect of a bead near a parallel plane, as shown in the previous section, has already been reported [9] as $\gamma \sim 1/y$. Some-

thing similar is observed when, instead of a plane, there is another bead.

The experiment consists in immobilizing a bead of $2\mu m$ of diameter (the typical size of an streptavidin bead - see Appendix B-) on the tip of the pipette and measure the zero-force signal of a 3μm diameter bead, optically trapped, at difference distances y as is shown in Fig.(3.3A), where the vertical alignment is perfect. However, a misalignment of a few tenths of nm is possible as depicted in (Fig.(3.3B)). Therefore, the following expression will be considered to fit the experimental data,

$$\gamma(y) = \gamma_0 + \frac{A}{\sqrt{y^2 + x_0^2}} \tag{3.18}$$

where γ_0 is the friction coefficient for large y (when the presence of the $2\mu m$ bead has no effect), A is a geometric coefficient, and x_0 is the misalignment in the x-direction.

In Figure (3.3C), results are show for three values of x_0. A fit is performed by imposing that γ_0 and A have to be the same in the three cases and that x_0 can have a different value in each bead.

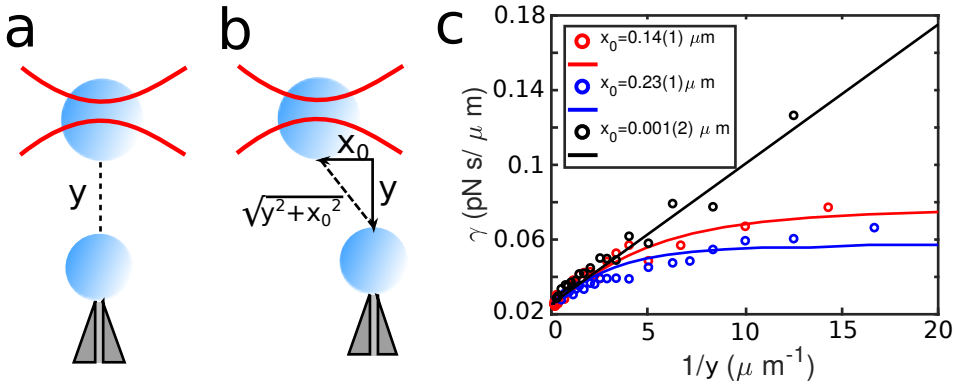

Figure 3.3: Bead-bead effects on hydrodynamics and friction. (**a**) A $2\mu m$ bead is fixed on the tip of a pipette and a $3\mu m$ bead optically trapped aligned in the y-axis. (**b**) Scheme of $2\mu m$ bead fixed on the tip of a pipette and a $3\mu m$ bead optically trapped with missalignment characterized by the parameter x_0. (**c**) Friction coefficient plotted versus the inverse of the bead-bead distance y for three $3\mu m$ beads at different x_0, each one represented with a different color, with their corresponding fits.

Assuming these conditions, a the fitting parameters γ_0 and A are obtained for the 2μm - 3μm beads geometry,

$$\gamma_0 = 0.025(7)\text{pN} \cdot \text{s}/\mu\text{m} \qquad \text{A} = 0.0075(3)\text{pN} \cdot \text{s}$$

The friction coefficient value for large distances y, γ_0, is again compatible with the theoretical prediction of a 3μm diameter single bead friction coefficient $\gamma = 0.0253(4)\text{pN} \cdot \text{s}/\mu\text{m}$.

Notice that the geometric factor A is larger in the bead-surface case than in the bead-bead case. The comparison of A parameter is not straight forward as the bead-surface distance is z and the bead-bead distance is y. However, it seems reasonable to obtain a bigger effect on the friction coefficient of a $3\mu m$ diameter bead with an infinite plane rather than with a $2\mu m$ diameter bead.

These results will be crucial for the study of dsDNA elasticity in Chapter 10 as the bead-bead proximity will vary γ value for the shorter molecules (1kbp and 3.6kbp).

Chapter 4

Optical Tweezers

4.1 Trapping with radiation pressure

Optical trapping was invented by Arthur Ashkin in 1970 and is based on the manipulation of microscopic objects using light pressure. The first observation of acceleration of freely suspended particles by the forces of radiation pressure from continuous-wave (CW) visible laser light was reported in 1970 [10]. Until that time, radiative forces were the main source of noise to detect radiation pressure. By suspending rather transparent particles in relatively transparent media, Ashkin was able to overcome the problematic effect of radiative forces, which were caused by temperature gradients in the surrounding medium. The crucial experiment consisted of suspending latex spheres of different diameters in water and observing how they were drawn toward the beam axis and accelerated in the propagation direction of light. The forces responsible of this effect are represented in Figure 4.1.

The relation between the refraction index of the medium, n_m, and the particle, n_p, is critical. When the refraction index of the sphere is larger than the medium one, the sphere will be pushed into the beam towards the maximum intensity region (beam axis) as it will act as a focusing lens. If the relation is inverted, the sphere becomes a diverging lens, being pushed out of the beam.

This observation established the bases of optical trapping: two identical counter-propagating Gaussian beams (moving in opposite directions) should cancel the forces that accelerate the particle, trapping it at the midway point. In other words, the radiation pressure alone

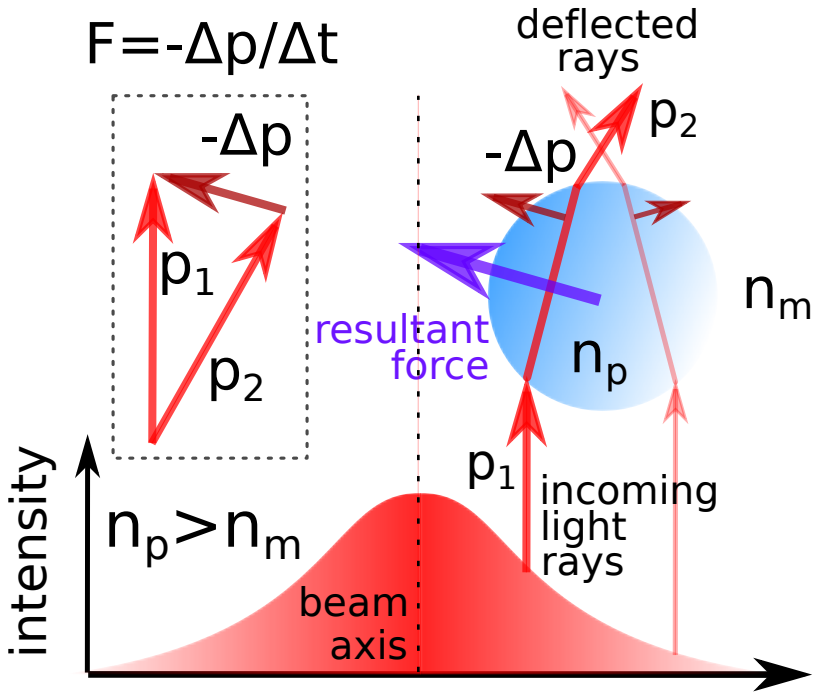

Figure 4.1: Radiation pressure. In the presence of a laser TEM_{00} mode (red Gaussian), the bead, due to the net change in linear momentum (Δp) of the deflected rays, feels a resultant force in the beam axis (vertical dashed line) direction. The index of refraction of the particle (n_p) not ... of the medium (n_m).

creates a optical well able to trap a microscopic particle.

4.2 Applications of optical trapping

The consolidation of this idea opened a new field of manipulating small biological objects using laser beams. A revolution in biophysics just began. Ashkin himself was able to capture viruses, yeasts, bacteria, and protozoa [11] [12]. One of the most critical aspects of working with living systems is the biological damage that a laser beam can cause. For that reason, the proper choice of power and wavelength of the laser beam is crucial. The near-infrared region is a window of transparency for biological materials preventing damage by light absorption. In particular, wavelengths around 1μm are most common

in optical trapping [13]. Although optical traps present laser-induced heating effects, they are minor [14].

Optical forces are usually in the range of piconewtons ($1pN = 10^{-12}N$). Although this magnitude is too small for the macroscopic world we are used to, pN forces govern the cellular and molecular worlds. Deformability of Red Blood Cells (RBC), unfolding and folding of DNA and RNA hairpins and proteins, stretching, bending, twisting, and overwinding of DNA occur at this force scale.

In the case of cell manipulation, e.g. in viruses and bacteria, the optical trap is able to directly capture the object of interest. On the contrary, when the scale is reduced to the molecular world, the trap can no longer capture the system due to its size. In order to overcome this issue, the "handle technique" method was implemented. It consists of attaching a dielectric sphere to the molecule being able to directly manipulate it using optical tweezers [15].

4.3 Measure forces and positions

Using radiation pressure to manipulate or capture microscopic objects, whether inanimate or living systems, is not the same as controlling the force exerted on them. Once the trapping phenomenon was established, there was the need to crystallize this proof of concept to a more advanced device. For that reason, in 1985 [16], Arthur Ashkin and his collaborators invented the Optical Tweezers setup. This device, which counts on a three-dimensional stable optical trap, can capture and measure the forces exerted by or to very different systems.

In order to measure force using an optical trap, a harmonic potential is assumed. Somehow, the optical trap is treated as a virtual spring with a characteristic stiffness k. This way, by knowing the displacement Δx, the force $F = k\Delta x$ can be computed.

4.3.1 Force probe

Assuming a linear relationship between the displacement and the force is not straightforward from an experimental point of view. The optical trap does not have a characteristic stiffness, although it is typical to find this expression in the literature. Therefore, as has been mentioned before, there are two possible methods to measure forces with optical

tweezers. The first method consists in trapping the object directly when it is large enough (RBC, viruses, bacteria, etc.). The second method is the "handle technique," or the force probe. Using a spherical object as a force probe allows us to have a well-characterized stiffness from the trap. Below in Figure 4.5 we show how to obtain the friction coefficient and the bead stiffness from a Lorentzian fit to the power spectrum (Eq. 3.15), uper changing bead size and trap stiffness.

Hence, we will be able to measure forces from systems attached to the bead, as RBC, dsDNA molecules, RNA hairpins, or even proteins, by measuring the displacement of the center of the bead respect to the center of the optical trap, Δx, being $F = k_b \Delta x$, the resultant force.

4.4 Mini-Optical Tweezers instrument

The miniTweezers [17] (Fig. 4.2a) consists of two focused counter-propagating laser beams ($P = 200\,mW$, $\lambda = 845\,nm$) that create a single optical trap [18]. It employs high-NA objectives ($NA = 1.2$) but underfills them to be able to collect almost all scattered light to measure the change of light momentum using position-sensitive detectors (PSDs). Before the objectives, a pellicle diverts ∼8% of each laser beam to a secondary PSD to determine the optical trap position. The remaining ∼ 92% is collimated using a lens, and it is introduced into the optical axis by using a polarizing beam-splitter that selects the horizontally polarized light. Then the linearly polarized light of each laser is circularly polarized by a quarter waveplate. The use of quarter-wave plates ensures that the light coming from the two laser beams do not interact with each other and guarantees that the light reflected from the particle is not returned to the laser but upon reflection is redirected to the opposite PSD [19]. The laser beams are focused by the objectives on the same spot and form the optical trap, which can hold dielectric objects with a refraction index higher than the surrounding aqueous medium (e.g., polystyrene beads) and exert forces to them. The exiting light is collected by the opposite objective and is converted to vertically polarized light by the other quarter-wave plate. The vertically polarized light is extracted from the optical path using two polarizing beam-splitters and relay lenses that redirect the light to the PSDs that measure the intensity of the beam (i.e., its

exerted force). The mini tweezers has a resolution of 0.1pN and 1nm at a 1kHz acquisition rate.

The chamber where the experiments are performed is placed between the two objectives and held with a metallic mount with three stages permitting movement in the x-, y- and z-directions. There are two possible ways to manipulate the position of the optical trap with respect to the chamber depending on the precision that is needed. For large displacements (up to hundreds of micrometers), the whole chamber is displaced along the x-, y- and z-directions using stepmotors. For fine displacements (less than a few micrometers), the optical trap is displaced along the x- and y-directions with a 2D piezoelectric motor attached to the tip of the light emitting optical fiber (wiggler).

The schematics of the experimental setup is presented in Fig. 4.2a. The experiments are performed in a microfluidics chamber placed vertically in the setup. As schematically shown in Figs. 4.2b and 4.2c, this microfluidics chamber has three channels: we will refer to the three channels as the upper, central and lower channel. The propagation of both laser beams is perpendicular to the chamber surface (z-axis). The experimental area is restricted to the central channel, where the object of study (biomolecule or cell) is held by two beads, one held by the optical trap and the other held by a glass micropipette, as shown in Fig. 4.2d.

The upper and lower channels are used to supply the two types of coated beads used in the experiments. For single-molecule pulling experiments, two beads of different sizes are used to distinguish them by eye. The bead of $\sim 2\mu$m of diameter, is coated with streptavidin (SA bead) and is placed on the tip of the micropipette immobilized by air suction(Fig. 4.2d). The other one, of $\sim 3\mu$m of diameter, is coated with digoxigenin (AD bead) and incubated with the molecular construct (bead preparation for single molecule experiments is detailed in Appendix B). The AD bead is the one captured in the optical trap. For the RBC experiments, the coating beads details are explained in Appendix D.4.

The microfluidics chamber is realized by sandwiching two layers of parafilm (Parafilm M, Bemis) between two coverslips (No. 2, dimensions $24\,mm \times 60\,mm \times 200\,\mu m$), as shown in Fig. 4.2c (preparation steps are detailed in Appendix A).

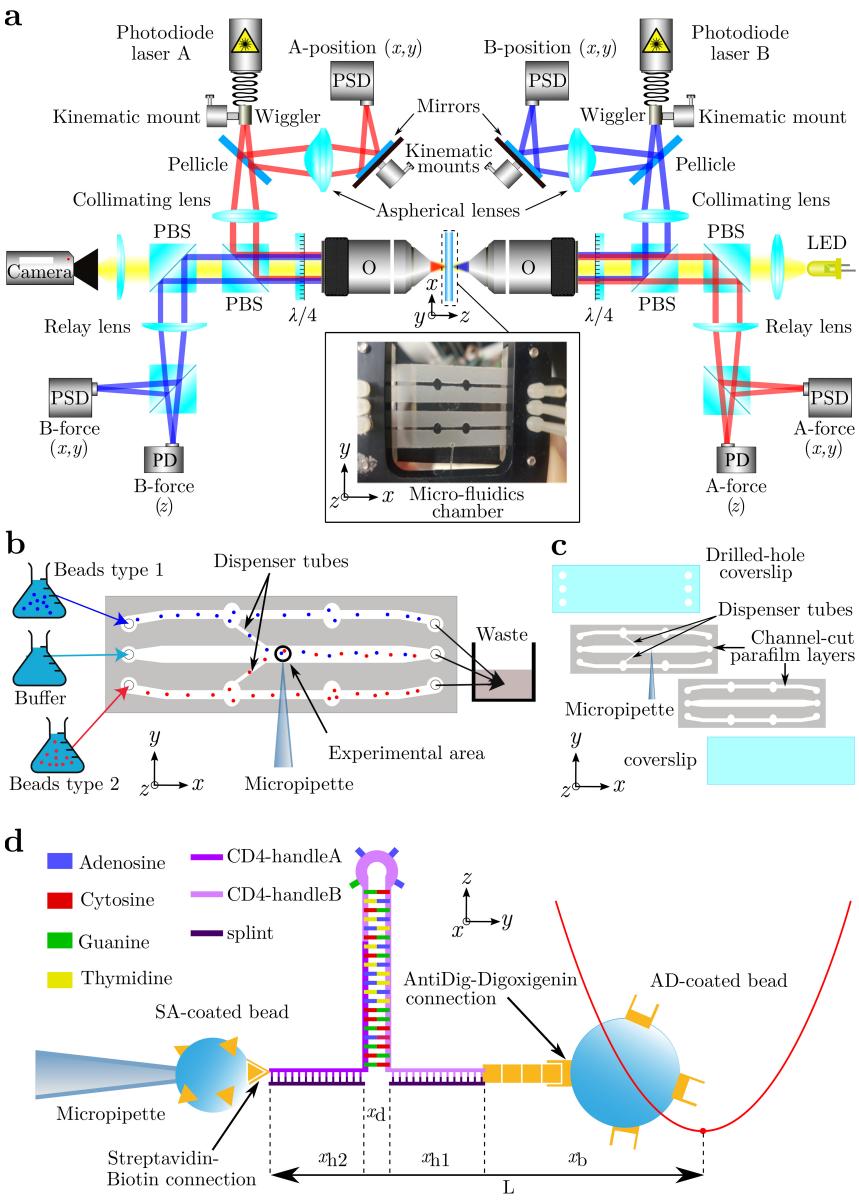

Figure 4.2: Mini-Tweezers setup. Schematic representations (**a**) of the miniTweezers setup, (**b**) of the microfluidics chamber (the flow goes from left to right, and the laser beams propagate perpendicularly to the surface of the chamber), (**c**) of the assembly procedure for the construction of the chamber, and (**d**) of the molecular configuration for the DNA hairpin pulling experiments (where the DNA hairpin is held between a bead immobilized on the tip of a micropipette and a bead captured in the optical trap, depicted as a harmonic well). Note that x_{h2}, x_d, x_{h1}, and x_b are distances along the y-axis.

4.4.1 Calibration

There are several approaches in order to measure force and displacement in an optical tweezers device. Although all LOT devices share the use of laser beams to trap tiny objects, not all of them have photodetectors monitoring the change in beam position or light momentum. Many of them usually use video analysis to transform the change of bead position into force, assuming a specific trap/bead stiffness. Our mini-tweezers setup measures the beam position before the formation of the trap and the change in light momentum after the light refracts in the force probe. For that reason, for a specific probe, a force and position calibration is needed.

4.4.1.1 Force calibration

Photodetectors return an electric signal (measured in volts) that needs to be converted to force (measured in pN) through a calibration factor. In order to measure this factor, we perform a Stokes test. It consists of moving the fluid around the bead at a constant velocity and measuring the PSD detectors' resultant signal. Moving the fluid can be achieved by controlling the motor's velocity of the mini-tweezers. The stack-slip condition ensures that the fluid is dragged at the speed of the moving chamber. Then, the force on the bead follows Stokes' law,

$$F = \gamma v \tag{4.1}$$

where F is the force, γ is the friction coefficient, and v is the velocity. From the fluid velocity and the friction coefficient of the bead (Eq. 3.17) (we use calibration beads of diameter of $3.00 \pm 0.02\mu$m), we extract the calibration factor by comparing the measured force by the photodetector (PSD) and Eq. 4.1.

As we can observe in Figure 4.3, once the force is calibrated, a linear relationship between force and motor's velocity is obtained with a slope equal to the bead's friction coefficient.

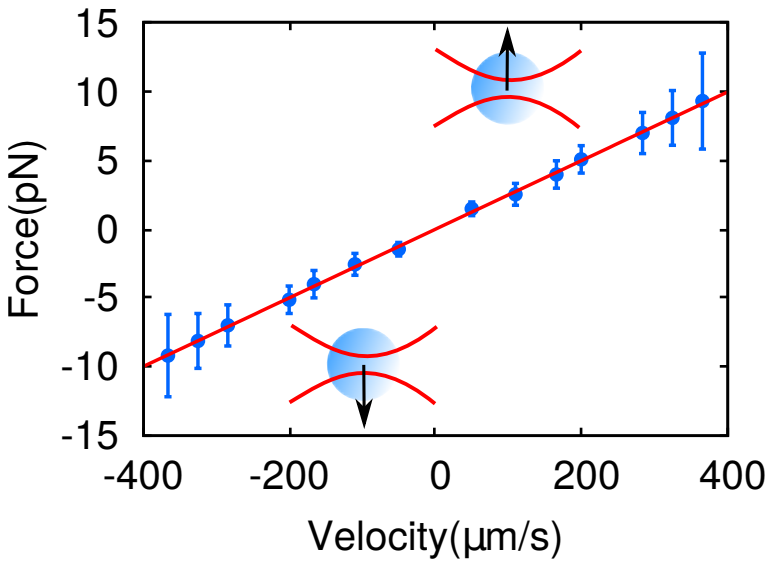

Figure 4.3: Stokes' test. Force versus motor's velocity for a calibration bead of 3μm of diameter. In red, the linear fit with a slope equal to the bead's friction coefficient $\gamma = 2.5(2)$pNs/nm.

4.4.1.2 Position calibration

As in the previous section, to calibrate the position, we need a calibration factor that relates the electrical signal from the photodetectors to the trap position, which is measured in nm. The first step is to immobilized a calibration bead on the tip of the micropipette (Fig. 4.4 inset). Then, we activate the autoalign protocol (which imposes that both traps exert the same force) and start moving the motor's position (which controls the microfluidic chamber). As observed in Figure 4.4, the LightLever signal and the motor's position follow a linear behavior, being the slope the calibration factor.

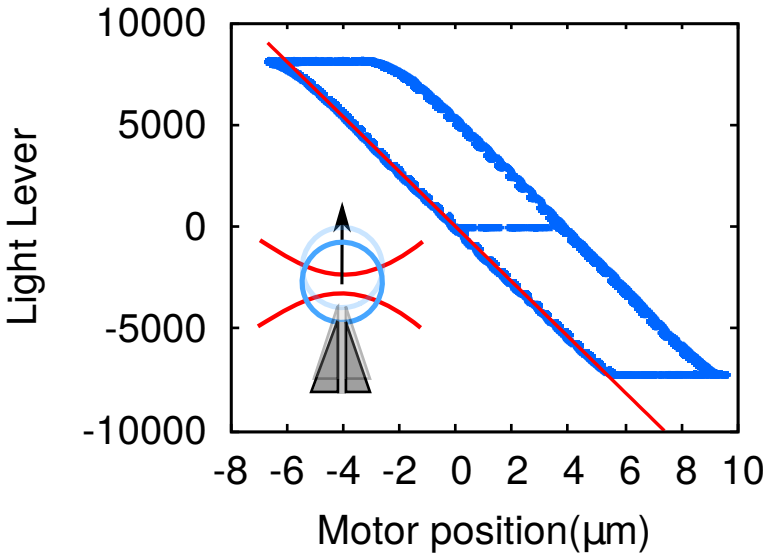

Figure 4.4: Laser trap position calibration. Position photodetector signal versus motor's position. In red, the linear fit to obtain the position calibration factor.

4.4.1.3 Trap stiffness characterization

After force and position calibration, we determine the trap stiffness using one of these two methods:

- **Power spectrum**. This method is used to determine the trap stiffness at zero force only from thermal fluctuations. As derived in section 3.1 Eq. 3.12, the force power spectrum of a single bead fluctuating inside an optical trap, in terms of trap stiffness k_b and friction coefficient γ, is expressed as,

$$S_{ff}(\nu) = \frac{k_B T k_b^2}{\gamma 2\pi^2} \frac{1}{(\nu^2 + (k_b/\gamma)^2)} \tag{4.2}$$

  As shown in Figure 4.5, a Lorentzian function $g(\nu) = A/(\nu^2 + \nu_c^2)$, where A is the amplitude and ν_c is the corner frequency of the force power spectrum. Identifying the amplitude as,

$$A = \frac{k_B T k_b^2}{\gamma 2\pi^2} \tag{4.3}$$

and the corner frequency as,

$$\nu_c = \frac{k_b}{2\pi\gamma} \tag{4.4}$$

we can express both k_b and γ in terms of amplitude, A, and corner frequency, ν_c, as,

$$k_b = \frac{A\pi}{k_B T \nu_c} \tag{4.5}$$

and,

$$\gamma = \frac{A}{2k_B T \nu_c^2} \tag{4.6}$$

From the fitting values A and ν_c, we derive k_b and γ for two different beads of 3μm and 6μm of diameter. These results are collected in Table 4.1.

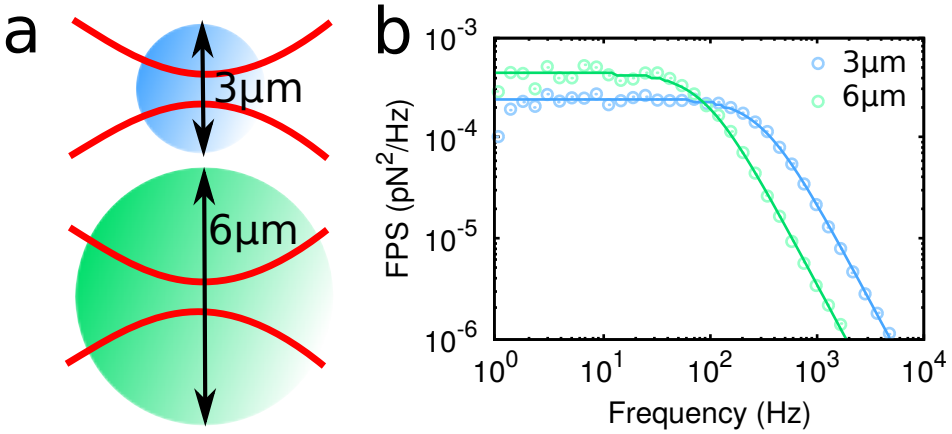

Figure 4.5: Power spectra of $3\mu m$ and $6\mu m$ diameter beads (**a**) Schematics of the two different beads with the optical trap (red). (**b**) Power spectrum in log-log scale for the two diameter beads and their corresponding fits to a Lorentzian.

Figure 4.6a shows the boxcar average of the power spectrum of a 3μm diameter bead at seven different laser powers. As the laser

	$\gamma(pN \cdot s/nm)$	k_b(pN/nm)
3μm	$2.6(2)10^{-5}$	0.060(3)
6μm	$5.7(5)10^{-5}$	0.030(2)

Table 4.1: Friction coefficient and trap stiffness. Results from the Lorentzian fit in Figure 4.5.

power increases, the bead stiffness also increases; however, the friction coefficient will not be affected as the bead diameter will remain the same.

- **Trap stiffness for high forces**. Power Spectrum analysis measures the k_b at zero force. Therefore, we need a different method to measure the trap stiffness in the presence of a force. In order to do so, a calibration bead is immobilized on the tip of the micropipette (Fig. 4.6b inset) by air suction. Starting at zero force, we move the optical trap upwards until reaching the maximum force ($\sim$ 100pN). Computing the derivative of the force-trap displacement curve (FDC), we obtain the bead stiffness, which follows a quartic potential respect to force as shown in Figure 4.6

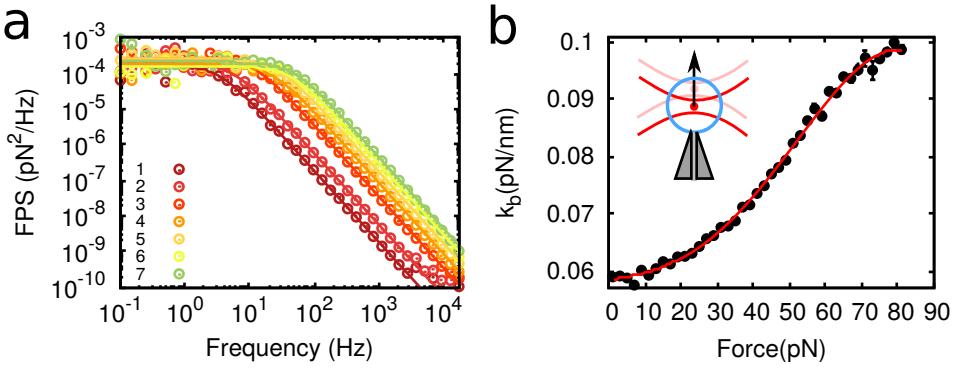

Figure 4.6: Force and position calibration (**a**) Power spectrum versus frequency in logarithmic scale for a 3μm diameter bead at different laser power. 1 indicates the minimum laser power and 7 the maximum one. (**b**) 3μm diameter bead stiffness versus force with its corresponding fit to a quartic potential (red).

Part III

Dynamics and non-equilibrium effects in red blood cells

Chapter 5

Introduction

Red blood cells (RBC) are the most abundant and simplest cells in human body. They are transported through the bloodstream and are responsible of oxygen delivery to the body tissues. While they circulate through capillaries, RBC are subject to mechanical deformation and stress. Capillaries can be thin as half the RBC disk diameter (6-8μm), causing RBC to squeeze as they pass through. Mechanical properties of RBC are tightly related to shape and composition being crucial for oxygen transport and delivery. Mechanical properties are highly dependent on endogenous (e.g. genetic) and exogenous (e.g. physicochemical stresses, aging) factors and are determinant for homeostasis. If altered they lead to diseases and disorders (such as haemolytic anemias and thrombosis). Therefore, the characterization of RBC mechanical properties is an important biomarker for human health.

In humans, the mature RBC lacks a nucleus making more room to store the oxygen-binding protein, haemoglobin, increasing the capacity of transporting oxygen. Moreover, the typical biconcave shape of RBC increases their surface area facilitating oxygen diffusion [20]. The lifespan of human RBCs is approximately of 115 days [21]. During this period they repeatedly circulate in the bloodstream lasting for about a minute per circulatory cycle [22]. Therefore, RBC in vivo are subjected to stress and strain, never reaching mechanical equilibrium.

Mechanical deformability dysfunction is directly related with several diseases such as sickle anaemia [23], malaria [24], thalassemia [25] etc. Moreover, during their lifespan, RBCs suffer from numerous

age-dependent alterations that conform the RBC aging phenotype (e.g. decline of metabolic activity, cell shape modification, membrane remodeling, oxidative injury, microvascularization, exposure of surface removal markers among others [26]). All these modifications in metabolic and physical properties of RBC trigger erythrophagocytosis that consists in the ingestion of RBC by macrophages normally located in the splenic and hepatic sinusoids [27]. It has been reported that most RBC dysfunctions systematically lead to a rigidification of the cell [23–25, 28]. RBC are viscoelastic, showing complex time-dependent responses to applied mechanical stress. Therefore, dynamical biomarkers such as frequency dependent elastic modeli yield valuable information about their physiological state. Indeed, the viscoelastic response of living cells (e.g. adherent type) and RBC have been studied in the past with techniques as diverse as micropipette aspiration [29], deformation in a flow [30], AFM [31], acoustic force spectroscopy (AFS) [32] and laser optical tweezers (LOT) [24, 33, 34]. The emergent picture of such studies is that the dynamical response of a RBC depends on the type of perturbation applied, the geometry of the experimental configuration and the measured physicochemical property. For instance, mechanical stiffness measurements have reported values that change by two orders of magnitude depending on the pulling orientation, the type of bond attachment and contact area of the probe. Noise correlation spectroscopy has emerged as an excellent technique to investigate rheological phenomena and active behavior of RBC, e.g. using LOT [35–38]. This type of spectroscopy is specially suited to measure membrane fluctuations (flickering) in the high-frequency domain (sub-second timescale). In the low-frequency domain ($\geq$1s) active fluctuations and nonequilibrium phenomena are observed [38, 39]. In particular, the power spectrum of the flickering signal at low frequencies increases with ATP concentration contributing to an average entropy production of hundreds of k_BT/s [38]. A quantitative characterization of relaxational phenomena of RBC in the low-frequency domain contributes to a better understanding of RBC haemostasis [40].

Chapter 6

Pulling and relaxation experiments of red blood cells

In our experimental configuration a single RBC is attached to two micron-sized beads, each one at opposite ends of the cell. The lower bead (LB) is immobilized by air suction on the tip of a micropipette (MP) whereas the upper bead (UB) is captured in the optical trap (OT) (Figure 6.1a). The experimental configuration is achieved by a series of manual operations where beads are captured with the optical trap and attached to the RBC. A flow is applied to the RBC to keep it far from the laser focus to avoid optical damage of the RBC by direct illumination [41] (See Appendix D for further details). Two kind of experiments have been performed: pulling and extension-jump experiments. The RBC is repeatedly stretched back and forth between a minimum and a maximum force in pulling experiments, and the force-extension curve (FEC) is measured. A step-jump is applied to the trap position in extension-jump experiments, and the subsequent force relaxation curve (FRC) is measured.

6.1 Pulling experiments

Figure 6.1b (left) shows FECs of a single RBC repeatedly pulled between 0 and 30pN. The first stretch-release pulling cycle (left panel, grey) systematically deviates from the following ones (left panel, black)

in agreement with previous results [42]. Initially, the RBC is fully relaxed (point A). Upon pulling, the RBC is mechanically elongated until reaching 30pN (point B). Then the trap is moved backward at the same speed, and the elongation decreased until reaching 0pN, at which point a remanent elongation of $\sim 0.5\mu m$ is observed (point C and zoom). We interpret the remanent elongation as the irreversible orientation of the RBC that occurs in the first pulling cycle. The same phenomenon is observed in ferromagnetic materials where the initial magnetization curve differs from the rest due to the irreversible motion of the domain walls [43]. Figure 6.1b (right panel) shows FECs for three different RBC which present mechanical hysteresis between the stretching (dark color) and releasing (light color) parts of the cycle (upward vs downward arrows). FECs show cell-to-cell variability indicating heterogeneous mechanical response of the RBC population (Fig. 6.1b, right panel). From the FECs, we also extracted the (elongational) stiffness of the RBC defined as the slope of the FEC between 7.5 and 12.5 pN. The RBC stiffness histogram is shown in (Fig 6.1c) giving a mean value $5 \pm 3\text{pN}/\mu\text{m}$. This value is compatible with previous experimental and simulation results using LOT [44].

In some cases, we also found the formation of a tether after reaching sufficiently high forces. This is shown in Figure 6.1d, where two tethers, each at one side of the RBC, are extruded at forces above $\simeq$ 20pN [1]. Figure 6.1e (left) shows the first five pulling cycles of a single RBC in the presence of a tether. Like in the untethered case, a remanent elongation is observed after completing the first pulling cycle, with the first pulling curve (grey) being different from the following ones (black). Starting at initial zero force and elongation (point A), the RBC is stretched until it reaches 30pN (point B). Then, the trap is moved backward at the same speed, and force is released down to zero (point C). Figure 6.1e (left, zoom) shows the remanent elongation after the first pulling cycle ($\sim 0.5\mu m$) while Figure 6.1e (right) shows FECs for three different RBCs with tether formation.

[1] We have also observed cases where a single tether is extruded in one of the two sides (indistinctly)

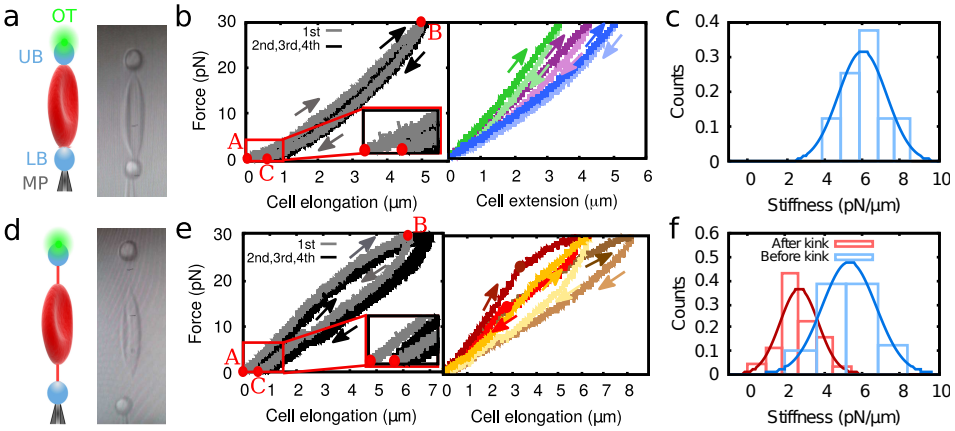

Figure 6.1: Representation of the two different RBCs populations, with and without tether, and the cell variability inside each population. (**a**) Schematics and video image of our experimental configuration of the untethered population where the lower micro-sized bead (LB) is fixed on the micropipette (MP) and the upper bead (UB) is immobilized by the optical trap (OT) shown in green. (**b**) (Left panel) First five force-extension curves of a RBC without tether. In black, the first FEC showing a remanent elongation and, in grey, the consecutive four FEC that overlap with each other. (Right panel) FECs for 3 different RBC, each one represented with a different color, pulling trace (from 0pN to 30 pN) is represented in dark color while the pushing trace (from 30 pN to 0pN) is represented in light color. (**c**) Histogram of untethered RBC stiffness obtained from the FECs of 8 different RBCs. The stiffness is computed by performing a linear fit of the FEC between 7.5pN and 12.5 pN. (**d**) Schematics and video image of our experimental configuration of the tethered population. In the image, the RBC present two tethers, one attached to each bead, but it is also possible to have RBCs with only one tether in the lower or upper bead. (**e**) (Left panel) First five FECs of a RBC with tether. In black, the first FEC that presents a remanent elongation and, in grey, the consecutive four FEC which overlap with each other. (Right panel) Force-extension curves for 3 different RBCs (different colors) in the presence of tether. The dark color represent the curve from 0pN to 30pN and the light color represent the curve from 30pN to 0pN. (**f**) Stiffness histogram for the pulling FECs in the presence of tether. In blue, the values computed before the kink and, in red, the values after the kink (indicated as a dot in panel e, right).

Note that FECs with tether show higher hysteresis than those without tether (Figure 6.1b and e, right). Tether formation is observed as the detachment of one of the two beads from the RBC at a given force. Concomitantly, a kink appears in the FEC at that force and the stiffness decreases (due to the combined stiffness of the serially connected tether and cell body). The same phenomenon is observed in the releasing process: a kink appears in the FEC upon tether absorption by the cell membrane. Notice that RBCs with a tether also show cell-to-cell variability and heterogeneous mechanical response across the RBC population (Figure 6.1e, right). Tether extrusion and absorption are cooperative processes that occur at characteristic forces (shown as dots for one RBC in Figure 6.1e, right). Tether formation is an irreversible process showing hysteresis: tether extrusion occurs at forces that are higher than tether absorption (Figure 6.2).

We also carried out experiments using beads functionalized with concanavalin A known to specifically attach to the spectrin network, finding results comparable to those shown in Figure 6.1. In particular, we also found the same spread in cell-to-cell variability as for non-specific attachments, suggesting that heterogeneous mechanical response is an intrinsic feature of RBCs (Figure 6.3).

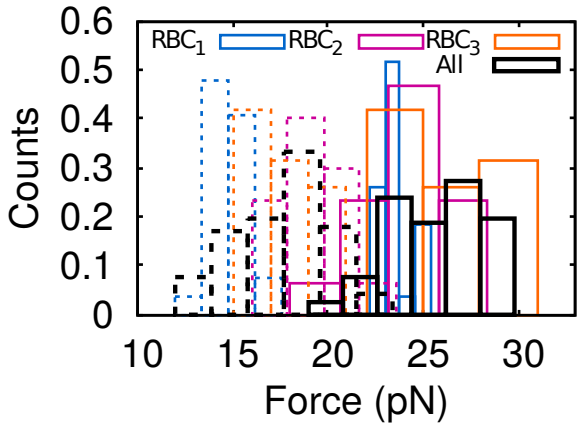

Figure 6.2: Force histograms of extrusion and absorption of tether in pulling experiments. In continuous lines, extrusion force histograms of three different RBCs (colors) together with the average (black). In dashed lines, absorption force histograms of three different RBCs (colors) together with the average (black).

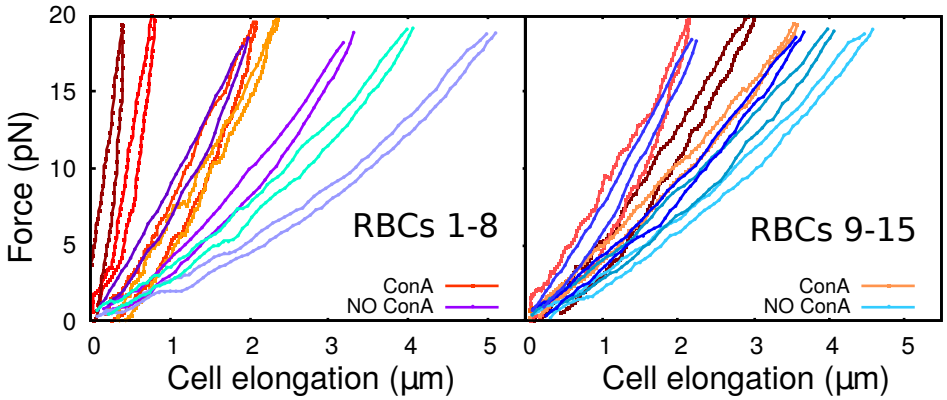

Figure 6.3: Concanavilin A coating in pulling experiments. Force extension curves for 15 different RBC. Bluish colors represent FEC without ConA coating and reddish FEC represent RBC with ConA coating. FECs have been divided in two panels indifferently in order to facilitate their visualization.

6.2 Extension-jump experiments

The bloodstream cyclically transports RBCs in order to deliver oxygen to body tissues. RBCs get oxygenated in the lung during the circulation cycle being pumped throughout the body for cellular respiration. During this process, RBCs travel inside constrained environments in arteries and veins squeezing when passing through narrow capillaries (of width comparable to the RBC size). RBCs also experience large deformations when filtered by the sinusoids in the spleen. Therefore, RBCs continuously experience mechanical stress in vivo, showing the importance of understanding their mechanical response using biophysical techniques (mechanical phenotyping).

RBCs have a complex architecture consisting of two major structures: the membrane lipid bilayer and the 2D spectrin-actin network. From mechanical stretching experiments, it is not easy to separate the individual contributions from each structure. Here we introduce a new approach based on dynamical phenotyping (DP) to separate the contribution of different structural elements to RBC deformation. To this end, relaxational processes in RBC are investigated in the time domain by applying a sudden extension-jump while the stress evolution is monitored. We have performed a series of extension-jump

protocols and measured force relaxation curves over four decades in time (0.01-300 seconds). These measurements permit us to find well-separated and reproducible timescales in RBCs and relate them to specific structural responses.

Four different kinds of extension-jump protocols have been performed (Fig.6.4a). These are characterized by the sign of the extension jump (tensional or compressive) and the shape of stepwise jumps. Extension jumps are applied by a sudden displacement $\Delta\lambda$ ($\sim 1-2\mu$m), of the trap position, being positive for tensional jumps (Fig.6.4a, upper panels) and negative for compressive jumps (Fig.6.4a, lower panels). A single timescale $\tau_0 = 5$ min defines the time between consecutive jumps (time axis in Fig.6.4a, bottom). Trap displacement leads to a force jump, $\Delta F = F_f - F_i$, where F_i is the initial force before the jump, and F_f is the force immediately after the jump (Fig.6.4b). Force relaxation curves (FRCs) are measured immediately after the jump, starting at F_f and during a time equal to $\tau_0 = 5$min (Fig.6.4b). We will label relaxation curves by ΔF, being positive (negative) for tensional (compressive) jumps. Step wise jumps are of two kinds: trotter-type and ladder-type protocols. In trotter protocols the initial force (F_i) stays close to zero ($F_i = 0-5$pN) for tensional jumps (Fig.6.4b, brown) and, the final force (F_f) stays close to zero for compressive jumps (Fig.6.4b, dark green). In ladder protocols, extension-jumps are consecutively applied (Fig.6.4a, orange and light green) and FRCs measured at every step (Fig.6.4b, orange and light green). In all protocols, several jumps (between 2 and 5) of varying amplitude (ΔF) were applied, the total experimental time per RBC being approximately half an hour.

FRCs in Fig.6.4b show a viscoelastic response after RBC deformation. For tensional jumps ($\Delta\lambda, \Delta F > 0$, upper panels) force monotonically decreases with time indicating RBC expansion. For compressive jumps ($\Delta\lambda, \Delta F < 0$, lower panels) force monotonically increases with time indicating RBC contraction. For all protocols, FRCs slowly decay over minutes reaching a stationary value higher (lower) than the initial force F_i for tensional (compressive) protocols. Remarkably, all FRCs show a triple exponential behavior (Figure 6.4c),

$$F(t) = A_1 e^{-t/\tau_1} + A_2 e^{-t/\tau_2} + A_3 e^{-t/\tau_3} + F_s \tag{6.1}$$

where A_1, A_2, A_3 are amplitudes, τ_1, τ_2, τ_3 are the corresponding relax-

ation times, and F_s is the stationary force in the large time limit.

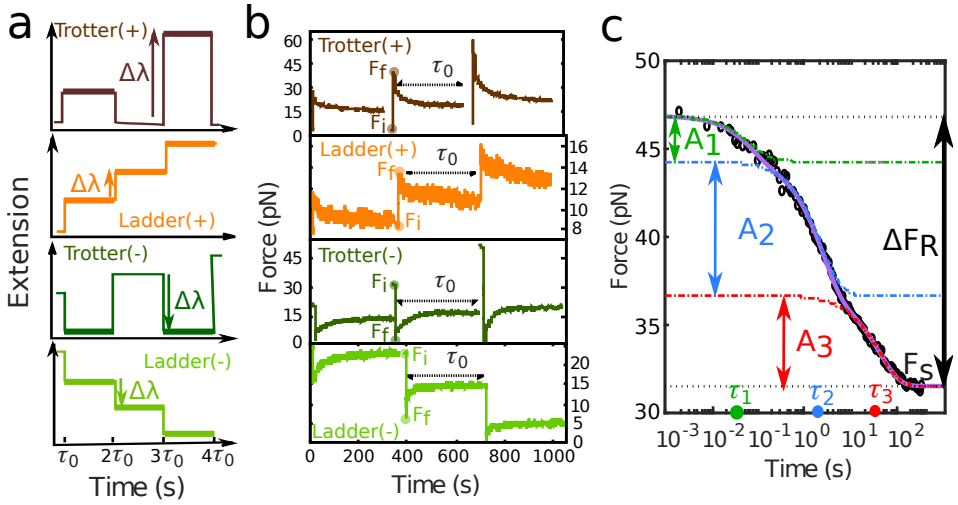

Figure 6.4: Protocols and three exponentials fit. (**a**) Schematic representation of the trap displacement versus time for the four different protocols (trotter(+), ladder(+), trotter(-) and ladder(-)). In thick lines, the time windows during which measurements are performed. The arrow next to $\Delta\lambda$ indicates the direction of the jump. (**b**) Three force relaxation curves for each of the four different protocols presented in (a). Initial and final forces indicated with big dots in the second FRC of each panel. (**c**) Force relaxation curve in normal-log scale. Every data point is the result of a box car average filter. The fitting curve Eq. 6.1 is represented in purple. In grey, the parameters of the first exponential (A_1 and τ_1); in red, the parameters of the second exponential (A_2 and τ_2); and in blue, the parameters of the third exponential (A_3 and τ_3). The stationary force, F_s, is represented as a dotted line at the bottom.

In Figure 6.4c we illustrate the parameters of the triple exponential for one relaxation curve of the Trotter(+)-type. A crucial feature of the FRC is the recovery force ΔF_R, which is equal to the total relaxation of the force after the deformation jump. From Eq. 6.1 this is given by $\Delta F_R = F(t=0) - F_s = A_1 + A_2 + A_3$ (Fig. 6.4c). If $\Delta F_R = 0$, the RBC response is fully elastic whereas if $\Delta F_R = \Delta F$ it is mainly inelastic and the RBC fully recovers the original stress before the jump. ΔF_R is a measure of the viscous response of the RBC after it has been deformed. ΔF_R is approximately half of the

total force jump, ΔF, being positive (negative) for tensional (compressive) deformations. Therefore the RBC partially recovers the initial force F_i before the deformation jump, demonstrating strong viscoelastic response and memory effects. This behavior has been reported in previous studies of RBCs [44], epithelial cells [45] and other materials such as shape memory polymers [46]. Figure 6.5 shows four selected FRCs with different protocols for the cases of RBCs without tether (panels a) and with (panels b) tether extrusion. Results have been fitted to Eq. 6.1 (black curves). FRCs are qualitatively the same for RBC without or with tether extrusion, in all cases a triple exponential fits the data. Other functions such as a double exponential and a stretched exponential fit the data worse (Fig. 6.6).

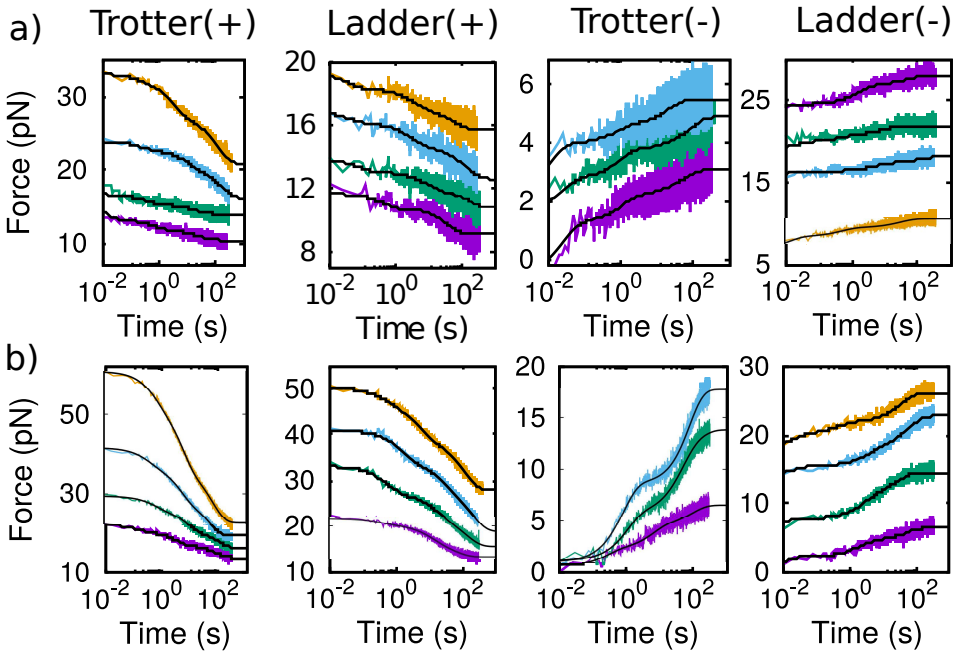

Figure 6.5: Experimental force relaxation curves for the four different protocols. Force versus time in normal-log scale. Each panel shows the raw data (dark color) of experimental curves with an average (light color), and their corresponding fits (black) for one of the four different protocols. Each color represents a relaxation curve with a different ΔF. (**a**) For the untethered population and (**b**) for the tethered population.

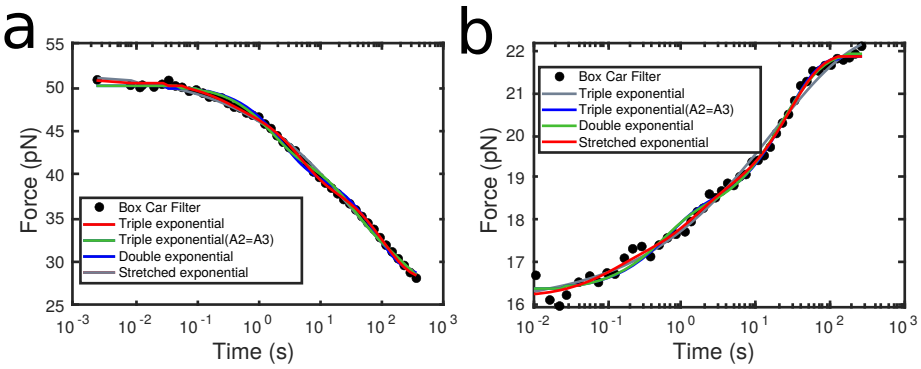

Figure 6.6: Force relaxation curve with different fits. Boxcar filter of the FRC (black points) with fits to triple exponential (red), triple exponential imposing second amplitude equal to third one (green), double exponential (blue), and stretched exponential (grey). FRCs shown for ((**a**) Trotter (+) and (**b**) Ladder(-).

Figure 6.8 shows all the parameters of the fits (amplitudes and relaxation times) plotted versus the force jump ΔF. Results have been averaged over the different protocols (Trotter(+) with Ladder (+) for $\Delta F > 0$ and Trotter(-) with Ladder (-) for $\Delta F < 0$). As shown in Figure 6.7, the three amplitudes similarly scale with ΔF for the different protocols.

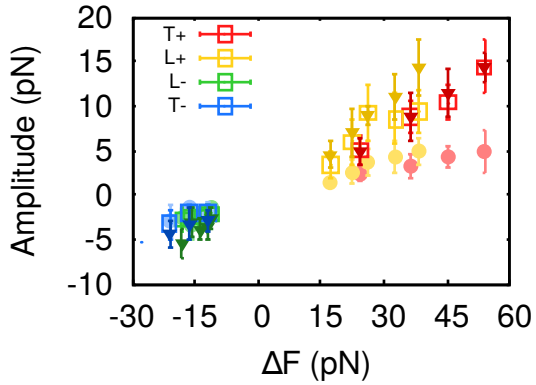

Figure 6.7: Amplitudes for the different protocols. Amplitudes as a function of ΔF for Trotter(+) in red, Ladder(+) in yellow, Trotter(-) in blue, and Ladder(-) in green. Circles represent the first amplitude, squares represent the second amplitude, and triangles represent the third amplitude.

However, at a closer inspection, fitting parameters show a systematic difference between untethered and tethered RBCs. Therefore fitting parameters are shown separately for the untethered and tethered cases, each point being the average over 3-6 different RBCs. In Figure 6.8a, we plot the recovery force ΔF_R versus ΔF, untethered (black circles) and tethered (grey circles). A distinct linear relationship is found in both cases, $\Delta F_R = 0.42(2)\Delta F$ (untethered) and $\Delta F_R = 0.67(2)\Delta F$ (tethered) showing higher viscous response (i.e. larger recovery force) for tethered RBCs. The higher viscosity of the extruded tether leads to higher hysteresis as observed in the FECs (Fig. 6.1 e). Notice the narrower range of ΔF values in the untethered case ($-25pN < \Delta F < 25pN$), due to tether extrusion above 30pN. Figure 6.8b shows the three amplitudes A_1 (green circles), A_2 (blue squares), A_3 (red triangles) plotted versus ΔF averaged over the different protocols. Again, a linear relationship is observed for the three amplitudes in the tethered (light color) and untethered (dark color) cases. Interestingly, a similar linear dependence is observed for A_2 and A_3 (blue and red symbols), which differs for A_1 (green symbols). Indeed, amplitudes A_2, A_3 are compatible with each other for the tethered and untethered cases. A single linear fit to A_2 and A_3 putting all data together gives $A_{23} = 0.27(3)\Delta F$ (tether, light grey area) and $A_{23} = 0.15(2\Delta F$ (untethered, dark grey area). In contrast, for the lowest amplitude A_1, similar values are obtained for the untethered (dark green) and tethered (light green) cases that can be fitted to the single linear relation $A_1 = 0.11(1)\Delta F$.

These results for the amplitudes suggest that A_1 is related to the hydrodynamic drag force between the bead and the area of contact wit the BRC. If the contact is local then there should not be distinction between the tethered and untethered case. In contrast, A_2 and A_3 describe two relaxation processes depending in the morphology of the RBC. In fact, the two amplitudes are comparable with each other suggests that the RBC's structural elements contributing to this response are subjected to the same force (i.e. as if they were serially connected). This might explain why A_2 and A_3 differ between the tether and untethered morphologies. Further information can be obtained from the relaxation times τ_1, τ_2, τ_3. The results are shown in Fig. 6.8c. Remarkably, we find three distinc well-separated timescales that are independent on the value of ΔF and the protocol, demonstrating

that these are intrinsic to the RBC. Moreover, these timescales are the same for tethered and untethered cases, with exception of τ_1 which is larger for the tethered case. In fact, tether extrusion upon applying a positive force jump ΔF causes the RBC's membrane to flow from the RBC body toward the tether.

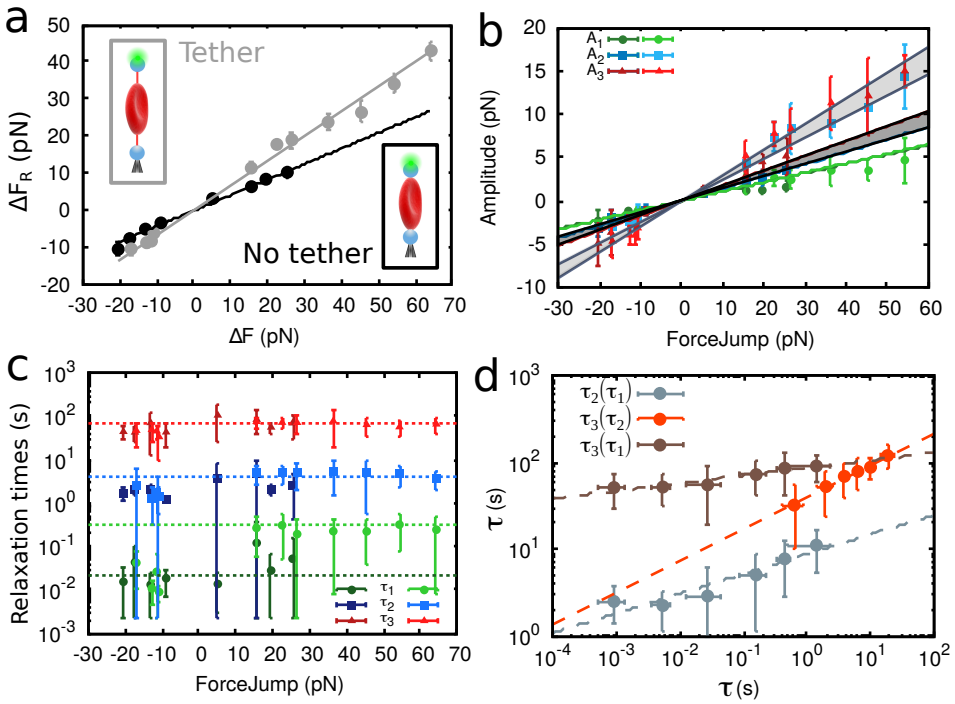

Figure 6.8: Amplitudes, relaxation times and restored forces. (**a**) Amplitudes as a function of ΔF for both RBCs populations. In light color untethered case and, in dark color, tethered case. Grey-black represent the first amplitude, dark-light red represent the second amplitude and dark-light blue represent the third amplitude. (**b**) Characteristic times as a function of ΔF for both tethered and untethered cases. In light color untethered case and, in dark color, tethered case. Grey-black represent the first characteristic time, dark-light red represent the second characteristic time and dark-light blue represent the third characteristic time. (**c**) Sum of the three amplitudes as a function of ΔF. In dark blue tethered case and in light blue untethered case. (**d**) .

In fact, upon retraction of the RBC ($\Delta F < 0$), τ_1 is the same for the untethered and tethered RBC (left most green points in Fig.

6.8c). Video images of RBC's retraction show that the tether is not immediately absorbed by RBC's body exhibiting the apparent asymmetry of τ_1 for $\Delta F > 0$ and $\Delta F < 0$. As the tether immediately relaxes upon retraction, the timescale τ_1 is that of the RBC's body membrane alone. The large timescales τ_2, τ_3 pertain to the response of the RBC's body being equal for the tethered and untethered cases. Averaging the values of the relaxation times over the ΔF values and the tethered-untethered cases, we get $\tau_2 = 4.0(5)$s, $\tau_3 = 70(5)$s. For τ_1, we separate the positive force jump data (light green circles, for $\Delta F > 0$) for tethered case from the rest of τ_1 data, obtaining $\tau_1^{tethered}(\Delta F > 0) = 0.30(5)s$ while $\tau_1 = 0.020(5)s$ for the other cases.

Finally, timescales τ_1, τ_2, τ_3 exhibit a strong heterogeneity varying between one and three orders of magnitude across the RBC population. Despite this variability, the timescales are strongly correlated with each other showing a sort of dynamic scaling. This is shown in Figure 6.8d where we plot them relative to each other. Interestingly, a power law describes the timescales dependencies $\tau_i = \alpha\tau_j^{\beta}$ with $i, j = 1, 2, 3$ and α and β positive constants. While τ_1 varies over three orders of magnitude, τ_2 and τ_3 do over just one or two. In particular, $\tau_2 = 9(1)\tau_1^{0.23(4)}$ (grey points), $\tau_3 = 40(2)\tau_2^{0.37(2)}$ (orange points), $\tau_3 = 87(4)\tau_1^{0.09(1)}$ (brown points).

6.3 Discussion and conclusions

In Chapter 6, we have studied the mechanical deformability of RBC using a miniaturized dual-beam counterpropagating LOT [47]. We carry out pulling and force relaxation experiments following an extension step jump to determine the temporal dependence of cell internal processes. A central question we aim to answer is whether there are characteristic relaxational timescales or, instead, the system is intrinsically free of timescales. Our results demonstrate that RBC exhibits three well-separated timescales spanning three orders of magnitude with a novel kind of stress and strain relaxational behavior that we call discrete-stretched exponential behavior. This new kind of relaxation response is intermediate between the pure exponential relaxation observed in linear and two-level systems [48] and the more complex stretched-exponential relaxation observed in polymers and glassy mat-

ter [49].

6.4 Future Perspectives

In Chapter 6, we have identified three processes in the relaxation curves of RBCs. Each process is characterized by an amplitude A, and a relaxation time, τ. A plausible explanation for these distinct process relates then to the RBC components (cellular membrane and 2D spectrin-actin network). However, an experimental proof is lacking. In order to do so, we will perform relaxation experiments in disrupted RBCs following two different approaches. The first approach will be the depletion of ATP, which is crucial in structural cell stability. In this case, we will alter both the membrane and the protein network. The second approach will consist in eliminating the spectrin-actin network to remain only with the RBC membrane. The product of this procedure is the so-called ghost RBC. This method will allow us to decouple the contribution of the membrane from the contribution of the protein network. We expect to obtain deviations in both amplitudes and relaxation times for each type of disrupted RBC. The study of the deviations will be essential for the complete understanding of the three relaxation processes.

Chapter 7

Soft-glass rheological model for red blood cells

In this chapter, we study the mechanics of Red Blood Cells (RBCs) and how it evolves in time from the perspective of a mechanical model. In particular, we model the pulling and relaxation experiments of RBCs presented in Chapter 6. The experimental configuration (Fig. 7.1a) consists of a RBC hold between two beads, the lower one (LB) is fixed on the tip of a micropipette (MP), and the upper one (UB) is captured in the optical trap (red lines).

Pulling experiments (Fig. 7.1b) are performed by moving the optical trap up at a constant velocity (stretching process represented in dark green) until reaching a given maximum force, f_{max}. In the figure, $f_{max} = 20$pN and the pulling velocity is $v = 140$nm/s. Once f_{max} is reached, the trap moves backwards at the same velocity until reaching $f = 0$pN. In the relaxation experiments (Fig. 7.1c) the optical trap is suddenly moved a distance $\Delta\lambda$ and the force relaxation measured during five minutes.

In both pulling and relaxation experiments, we control the trap position λ while measuring the force (Fig. 7.2a left). λ is defined as the distance between the center of the lower bead and the center of the optical trap,

$$\lambda = 2r + x_c + x_b \tag{7.1}$$

where r is the bead radius, x_c is the cellular extension, and x_b is the bead position relative to the trap center. As the bead radius r is

a constant, an increment of the trap position $\Delta\lambda$ will be distributed between x_b and x_c,

$$\Delta\lambda = \Delta x_c + \Delta x_b \tag{7.2}$$

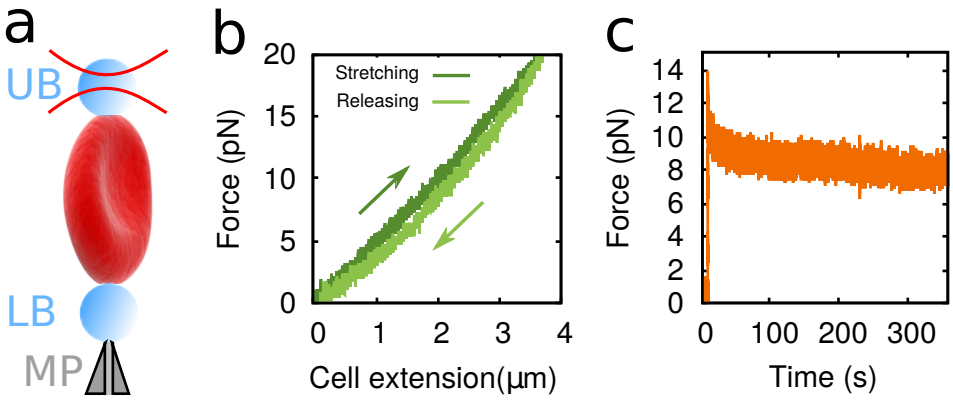

Figure 7.1: Experimental force-extension and force-relaxation curves. (**a**) Experimental configuration in pulling and relaxation experiments. The RBC is held between two beads (blue spheres), the lower one (LB) is fixed on the tip of the micropipette (MP) by air suction, and the upper one (UB) is optically trapped. (**b**) Experimental force-extension curve of a RBC where the stretching (releasing) parts of the cycle are shown in dark (light) green. (**c**) Experimental force-relaxation curve of a RBC after a deformation step jump is applied on a relaxed RBC. The force rises to a maximum value and then relaxes over time.

7.1 Disordered blobs model (DBM)

In order to simulate the experiments, we model the RBC as a one-dimensional chain formed by N blobs (binary large objects in Fig. 7.2a, right). Each blob can be in two different states: compact ($\sigma = 0$) or extended ($\sigma = 1$) (Fig. 7.2a right). The state of each blob is determined by a free energy landscape, which varies with force (Fig. 7.2b). In the disordered blobs model (DBM), the free energy landscape of each blob has different parameters extracted from a mathematical distribution (see below).

The free energy landscape of a blob has two minima corresponding to the two states, and is characterized by two extensions (x_i^m, $x_i^\dagger$)

and two energies (b_i,Δg_i). x_i^m stands for the extension between the extended and compact states. $x_i^\dagger$ is the distance of the transition state to the compact state. The barrier b_i^0 is the energy maximum at the transition state that the blob must overcome to go from compact to the extended state. Δg_i is the free energy difference between the extended and compact states where $1 \geq i \geq N$ represents the index of a blob.

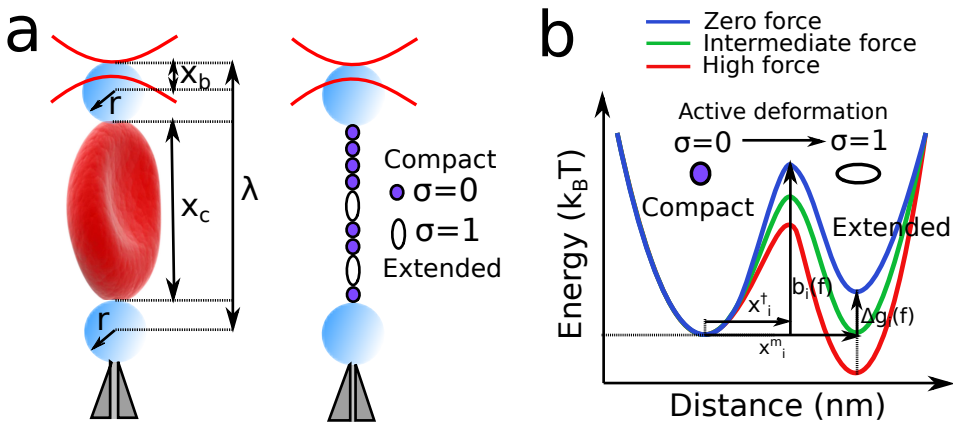

Figure 7.2: Two-state model and energy landscape. (**a**) In left panel, experimental configuration of the RBC indicating the control parameter λ, the RBC extension, x_c, the bead-trap extension, x_b, and the bead radius r. In the right panel, schematics of RBC disordered blob model. The RBC is modeled as a one-dimensional chain of blobs (binary large object) that can be compact (purple circle) or extended (white oval). (**b**) Free Energy landscape of the DBM characterized by two minima that correspond to each blob state compact on the left and extended on the right). $b_i(f)$ is the force-dependent energy barrier between the two states, $\Delta g_i(f)$ is the force-dependent free-energy difference between the two minima; $x_i^\dagger$ is the distance between the compact state and the transition state and, x_i^m is the distance between the compact and extended states. Notice that as force increases, both $b_i(f)$ and $\Delta g_i(f)$ decrease.

The energies $b_i(f)$ and $\Delta g_i(f)$ vary linearly with force,

$$b_i(f) = b_{i0} - f x_i^\dagger \tag{7.3}$$

$$\Delta g_i(f) = \Delta g_{i0} - f x_i^m \tag{7.4}$$

where b_{i0} and Δg_{i0} are the extrapolated values at zero force.

7.2 Monte-Carlo simulations

We perform a stochastic Monte Carlo (MC) simulation of the model for pulling and relaxation experiments. The difference between the pulling and the step jump protocol lies on how the control parameter λ changes at each iteration.

7.2.1 Pulling protocol

For each iteration (MC sweep), the simulation reproduces the trap movement by gradually increasing λ,

$$\lambda(t + dt) = \lambda(t) + vdt \tag{7.5}$$

where v is the pulling velocity and dt is the timestep. Once the $f_{max} = 20$pN is reached, the program starts decreasing the value of the control parameter λ as,

$$\lambda(t + dt) = \lambda(t) - vdt \tag{7.6}$$

Iterations are performed until reaching the experimental minimum force, $f_{min} = 0$pN. At this point, a pulling cycle has been completed (Fig. 7.3 blue).

7.2.2 Step-jump protocol

For the relaxation case, we apply a given $\Delta\lambda$ at $t = 0$s. Initially, $\Delta\lambda$ leads to an irreversible jump, $\Delta x_{b,0}$, with a corresponding force of $f_0 = k_b \Delta x_{b,0}$. Subsequently after, $\Delta\lambda$ remains constant (Fig. 7.3, red), however, as times goes by, it is distributed between Δx_b and Δx_c (Eq. 7.2). At each iteration, the initial energy distributions $b_{i,0}$ and $\Delta g_{i,0}$ will be modified according to Eqs. 7.3 and 7.4. After 250s (25000 sweeps and $2.5 \cdot 10^7$ steps), the simulation stops.

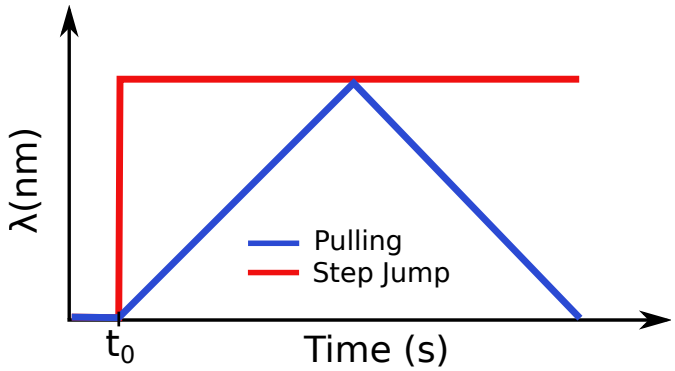

Figure 7.3: Trap position (λ) time evolution. Schematics of the control parameter λ versus time for the pulling protocol (blue) and the step jump protocol (red). In the pulling protocol, λ increases with a constant velocity until a maximum value and then decreases with the same speed until the initial value. In the step jump protocol, at initial time t_0, λ suddenly jumps to a maximum value and subsequently remains constant.

7.2.3 Monte-Carlo algorithm

The system consists in two elements, the bead and the RBC. The bead is captured in an optical trap which follows the linear relation,

$$f = x_b k_b \tag{7.7}$$

where k_b is the trap stiffness. At the same time, we model the RBC according to the worm-like chain (WLC) elastic model,

$$f(x) = \frac{k_B T}{p}\left[\frac{1}{4(1-x/L)^2} - \frac{1}{4} + \frac{x}{L}\right] \tag{7.8}$$

where k_B is the Boltzmann constant, T is the temperature, p is the persistence length, x is the RBC extension, f is the force, and L is the RBC contour length expressed as,

$$L = \sum_{i=1}^{N} \sigma_i x_i^m \tag{7.9}$$

where x_i^m is the extension for i blob.

In order to perform the simulation, the MC algorithm follows the next steps:

- The RBC is initialized with all the blobs in the compact state ($\sigma_i = 0$). At $t_0 = 0$s, $f = 0$pN and $\Delta\lambda = 0$nm.

- From λ value (sections 7.2.1 ans 7.2.2), we compute the RBC extention, x_c, assuming mechanical equilibrium between the trap force and the force of the RBC, $f_{trap} = f_{RBC}$.

- From x_c value and Eq. 7.1, the trap-bead extension x_b is computed.

- The force is computed using Eq. 7.7 assuming a constant k_b value.

- From the force value, we sequentially and randomly select N=1000 blobs of the blob chain and update their state following the kinetic rates,

$$k_{0\to1} = k_m e^{-b_i(f)/k_B T} \tag{7.10}$$

$$k_{1\to0} = k_m e^{(-b_i(f)+\Delta g_i(f))/k_B T} \tag{7.11}$$

  where k_m is the microscopic rate defined as how many times per second a blob tries to change its state, $0 \to 1$ corresponds to go from the compact(0) to the extended(1) state, and $1 \to 0$ vice versa.

- Accepting/rejecting a blob update. The probability of a blob to change state equals the product of the kinetic rate $k_{\sigma\to1-\sigma}$ (Eqs. 7.10 and 7.11) and the timestep dt. If the probability is larger than a random number uniformly distributed between 0 and 1, a transition will be accepted.

- Updating the contour length, L. Every time a blob goes from the compact state ($\sigma = 0$) to the extended one ($\sigma = 1$), it releases a certain amount of extension x_m to the total length of the RBC, represented by L, the counter length. On the reverse process, when a blob is extended and a transition to the compact state is accepted, L will decrease by x_m.

To map the MC simulation time into real time, we compare the real time unit $dt = 0.01$s with one MC sweep. The latter is equal to N random sequentially MC steps, with one step being the updating of one individual blob. Therefore, in every MC sweep, N values chosen blobs are updated.

7.3 Experimental data comparison

The initial distributions of the distances (x_i^m, $x_i^\dagger$) and the energies ($b_{i,0}$, $\Delta g_{i,0}$) determines the outcome of the simulation. Realistic initial distributions need to satisfy some conditions: for each individual blob, the barrier b_i has to be larger than the energy difference between the two states Δg_i and both must be positive ($b_{i,0} > \Delta g_{i,0} > 0$).

In particular, we implement three different sets of distance and energy distributions (Fig. 7.4).

- **Homogeneous model (HM).** The first case of distributions is the homogeneous non-disorder soft-glass mechanical (SGM) model where all parameters are constant (red bins in Fig. 7.4a). The values of x_i^m, $x_i^\dagger$, $b_{i,0}$ and $\Delta g_{i,0}$ have been taken from a similar model applied to reproduce DNA condensation in the presence of dendrimers [50]. The FEC for the homogeneous distributions, is shown in Figure 7.4b (red), which presents three different regions: an initial sudden increase of the force, a shoulder, and a final region where the force increases until reaching 20pN. Notice that in this case, the curve presents a negligible hysteresis between the stretching (dark red) and the realising (light red) processes.

- **Gaussian model (GM).** In the second case, the energy landscape parameters are random Gaussian distributed (Fig. 7.4a blue histograms). The Gaussian distributions are obtained by introducing a variance to the previous homogeneous values (red bins). In this case, the FEC (Fig. 7.4b blue) also presents three regions; however, the transitions between them are smoother than in the homogeneous case, and hysteresis appears throughout the force range.

- **Exponential energy model (EEM).** The third model is the random exponential distribution. In this model x_i^m, $x_i^\dagger$ are Gaussian distributed, but $b_{i,0}$, $\Delta g_{i,0}$ are exponentially distributed. The FEC (green curve in Fig. 7.4b) shows no shoulder. Instead, the stretching curve (dark green) presents an almost linear force increase. Moreover, hysteresis is present in the whole force range, reproducing the shape of the experimental data (Fig. 7.4b) qualitatively. In order to obtain the green FEC, we modify the energy distributions respect to the Gaussian case as observed in Figure 7.4a, green bins. We decrease the Δg_0 values and we define a wider range of b_0. As shown in Figure 7.4c, the best model fitting to the pulling experiments is the FEC with exponentially distributed energies.

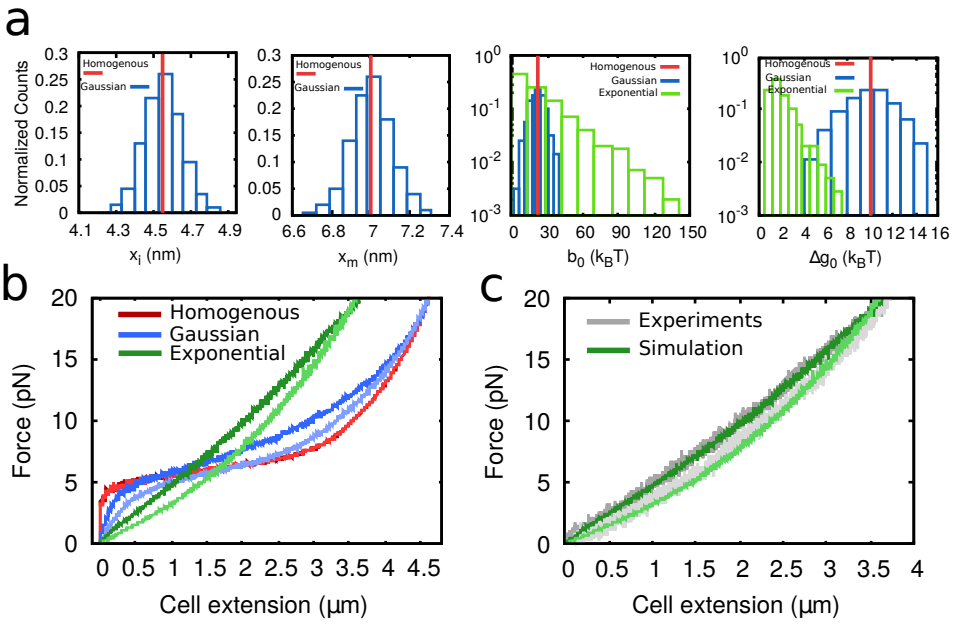

Figure 7.4: Energy distributions and pulling results. (**a**) Initial distributions for x_i^m, $x_i^\dagger$, $b_{i,0}$ and $\Delta g_{i,0}$. Histograms of homogeneous distributions (red), random Gaussian distributions (blue), and random exponential distributions (green). (**b**) Simulated FEC for the three parameters distributions. Dark colors represent the stretching process, and light colors the releasing process. (**c**) Comparison between experimental data and simulations using the exponentially distributed parameters model.

The EEM successfully reproduces the pulling experimental data, therefore, we apply the same model to the relaxation experiments. In the relaxation experiments, the control parameter λ jumps by $\Delta\lambda$ at time $t_0 = 0$s and remains constant over five minutes. We obtain the simulated relaxation curve (Fig. 7.5a red) by imposing the experimental value of $\Delta\lambda$ in the algorithm. The simulation underestimates the force reached right after applying the jump $\Delta\lambda$ and does not present three relaxation processes as observed in Chapter 6, however, it reproduces the general trend of the experimental data (Fig. 7.5a blue).

The underestimation of the maximum force could be due to the fact that we are missing an elastic term in the DBM. In the model the jump $\Delta\lambda$ is performed during a single iteration while, in the experiment, $\Delta\lambda$ jumps are divided into sub-steps. Another experimental limitation that could affect the force's fast response is the contact area between the RBC and the bead. Although the beads are coated with Concanaviline A, which specifically binds to sugars in the RBC membrane, we do not control the exact contact area. Moreover, the RBC population is composed by cells of different ages, and therefore, it is heterogeneous in terms of stiffness and size.

Even so, the simulations using a DBM reproduce the linearity between the force jump ΔF and the recovery force ΔF_{rec} after 250s (Fig. 7.5b in blue points), which is a significant feature of the experimental data. The simulated points (Figure 7.5b, red) are computed by changing the initial control parameter $\Delta\lambda$. Notice that the algorithm assumes $\Delta F = F_{max}$ as F_{min} is always equal to 0pN. However, the experimental data may not fulfill this condition as sometimes $F_{min} \neq 0$pN.

In Figure 7.5b, we show the linear fits for both experimental and simulated data,

$$\Delta F_{rec} = (0.44 \pm 0.01)\Delta F \tag{7.12}$$

$$\Delta F_{rec} = (0.428 \pm 0.009)\Delta F \tag{7.13}$$

Notice that the simulated fit is in very good agreement with the experimental one.

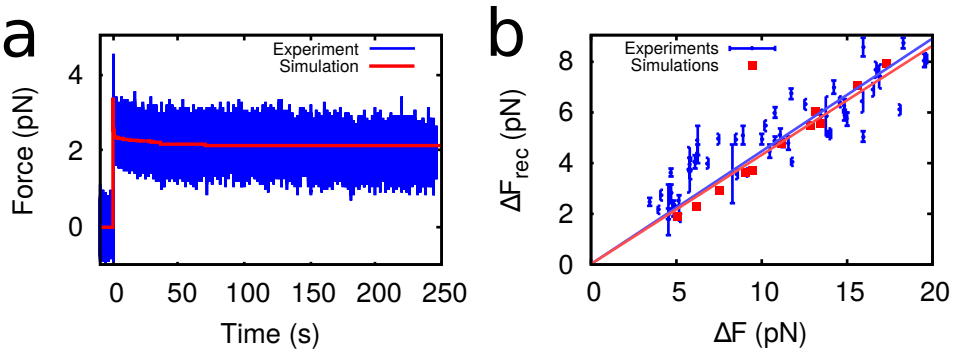

Figure 7.5: Relaxation curves and linear response relation. (**a**) Comparison between one experimental force-relaxation curve (blue) and simulations using the EEM (red). (**b**) Recovery force, ΔF_{rec}, as a function of force jump, ΔF, for experimental curves (blue points) and simulations (red squares) together with their corresponding linear fits.

7.4 Discussion and conclusions

We have introduced a soft-glass rheology model (the disordered blobs model) that reproduces the experimental RBC pulling and force relaxation curves measured with optical tweezers. Moreover, the worm-like chain (WLC) model describes the force generated by the RBC and the stress behavior in continuous strain deformation (pulling) and strain jump deformation (relaxation) experiments.

Using pulling experimental curves, we have been able to tune and determine how the different distributions of the distances, x_i^m and $x_i^\dagger$, and the energies, $b_{i,0}$ and $\Delta g_{i,0}$, affect the shape of the FEC.

In addition, exponential distributions for b_i and Δg_i properly reproduce the experimental data. However, small deviations of these distributions can substantially change both the pulling and the relaxation curves.

In the case of relaxation simulations, the linear relation between the simulated pair of values ΔF_{rec} and ΔF is in very good agreement with the experimental results.

Chapter 8

High-frequency force spectroscopy of red blood cells

In the present chapter, we study the passive fluctuations of red blood cell (RBC) through noise measurements using laser optical tweezers (LOT).

The measurements are performed in the experimental configuration shown in Figure 8.1a where a RBC is held between two beads. The lower bead is fixed on the tip of the micropipette, while the upper bead is captured in the optical trap. We measure the force signal of a RBC at rest during a minute (Fig. 8.1b). For each force signal, we compute the force power spectrum (FPS) (Fig. 8.1c, blue lines) together with the corresponding boxcar (BC) average filter (red points).

In Figure 8.1d, we show the FPS of a single RBC at seven different trap stiffnesses (each trap stiffness represented in circles of different colors). Considering that the integral of the FPS is equal to the variance of the signal, we observe how the force variance decreases as the trap stiffness does (Fig. 8.1d). The trap stiffness is measured by fitting the FPS of the bead without the RBC (Chapter 4 subsection 4.4.1.3).

As shown in Figure 8.1e, we measure the FPS of three RBCs for each trap stiffness. Each RBC is represented with a different symbol (RBC1 in squares, RBC2 in triangles, and RBC3 in circles). Notice that the FPS of the three different RBC taken at $k_b = 5.2\text{pN}/\mu\text{m}$ are compatible with each other showing a high reproducibility.

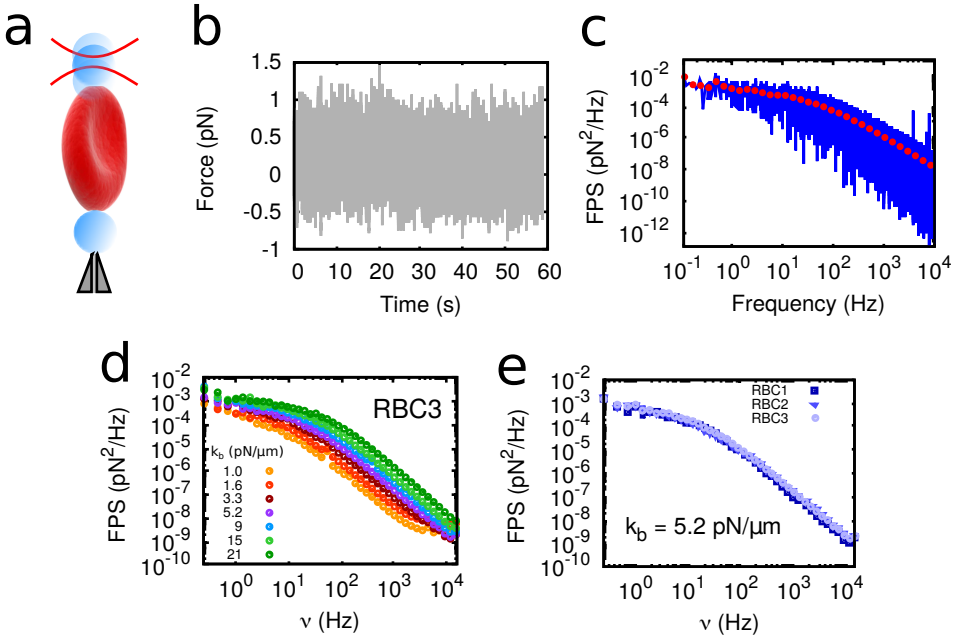

Figure 8.1: Experimental data and power spectra. (**a**) Experimental configuration where the bead captured in the optical trap is attached to the RBC membrane. (**b**) Force signal. (**c**) Force power spectrum (FPS) (blue lines) together with its corresponding boxcar average filter (red points). (**d**) Boxcar average of the force power spectrum of a single RBC at seven trap stiffnesses represented in different colors. (**e**) Boxcar average of the FPS of three RBCs measured at $k_b = 5.2\text{pN}/\mu\text{m}$. Each RBC is represented with a different symbol and a different tonality of purple.

By the equipartition theorem, the variance of the position of an optically trapped object equals,

$$\sigma_x^2 = \langle x(t)^2 \rangle - \langle x(t) \rangle^2 = \frac{k_B T}{k_T} \tag{8.1}$$

where k_T is the total stiffness applied to the object. In the trap-RBC configuration, k_b is the trap stiffness and k_{RBC} is the RBC stiffness. In Appendix E, we demonstrate that the total stiffness for the this kind of configuration is equal to the sum of the two contributions, $k_T = k_b + k_{RBC}$. Hence, to measure RBC activity, it is necessary to reduce the optical trap stiffness as much as possible. Therefore, the active signal of RBCs should increase as k_b decreases. As we measure the force signal, Eq. 8.1 is rewritten as,

$$\frac{\sigma_f^2}{k_b^2} = \frac{k_B T}{k_b + k_{RBC}} \tag{8.2}$$

where the variance of the force is equal to $\sigma_f^2 = \sigma_x^2 k_b^2$.

8.1 Measuring the force variance

From a 60s force singal, we determine the force variance for five different time windows (TW) (colored rectangles in Fig. 8.2, 10s in blue, 5s in light green, 1s in dark green, 0.1s in brown, and 0.01s in orange). For each time window, we divide the signal in $N = 60\text{s/TW}$ sub-signals having $N = 6$ sub-signals in the case of TW = 10s. The N sub-signals are averaged to compute a single variance value for each TW.

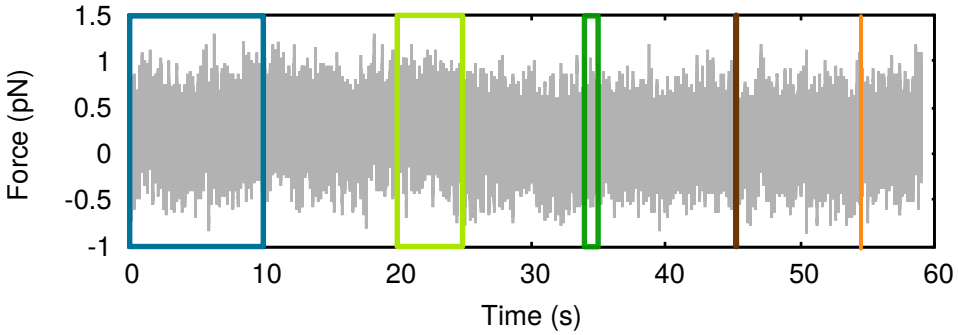

Figure 8.2: Computing force variance. Force signal of 60 seconds with five different time windows: 10s, 5s, 1s, 0.1s, and 0.01s represented in dark blue, light green, dark green, brown, and orange, respectively.

We present two different approaches in order to quantify the RBC activity from force variances using Equation 8.2. The first method measures the viscoelasticity of the RBC at different time windows. In the second procedure, we fix the RBC stiffness from pulling experiments, k_{RBC} (pulling velocity $v = 140\text{nm/s}$) and we compute the corresponding effective temperature.

8.2 Viscoelastic dependence of k_{RBC}

The first method measures the RBC stiffness for each k_b and TW. Rewriting the force variance from Eq. 8.2 as a function of the trap stiffness, we obtain the following relation,

$$\frac{k_B T}{\sigma_f^2} = \frac{1}{k_b} + \frac{k_{RBC}}{k_b^2} \tag{8.3}$$

where $\frac{k_B T}{\sigma_f^2}$ shows a quadratic dependence on $1/k_b$.

In Figure 8.3a, we show the experimental data of $k_B T/\sigma_f^2$ versus k_{RBC}/k_b, with its corresponding fit to a quadratic function being the vertical dashed line the condition $k_{RBC} = k_b$. For every quadratic fit, we extract a value k_{RBC}. Notice the difference between k_{RBC} obtained from pulling experiments and k_{RBC} as the result of the quadratic fit.

Eq. 8.3 is derived from the equipartition relation and valid in equilibrium conditions. For $k_{RBC} < k_b$ (left of the vertical dash line, Fig. 8.3), all time window sets are in good agreement with the quadratic behavior. However, for $k_{RBC} > k_b$ (right of the vertical dash line, Fig. 8.3), the experimental data are systematically below the quadratic prediction for equilibrium. Additionally, we observe an increase of this discrepancy with the time window value.

In Figure 8.3b, we present the RBC stiffness values obtained by fitting Eq. 8.3 to experimental data for the three different RBCs. Each RBC is represented with a different symbol and tonality of red. The horizontal red lines stand for the three different k_{RBC} values obtained from pulling data.

For the shorter time window we obtain a RBC stiffness compatible or larger than the one obtained from pulling experiments (horizontal lines in Fig. 8.3b). On the other hand, as the time window increases, the RBC stiffness decreases showing a cell softening for large times.

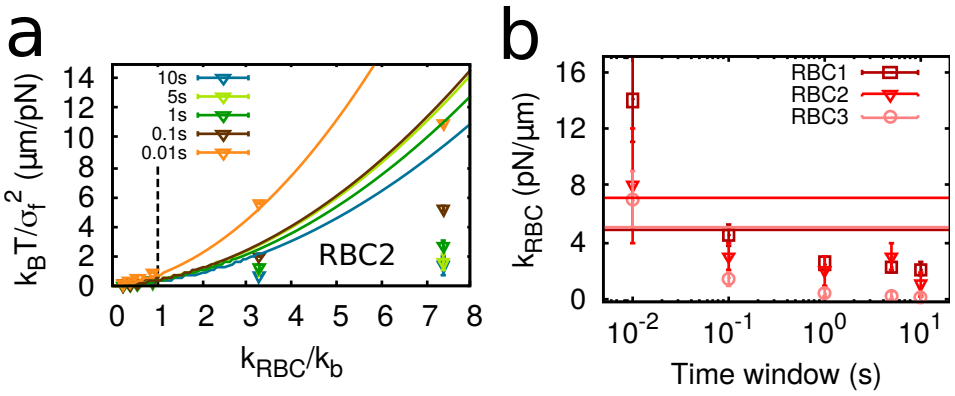

Figure 8.3: RBC stiffness from force variance. (**a**) k_BT divided by force variance as a function of k_{RBC} divided by trap stiffness k_b. We show a single RBC where each color represents a different time window. Experimental data represented as triangles, and quadratic fits to Eq. 8.3 represented in solid lines. The vertical dash line represents the condition where the trap stiffness equals the RBC stiffness obtained from pulling experiments. (**b**) RBC stiffness obtained by the quadratic fit to Eq. 8.3 versus the time window for three RBCs. Each RBC is represented with a different symbol and a different tonality of red. Horizontal lines represent the values of RBC stiffness obtained from pulling experiments.

8.3 Effective-temperature measurements

For each of the three RBC, we measure a pulling cycle ($v = 140$nm/s at $k_b = 60$pN/μm). Performing a linear fit into the force-extension curve (FEC), we measure the RBC stiffness, k_{RBC}. From the cellular stiffness, k_{RBC}^{pull}, for each RBC, we compute the effective temperature rewritting Eq. 8.2 as,

$$T_{eff} = \frac{\sigma_f^2(k_b + k_{RBC}^{pull})}{k_B k_b^2} \tag{8.4}$$

The effective temperature quantifies how far from equilibrium a system is. In particular, we explore the effective temperature in order to identify activity of the RBC. If the obtained effective temperature is larger than the real one (298K), it means that the system is out of equilibrium and active.

In Figure 8.4a, we show the effective temperature divided by the real one (298K) versus the ratio k_{RBC}/k_b. The horizontal dashed line indicates the equilibrium condition $T_{eff} = T_{real}$, while the vertical dashed line shows the limit where $k_{RBC} = k_b$.

For a constant trap stiffness value, the effective temperature increases with the time window. The fact that the effective temperature becomes larger than the environmental value ($T_{eff} > T_{env} = 298$K), indicates that activity appears at larger time windows.

For the larger trap stiffness, $k_b = 21$pN/μm, we recover the equilibrium condition except for the shorter time window 0.01s. For all the time windows, the effective temperature increases as the trap stiffness decreases. As expected, the non-equilibrium effects of the RBC ($T_{eff} > T_{env}$) appears by reducing the trap contribution to the fluctuations. In fact, the larger values of the effective temperature, which indicate higher activity, are in the $k_b < k_{RBC}$ regime.

In Figure 8.4b, we compare the effective temperature ratio (T_{eff}/T_{env}) plotted versus the stiffness ratio (k_{RBC}/k_b) of three RBCs for $TW =$ 10s. Each RBC is represented in a different symbol and tonality of blue. For all RBC $T_{eff} > T_{env}$ at low k_b values, indicating non-equilibrium effects. Interestingly, RBC2 and RBC3 show a larger activity than RBC1.

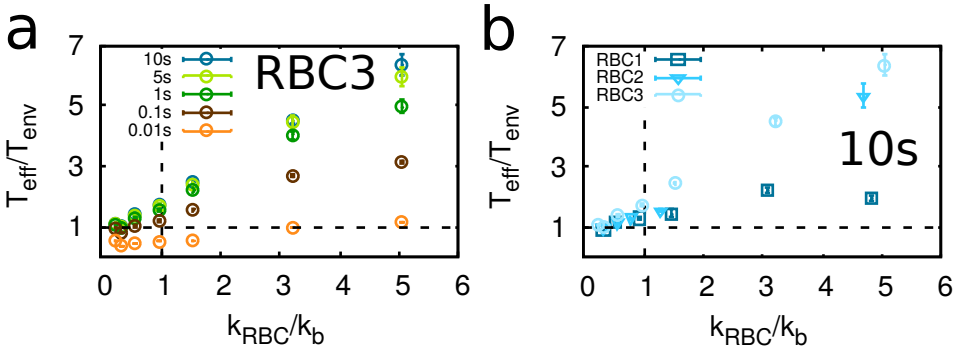

Figure 8.4: RBC effective temperature at different trap stiffnesses. Effective temperature divided by the environmental temperature versus k_{RBC}/k_b. The horizontal dashed line represents the condition $T_{eff} = T_{env}$, and the vertical dashed line $k_b = k_{RBC}$. (**a**) Single RBC where each time window is represented in different colors. (**b**) 10s time window of three RBCs. Each RBC is represented with a different symbol and a different tonality of blue.

8.4 Discussion and conclusions

From the equipartition theorem, we develop two methods to quantify the non-equilibrium effects and activity of the RBCs by changing the trap stiffness. The first method measures the RBC viscoelasticity by computing the RBC stiffness for each time window. The second method computes the effective temperature of the RBC assuming a constant RBC stiffness obtained from the pulling experiments.

In the first method, we recover equilibrium for large values of k_b and obtain deviations from equilibrium as k_b decreases. We observe a softening of the RBC as the time window increases.

In the second method, we check that, for large values of k_b, we recover equilibrium as the effective temperatures are compatible with the real temperature (298K). On the other hand, we observe that as we decrease the trap contribution to position fluctuations by reducing the trap stiffness k_b, the effective temperature increases. It means that when $k_{RBC} > k_b$, we measure $T_{eff} > 298$K detecting activity.

8.5 Future Perspectives

In Chapter 8, we have measured force signals at zero force with a stiffness range between 1 and 21 pN/μm. However, instead of decreasing the trap stiffness, one might keep the k_b value at 60pN/μm and apply force to the system.

In Figure 8.5a, we show the power spectra of a single RBC at seven different forces (circles of different colors, being the black squares the power spectrum of a bead alone at zero force at $k_b = 60$pN/μm). We distinguish two regions, the low-frequency regime corresponding to effects at long times, and the high-frequency regime where the power spectrum decreases following a power decay.

In the low-frequency regime, we observe that, in the presence of force, the RBC power spectrum lies above the bead power spectrum. Moreover, we observe how the area below the RBC power spectra (colored circles), and therefore the force variance, increases with force. This result suggests that activity increases with supplied stress to the RBCs.

On the other hand, we detect a slight variation of the power decay exponent in the high-frequency regime. In Figure 8.5b results

for ten different RBCs are shown (each point represents a fit to a power spectrum). Notice that at zero force, the RBC power spectra reproduce the expected -2 exponent typical of the Lorentzian shape, $S(\nu) = A/(\nu^2 + \nu_c^2)$. Nevertheless, as force increases, the exponent decreases in absolute value until reaching a constant value around -1.85.

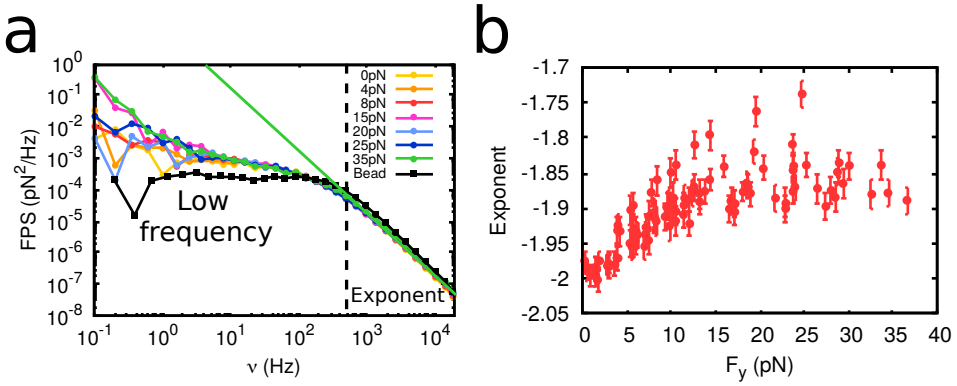

Figure 8.5: RBC force power spectra at high trap stiffness at different forces. (**a**) Force power spectra of a single RBC at different forces (each color represents a different force value). In black squares, the power spectrum of a single bead. The vertical dash line represents the corner frequency of the bead force power spectrum. (**b**) Exponent obtained by fitting the high-frequency range of the force power spectra as a function of the force applied to the RBC for ten different RBCs.

From these preliminary results, we plan to apply the two methods developed in Chapter 8 to data obtained from stressed RBCs measured at high trap stiffness values. This way, we will prove if the RBC activity can also be measured and detected under these conditions and if the effect of reducing the trap stiffness is comparable to the effect of applying a force.

Part IV

Stochastic thermodynamics of molecules and cells

Chapter 9

Variance sum rule for entropy production

9.1 Introduction

In 1865, German physicist Rudolf Clausius coined the term entropy to quantify the amount of heat that can be converted to work. Later on, Boltzmann, Gibbs, and Maxwell interpreted entropy as a statistical quantity related to the number of micro-states or configurations that a system can explore in a given macrostate. This probabilistic interpretation led to relate entropy and information in the 20th century.

In complex systems such as proteins, genetic material, molecular motors, and various cell types, the number of different micro-states for a given macrostate is huge. Living systems are constantly dissipating energy and producing entropy. Therefore, biological processes are irreversible (e.g. development, growth, aging, etc.) operating under nonequilibrium conditions. Hence, the quantification of the entropy production is critical to understand how life works.

Until now, physicists and mathematicians have been able to analytically derive lower bounds of the entropy production rate in nonequilibrium systems. A prominent example is the thermodynamic uncertainty relation (TUR) which provides a lower bound for the entropy production in nonequilibrium steady states (NESS).However, for biological applications, these lower bounds are too loose meaning that they are far below actual entropy production rates. For example, molecular motors hydrolyze ATP to translocate in a stepwise manner

(e.g. helicases unwinding DNA which hydrolyze one ATP molecule every few number of basepairs). However, at every step the energy required for translocating, in physilogical conditions, is one order of magnitude lower the available free energy per step ($\simeq 20k_B$T). From a practical point of view, these lower bounds do not provide accurate estimates of the entropy production rate of the system of interest. Hence, it is essential to derive exact relations for entropy production rates that are amenable to experimental verification, useful to characterize complex systems' non-equilibrium effects fully.

In this chapter, we introduce a new relation based on the sum of variances of physical quantities of the system such as displacement and cumulative force in noise-correlation spectroscopy experiments. We validate this relation for systems in equilibrium and out of equilibrium, such as beads optically trapped with and without a flow. We also investigate the applicability of the variance sum rule to molecular systems. In particular, we apply it to DNA hairpins in their folded and unfolded states. We also consider the stochastic switching trap (SST) as an example of an exactly solvable nonequilibrium model, and derive an analytical expression for the entropy production rate. The SST model might be used to reproduce the nonequilibrium processes of active systems, such as RBC, to directly measure their entropy production rates. A few preliminary results are presented and future perspectives discussed.

This chapter is the result of a fruitful collaboration with Ivan di Terlizzi and Marco Baiesi at the University of Padova (Italy). The results of this chapter are part of a common paper [51].

9.2 An illustrative example: the bead in the optical trap

As introduced in Chapter 3, the Langevin equation for a bead captured in an optical trap is,

$$m\frac{d^2x}{dt^2} + \gamma\frac{dx}{dt} + kx = f(t) + \eta(t) \tag{9.1}$$

where m is the mass, x is the bead position, γ is the friction coefficient , k is the trap stiffness, f is the force and $\eta(t)$ is the noise

with $\langle \eta(t) \rangle = 0$ and $\langle \eta(t)\eta(s) \rangle = 2k_B T\gamma\delta(t-s)$. In overdamped limit ($m = 0$), Eq. 9.1 is rewritten as,

$$\gamma \frac{dx}{dt} + kx = f(t) + \eta(t) \tag{9.2}$$

Equation 9.2 can be solved in the absence of external force, $f = 0$. We get for $x(t)$,

$$x(t) = x_0 e^{-kt/\gamma} + \frac{1}{\gamma}\int_0^t \eta(s) e^{-k(t-s)/\gamma} ds \tag{9.3}$$

which decays to 0 in equilibirum $\langle x(t \to \infty) \rangle = 0$. The average of the position is,

$$\langle x(t) \rangle = x_0 e^{-kt/\gamma} \tag{9.4}$$

Equation 9.4 defines the relaxation time of the bead, $\tau_R = \gamma/k$.

The second moment of x is,

$$\begin{aligned}
\langle x^2(t) \rangle &= \langle x_0^2 e^{-2t/\tau_R} \rangle + \langle \frac{1}{\gamma^2}\int_0^t ds_1 \int_0^t \eta(t)\eta(s) e^{-(t-s_1-s_2)/\tau_R} ds_2 \rangle \\
&+ \langle 2x_0 e^{-t/\tau_R} \frac{1}{\gamma}\int_0^t \eta(s) e^{-(t-s)/\tau_R} ds \rangle \\
&= x_0^2 e^{-2t/\tau_R} + \frac{1}{\gamma^2}\int_0^t ds_1 \int_0^t 2k_B T\gamma\delta(s_1 - s_2) e^{-(t-s_1-s_2)/\tau_R} ds_2
\end{aligned} \tag{9.5}$$

then,

$$\begin{aligned}
\langle x^2(t) \rangle &= x_0^2 e^{-2t/\tau_R} + \frac{2k_B T}{\gamma}\int_0^t e^{-2(t-s)/\tau_R} ds \\
&= x_0^2 e^{-2t/\tau_R} + \frac{k_B T}{k}\left(1 - e^{-2(t-s)/\tau_R}\right)
\end{aligned} \tag{9.6}$$

so, the position variance $V_x = \langle x^2(t) \rangle - \langle x(t) \rangle^2$ is equal to,

$$V_x = \frac{k_B T}{k}\left(1 - e^{-2t/\tau_R}\right) \tag{9.7}$$

In equilibrium ($t \to \infty$), $V_x = \frac{k_B T}{k}$. Important for the calculus below is the equilibrium correlation function $C(t) = \langle x(0)x(t)\rangle$. It can be shown that,

$$\frac{\partial C}{\partial t} = \frac{k}{\gamma} C(t) \tag{9.8}$$

where,

$$C(t) = \frac{k_B T}{k} e^{-t/\tau_R} \tag{9.9}$$

9.2.1 Displacement variance

The bead's displacement is defined as $\Delta x(t) = x(t) - x(0)$. Its variance is given by,

$$\sigma^2_{\Delta x} = \langle (x(t) - x(0))^2 \rangle - \langle (x(t) - x(0)) \rangle^2 \tag{9.10}$$

developing the averages we obtain,

$$\sigma^2_{\Delta x} = \sigma^2_{x(t)} + \sigma^2_{x(0)} - 2C(t) \tag{9.11}$$

For long times t, $C(t) \to 0$ and the variance of the displacement, the position evaluated at two different times, is expressed as,

$$\sigma^2_{\Delta x} = \sigma^2_{x(t)} + \sigma^2_{x(0)} = \frac{2k_B T}{k_b} \tag{9.12}$$

which is twice $V_x(t \to \infty)$ Eq. 9.7. Generalizing $\sigma^2_{\Delta x}$ for any t, the following expression is obtained,

$$\sigma^2_{\Delta x}(t) = \frac{2k_B T}{k_b}(1 - e^{-t/\tau_R}) \tag{9.13}$$

where τ_R is the relaxation time which is defined as,

$$\tau_R = \frac{\gamma}{k_b} \tag{9.14}$$

where γ is the friction coefficient. For simplicity, we express the displacement variance as $V_{\Delta x} = \sigma^2_{\Delta x}$.

9.2.2 Cumulative force variance

The force is given by $f = kx(t)$. We define the cumulative force between 0 and t as,

$$\Sigma_f = \int_0^t f(s)ds = k\int_0^t x(s)ds \tag{9.15}$$

Squaring Eq. 9.16 and averaging it, we get,

$$\langle \Sigma_f^2 \rangle = k^2 \int_0^t ds_1 \int_0^t \langle x(s_1)x(s_2)\rangle ds_2 \tag{9.16}$$

where $C(t,s) = \langle x(s_1)x(s_2)\rangle$ for $(t > s)$ and is given by,

$$C(t,s) = \frac{k_B T}{k} e^{-(t-s)/\tau_R} \tag{9.17}$$

Inserting Eq. 9.17 into Eq. 9.16,

$$\begin{aligned}
\langle \Sigma_f^2 \rangle &= k^2 \int_0^t ds_1 \int_0^t \frac{k_B T}{k} e^{-|s_1-s_2|/\tau_R} ds_2 \\
&= 2k_B T\gamma \int_0^t ds_1 (1 - e^{-s_1/\tau_R}) \\
&= 2k_B T\gamma \left[t - \tau_R(1 - e^{-t/\tau_R})\right]
\end{aligned} \tag{9.18}$$

The variance of the cumulative force is,

$$V_{\Sigma_f}(t) = 2k_B T\gamma t(1 - \frac{\tau_R}{t}(1 - e^{-t/\tau_R})) \tag{9.19}$$

9.2.3 Variance sum rule

Combining the displacement and cumulative force variances, we obtain a simple expression for the sum of the variances in equilibrium conditions that only depends on the friction coefficient γ,

$$V_{\Delta x} + \frac{V_{\Sigma_f}}{\gamma^2} = \frac{2k_B T t}{\gamma} = 2Dt \tag{9.20}$$

where $D = k_B T/\gamma$ is the diffusion coefficient. For simplicity, we will express the sum of the two variances as $V_T = V_{\Delta x} + V_{\Sigma_f}/\gamma^2$.

Variances $V_{\Delta x}$,V_{Σ_f}, and V_T have dimensions of nm^2. Assuming $V_{\Delta x} = V_{\Delta f}/k_b^2$, where $V_{\Delta f} = \sigma^2_{\Delta f}$, it is possible to compute the displacement variance and the sum of the variances directly from the force signal alone without assuming a trap stiffness value. In this way, Eqs. 9.13 and 9.47 can be rewritten as,

$$V_{\Delta f} = 2k_BTk_b(1 - e^{-t/\tau_R}) \tag{9.21}$$

$$\frac{V_{\Delta f}}{k_b^2} + \frac{V_{\Sigma_f}}{\gamma^2} = \frac{2k_BTt}{\gamma} \tag{9.22}$$

9.3 Variance sum rule in a flow

The former variance sum rule can be generalized to arbitrary (not only quadratic) potentials for nonequilibirum steady states (NESS). Defining the Langevin equation for one particle in a flow for any type of potential U,

$$\dot{x}(t) = -\frac{U'(x(t) - \lambda(t))}{\gamma} + \eta(t) \tag{9.23}$$

where $\eta = \sqrt{2k_BT\gamma} \cdot \xi(t)$, with $\langle \eta(t) \rangle = 0$ and $\langle \eta(t)\eta(s) \rangle = 2k_BT\gamma\delta(t - s)$. Let us consider a stationary moving potential so $\lambda(t) = vt$. Let's change variable as $x \to y = x - vt$ where v is the flow velocity. Then, we rewrite Eq. 9.23 as,

$$\gamma\dot{y}(t) = -V'(y(t)) + \eta(t) \tag{9.24}$$

where $V'(y) = \gamma v + U'(y)$. For the displacement we have,

$$\Delta_x(t) = y(t) - y(0) + vt = \Delta y(t) + vt \tag{9.25}$$

and the work is given be,

$$W(t) = -v \int_0^t U'(y(s))ds \tag{9.26}$$

Integrating Eq. 9.24, we obtain,

$$\gamma\Delta_x(t) = \frac{W(t)}{v} + \int_0^t \eta(s)ds \tag{9.27}$$

From Eq. 9.27, we compute the variances $V_{\Delta x}$ and V_W in the non-equilibrium steady state (NESS). From Eq. 9.25,

$$\langle \Delta_x(t) \rangle = vt \tag{9.28}$$

Then, we compute $\langle W(t) \rangle$ by averaging over the noise Eqs. 9.27 and using 9.28,

$$\langle W(t) \rangle = v^2 \gamma t \tag{9.29}$$

To calculate $\langle W^2(t) \rangle$ we square Eq. 9.27, and average over the noise,

$$\frac{\langle W^2(t) \rangle}{v^2\gamma^2} = \langle \Delta_x^2(t) \rangle + 2Dt - \frac{2}{\gamma}\int_0^t \langle \Delta_x(t)\eta(s) \rangle ds \tag{9.30}$$

where $D = k_B T/\gamma$. We define the response function $G(t,s)$ as,

$$G(t,s) = \langle \frac{\delta \Delta x(t)}{\delta \eta(s)} \rangle = \langle \frac{\delta x(t)}{\delta \eta(s)} \rangle = \frac{1}{2k_B T\gamma} \langle x(t)\eta(s) \rangle = \frac{1}{2k_B T\gamma} \langle \Delta x(t)\eta(s) \rangle \tag{9.31}$$

From Eqs. 9.28 and 9.31 we get for the last term of Eq. 9.30,

$$\int_0^t \langle \Delta x(t)\eta(s) \rangle ds = 2k_B T\gamma \int_0^t G(t,s) ds = 2k_B T\gamma \chi(t) \tag{9.32}$$

where the susceptibility $\chi(t)$ is,

$$\chi(t) = \int_0^t G(t,s) ds \tag{9.33}$$

In the NESS, there is time-translational invariance (TTI) and the FDT holds. The correlation function $C(t,s)$ with $(t \geq s)$ considering TTI is,

$$C(t,s) = \langle y(t)y(s) \rangle = C(t-s) \tag{9.34}$$

and the response function,

$$G(t,s) = G(t-s)\Theta_H(t-s) \tag{9.35}$$

where $\Theta_H(t-s)$ is the Heaviside theta function. Then the FDT is given by,

$$\frac{\partial C(t)}{\partial t} = -k_B T G(t) \tag{9.36}$$

Inserting Eq. 9.36 in Eq. 9.33 we get,

$$\chi(t) = \frac{1}{k_B T}(C(0) - C(t)) \tag{9.37}$$

Combining Eq. 9.37 with Eq. 9.25,

$$\langle \Delta x^2(t) \rangle = v^2 t^2 + 2 k_B T \chi(t) \tag{9.38}$$

We insert it into Eq. 9.32 into Eq. 9.30,

$$\frac{\langle W^2(t) \rangle}{v^2 \gamma^2} = \langle \Delta x^2(t) \rangle + 2Dt - 4 k_B T \chi(t) \tag{9.39}$$

Using Eq. 9.38 we get,

$$\frac{\langle W^2(t) \rangle}{v^2 \gamma^2} = -\langle \Delta x^2(t) \rangle + 2Dt + 2v^2 t^2 \tag{9.40}$$

From Eq. 9.28 we rewrite Eq. 9.40 as,

$$\frac{\langle W^2(t) \rangle}{v^2 \gamma^2} = -\langle \Delta x^2(t) \rangle + 2Dt + 2\langle \Delta x(t) \rangle^2 \tag{9.41}$$

Using Eq. 9.29 and using $\langle W \rangle = \gamma v \langle \Delta x \rangle$ we get,

$$\frac{V_W}{v^2 \gamma^2} = \frac{\langle W^2(t) \rangle}{v^2 \gamma^2} - \frac{\langle W(t) \rangle^2}{v^2 \gamma^2} = \frac{\langle W^2(t) \rangle}{v^2 \gamma^2} - 2\langle \Delta x(t) \rangle^2 \tag{9.42}$$

which yields the variance sum rule,

$$V_{\Delta x} + \frac{V_W}{v^2 \gamma^2} = +2Dt \tag{9.43}$$

for the variance of the displacement $V_{\Delta x}$ and the variance of the work V_W.

9.4 Equilibrium variance sum rule

In the absence of a flow, $v = 0$, we can rewrite the variance sum rule in terms of the cumulative force Σ_f,

$$\Sigma_f(t) = -\int_0^t U'(y(s))ds \tag{9.44}$$

where from Eq. 9.26 $\Sigma_f(t) = W(t)/v$ is the cumulative force. Rewritting Eq. 9.27 in terms of $\Sigma_f(t)$ we get,

$$\gamma\Delta x(t) = \Sigma_f(t) + \int_0^t \eta(s)ds \tag{9.45}$$

Then we rewrite Eq. 9.30 as,

$$\frac{\langle\Sigma_f^2(t)\rangle}{\gamma^2} = \langle\Delta x^2(t)\rangle + 2Dt - \frac{2}{\gamma}\int_0^t \langle\Delta x(t)\eta(s)\rangle ds \tag{9.46}$$

Repeating the same procedure shown in section 9.3, we obtain a variance sum rule that depends on the variance of the cumulative force V_{Σ_f} instead of the variance of the work V_W.

$$V_{\Delta x} + \frac{V_{\Sigma_f}}{\gamma^2} = 2Dt \tag{9.47}$$

The variance sum rule Eq. 9.47 can be extracted in many ways. It can be demostrated to be valid for N particles systems (where Δx stands for the mass center displacement) and f or W is the external total force and work applied to the system. It can be also generalized to arbitrary NESS that do not fulfill the FDT (unlike the simple stationary moving potential case). The Langevin equation for such kind of systems is,

$$\gamma\dot{x}(t) = f(x) + \eta(t) \tag{9.48}$$

where $f_t(x)$ is an arbitrary time-dependent force that produces a NESS. The system is time-translational invariant but the FDT (Eq. 9.36) has a violation factor,

$$X(t)\frac{\partial C(t)}{\partial t} = -k_B T C(t) \tag{9.49}$$

where $X(t)$ is the fluctuation dissipation ratio, also written as,

$$X(t) = \frac{T}{T_{eff}} \tag{9.50}$$

where T_{eff} is a time-dependent effective temperature. One can derive a variance sum rule also in this case

$$V_{\Delta x} + \frac{V_{\Sigma_f}}{\gamma^2} = 2Dt + E(t) \tag{9.51}$$

where $E(t) = 2(V_{\Delta x}(t) - 2k_B T\chi(t))$. Taking the susceptibility for the stationary moving potential case Eq. 9.38, we verify that $E(t)$ vanishes recovering Eq. 9.47.

Finally, a variance sum rule can be also derived for Non-Markovian systems that have a memory kernel $\Gamma(t)$ and satisfy the Langevin equation,

$$\int_{-\infty}^{t} \Gamma(t-s)\dot{x}(s)ds = f(x(t)) + \eta(t) \tag{9.52}$$

In this case, a correction term can be observed in the variance sum rule which also depends on the memory kernel $\Gamma(t)$. These and other results can be found in [51].

9.5 Experimental results

9.5.1 Bead with and without flow

To validate the equilibrium case, we capture a single calibration bead of $3.00(2)\mu$m of diameter in the optical trap (Fig. 9.1a) with trap stiffness $k_b = 60(5)\text{pN}/\mu\text{m}$. The experiments are performed in Milli-Q water at 298K being the medium viscosity $\eta = 8.90 \cdot 10^{-4}\text{Pa} \cdot \text{s}$. The friction coefficient for spherical objects is,

$$\gamma = 6\pi\eta r \tag{9.53}$$

where η is the medium viscosity and r is the radius of the object. In the bead case, the friction coefficient takes a value of $\gamma = 2.5(3) \cdot 10^{-2}\text{pN} \cdot \text{s}/\mu\text{m}$ and therefore, a relaxation time (Eq. 9.14) of $\tau_R = 0.42(4)\text{ms}$.

As shown in Eq. 9.47, the velocity dependence on the sum of variances relation drops. Hence, the results obtained with and without velocity should be equivalent.

For the non-velocity case, we measure the zero force signal of a bead at rest (Fig. 9.1b), while in the velocity case, we apply a flow of force $\sim$ 5pN.

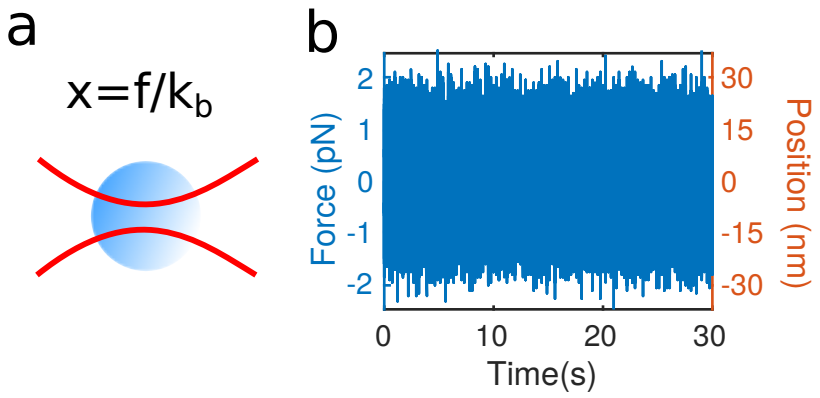

Figure 9.1: Single bead configuration, force and position signals. (**a**) Experimental configuration of a single bead (blue sphere) optically trapped (red lines). In this configuration, the position of the bead respect to the center of the optical trap is directly the measured force divided by the trap stiffness. (**b**) Force and position signals for a single bead optically trapped. The force is show in the left y-axis while the position is shown in the right y-axis.

9.5.1.1 Displacement and cumulative forces variances

In Figure 9.2 we show six different datasets: F_{01}, F_{02}, and F_{03} stand for single beads at rest (circles with different blue tonalities), while F_{11}, F_{12}, and F_{13} stand for single beads in a flow (squares with different tonalities of red).

In Figure 9.2a we show bead's displacement variances as a function of time in log-log scale (upper panel) and normal-normal scale (lower panel). We clearly distinguish the two regimes described in Eq. 9.13. For $t \ll \tau_R$, the displacement variance grows linearly with time while, for $t \gg \tau_R$, the displacement variance reaches a maximum value. In Figure 9.2a (lower panel), we observe that the stationary value at large times is equal to $2k_BT/k_b$ as predicted in Eq. 9.12.

The variance of the sum of forces also presents two separated regimes with a crossover at $t \simeq \tau_R$. In Figure 9.2b (upper panel), we observe a quadratic dependence for the variance of the cumulative force versus time at short times ($t \ll \tau_R$). However, in the large time regime ($t > \tau_R$), we observe a linear dependence (Fig. 9.2b, lower panel).

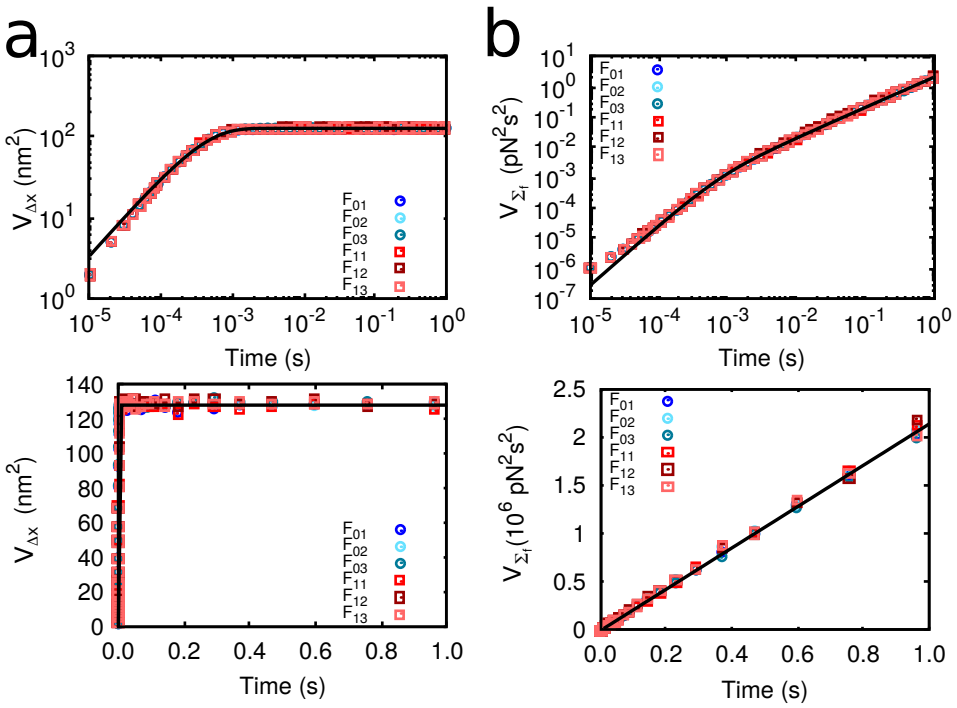

Figure 9.2: Single bead displacement and cumulative force variances. $V_{\Delta x}$ and V_{Σ_f} for single beads optically trapped. Blueish points for beads at rest and reddish squares for beads inside a flow. The blueish circles are barely seen because they overlap with the reddish squares. Black lines represent simultaneous fits to Eqs. 9.13 and 9.19 over the six datasets. Log-log scale representation in upper panels and normal scale representation in lower ones. (**a**) Displacement variance. (**b**) Cumulative force variance.

As the six datasets are compatible for both $V_{\Delta x}$ and V_{Σ_f}, we simultaneously fit (black lines) all the data to the theoretical predictions (Eqs. 9.13 and 9.19). The agreement between experiments and theory is pretty good, and we do not see a dependence with the speed of the flow, as expected.

9.5.1.2 Sum of variances

The sum of the variances is obtained by combining the displacement variance with the variance of the cumulative force as shown in Eq. 9.47. In Figure 9.3, we present the sum of the two variances (green circles) together with the contributions of the displacement variance (blue circles) and the variance of the cumulative force (red circles). Notice that in this figure we plot Eq. 9.22 (rather than Eq. 9.47) where the displacement's variance is expressed as $V_{\Delta x} = V_{\Delta f}/k_b^2$. In this way, by fitting the data to Eq. 9.22 we can derive the values of k_b and γ. We observe a linear dependence between the sum of the variances and time. At short times ($t < \tau_R$), the main contribution to the sum of variances is the displacement variance, while for long times ($t > \tau_R$), the displacement variance reaches a stationary value, and the major contribution is the variance of the cumulative force.

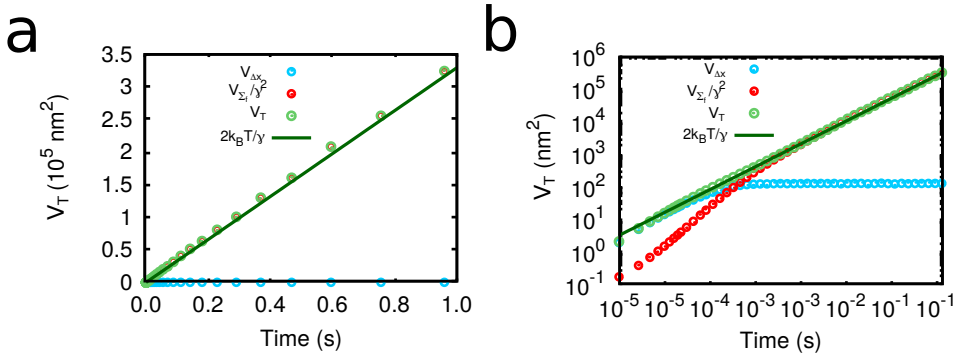

Figure 9.3: Single bead variance sum rule. Sum of the variances for a single bead optically trapped (green circles). In blue circles, the contribution of the displacement variance and, in red circles, the contribution of the variance of the cumulative force. The fit to Eq. 9.47 is represented in dark green. (**a**) Normal scale. (**b**) Log-log scale.

Each fit in Figures 9.2 and 9.3, returns two fitting parameters, k_b and γ (Table 9.1). These values are compatible with the expected ones: $k_b = 60(5)\text{pN}/\mu\text{m}$ and $\gamma = 2.5(3) \cdot 10^{-2}\text{pN} \cdot \text{s}/\mu\text{m}$. k_b was obtained by measuring the power spectrum in calibration beads (Fig. 4.5), and γ from Eq. 9.53 with η the viscosity of distilled water at 298K ($\eta = 0.00089(4)\text{Pa} \cdot \text{s}$) and $r = 1.50(1)\mu\text{m}$.

	k_b(pN/μm)	$\gamma(10^{-2}$pN $\cdot$ s/μm)
$V_{\Delta x}$	58(1)	2.4(1)
V_{Σ_f}	62(4)	2.6(1)
V_T	60(2)	2.7(1)

Table 9.1: Single bead trap stiffness and friction coefficient. Bead stiffness, k_b, and friction coefficient, γ, obtained by fitting the variance of the displacement, the cumulative force variance and the sum of variances. Results have been averaged over 6 beads (3 without a flow, 3 with flow).

9.5.2 Folded and unfolded CD4 hairpin

9.5.2.1 Obtaining bead's displacement and force signals

In this chapter, we apply the variance sum rule analysis to an optically trapped bead attached to a CD4 hairpin in the folded or unfolded state. The CD4 is a small hairpin composed of a stem of 20bp terminating in a tetraloop (GAAA). To manipulate the hairpin, we attach a short dsDNA handle (29bp) to each end of the hairpin to increase the signal noise ratio (SNR) [52]. One handle is tailed with biotins to bind the SA bead, and the other one is tailed with digoxygenins to bind the AD bead. In Figure 9.4a, we show the experimental configuration. The molecular construct is held between two beads, the lower one (SA) is fixed on the tip of the micropipette by air suction and the upper one (AD) is captured by the optical trap.

The CD4 hairpin adds an extra contribution to the bead dynamics compare to the case of a bead alone optically trapped (Chapter 9.5). Therefore, with a tethered hairpin, the total stiffness of the bead is the sum of the contributions of the tethered molecular construct (hairpin plus handles) and the optical trap. The bead is connected on one side to the optical trap and on the other side, the molecular construct in a parallel configuration (Fig. E.1). This can be modeled by two springs, being k_b the trap stiffness, and k_m the stiffness of the molecular construct (hairpin plus handles). As explained in Appendix E, the total stiffness k_T acting on the bead equals $k_T = k_b + k_m$.

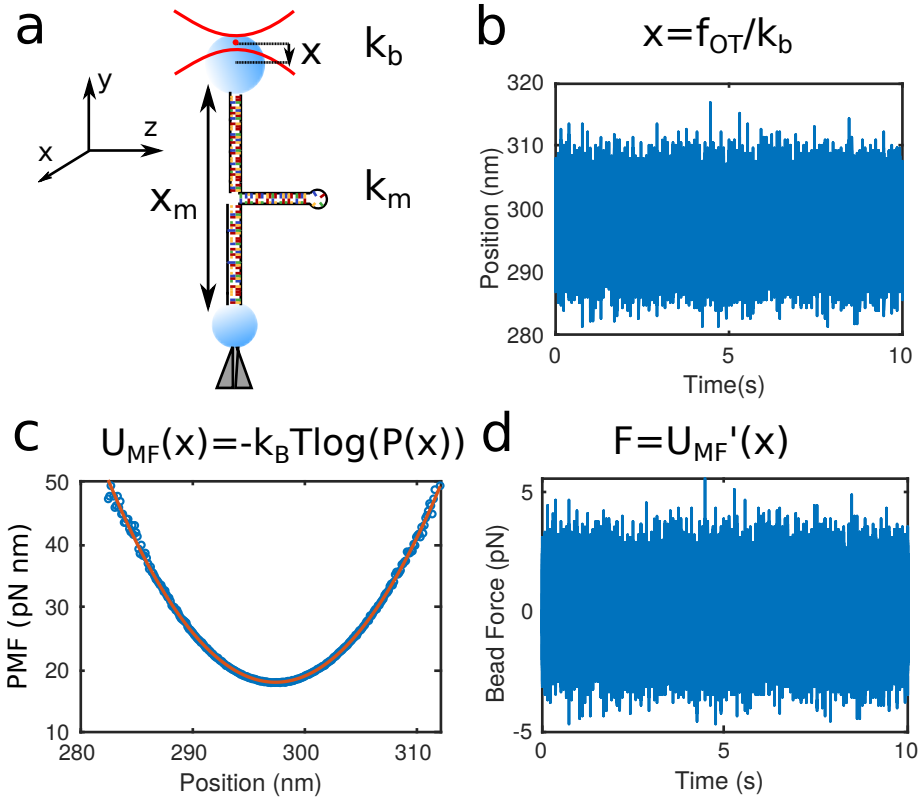

Figure 9.4: CD4 experimental configuration and bead's position and force signals. (**a**) Experimental configuration where the CD4 hairpin is linked to two beads by 29bp dsDNA handles. The bead is captured in the optical trap (red lines) and the other is fixed on the tip of a micropipette. k_b is the trap stiffness, and k_m is the stiffness of the molecular construct (hairpin plus handles). (**b**) Bead's position signal. The relation $x = f_{OT}/k_b$ has been used to convert force into position. (**c**) Potential of the mean force (PMF) of bead's position x (blue circles, $U_{MF}(x)$) and a quadratic fit (orange line). $V_{\Delta x}$ has been calculated from the position distribution $P(x)$ using the expression $U_{MF}(x) = -k_B T \log(P(x))$, Eq. **??** (**d**) Bead's force signal computed by deriving the PMF, $F(x) = U'_{MF}(x)$.

In the simplest description of the motion of the bead, a single friction coefficient describes the dragging force with water. However, in a setup where there is a molecule tethered the bead, a single friction coefficient cannot describe the dynamics in detail. This arises the question of how to evaluate the effect of the molecular construct in the beads's dynamics.

For a linear polymer, the longitudinal friction coefficient $\gamma_{\parallel}$ is given by,

$$\gamma_{\parallel} = \frac{2\pi\eta L}{\log(L/a)} \tag{9.54}$$

where L is the contour length and a the diameter of the cross section. For the short molecules considered in these experiments $L \simeq$ 20nm for the folded hairpin and $L \simeq 50$nm for the unfolded hairpin being $\gamma_{\parallel} \simeq [10^{-5}, 10^{-4}]\text{pN} \cdot \text{s}/\mu\text{m}$ which is negligible with respect to the bead's friction coefficient $\gamma = 2.5 \cdot 10^{-2}\text{pN} \cdot \text{s}/\mu\text{m}$.

However, the hairpin experimental configuration has the trap and micropipette beads in proximity with each other leading to important bead-bead hydrodynamic effects. In fact, the short elongation of the molecular construct x_m ($\sim$20nm in the folded case and $\sim$50 nm in the unfolded one) implies that the beads are extremely close to each other during the experiments. The bead-bead proximity between the AD and the SA beads increases the value of γ (see Chapter 3 Section 3.4). Therefore, for the CD4 experiments, we expect to obtain larger γ values respect to the single bead case ($\gamma = 0.025(3)\text{pNs}/\mu\text{m}$) due to the bead-bead hydrodynamic effects.

To apply the variance rule we still need to calculate the total force acting on the bead (and not only the force exerted by the optical trap), while the position is given by f_{OT}/k_b (Fig. 9.4b), permitting us to calculate $V_{\Delta x}$.

To derive the total force applied to the bead ($F = f_m + f_{OT}$, Fig. 9.4a) we determine the potential of mean force for the bead. The potential of the mean force acting on the bead is defined as,

$$U_{MF}(x) = -k_B T \log P(x) \tag{9.55}$$

where $P(x)$ is the normalized probability of the bead's position. In Figure 9.4c, we show the potential of mean force calculated from the measured position signal at Figure 9.4b together with its quadratic fit. Notice that the stiffness associated with the quadratic potential equals the total stiffness k_T as the variance associated with the bead position has two contributions: the trap stiffness (k_b) and the molecular construct (k_m). Finally, we derive the potential respect to the position ,$F(x) = -U'_{MF}(x)$, and evaluate it for every value of the position signal to obtain the total bead force F signal (Fig. 9.4d). This

procedure is only applicable for equilibrium systems, otherwise there are net currents in the system and Eq. 9.55 does not holds.

9.5.2.2 Displacement (Δx) and cumulative force (Σ_f) variances

The displacement variance shown in Figure 9.5a follows the equilibrium prediction of Eq. 9.13. However, the relaxation time of the bead is now equal to $\tau_R = \gamma/k_T$ where k_T is the total stiffness. Therefore, the stationary value of $V_{\Delta x}$ for long times is equal to $2k_BT/k_T$ instead of $2k_BT/k_b$. The k_T values obtained from the fits are $k_T = 290\text{pN}/\mu\text{m}$ (unfolded) and $k_T = 370\text{pN}/\mu\text{m}$ (folded).

For the variance of the cumulative force, we observe deviations from the equilibrium prediction (Eq. 9.19) above 10ms (Fig. 9.5b, blue and red solid lines). These deviations are caused by drift effects due to small movements of the micropipette in the microfluidics chamber, a macroscopic object subject to drift (temperature cahnges, air currents,enviormental noise). Tiny misalignments of the tether molecule due to micropipette movements introduce drift forces to the force signal as the molecular construct is only 40 nm long. Drift contributes a lot to V_{Σ_f} at long times because, being the variance of the cumulative force, it grows linearly with time.

9.5.2.3 Sum of variances

In Figure 9.6, we show $V_{\Delta f}/k_b^2$ (blue circles), V_{Σ_F}/γ^2 (red circles), and the sum of the two variances V_T (green circles) for the unfolded hairpin (panel a) and the folded (panel b).

For the unfolded case (Fig. 9.6a), the sum of the variances presents a slight deviation respect the equilibrium (dark green line), while the folded case (Fig. 9.6b) presents a much larger deviation. The deviation at long times is related to the drift of the micropipette. Hence, the folded case's more significant deviation could be related to the bead being closer to the micropipette.

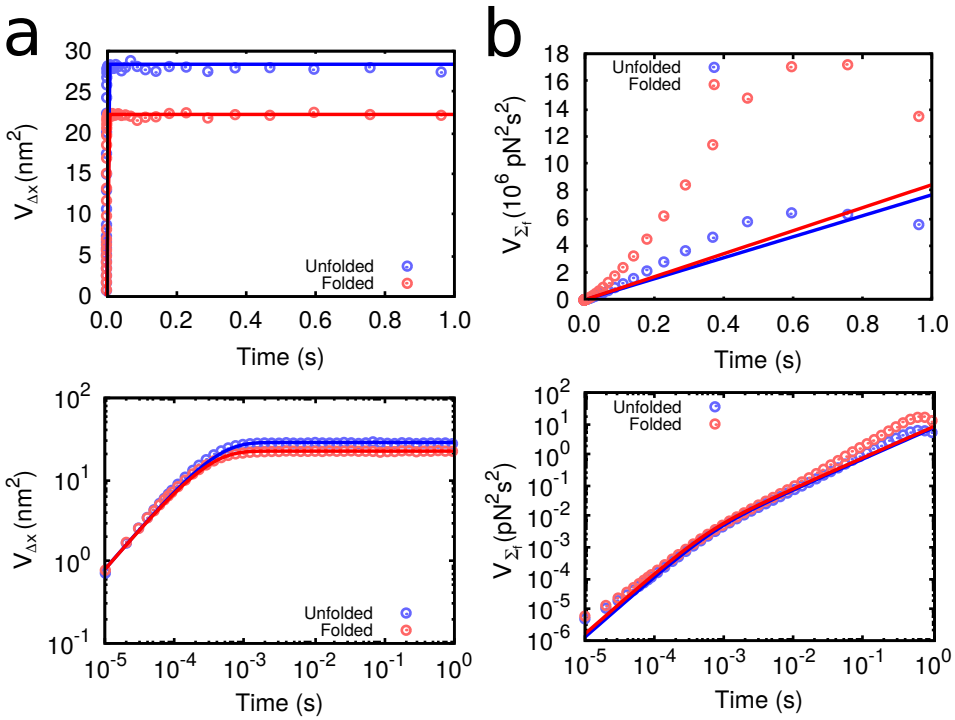

Figure 9.5: Bead's position and cumulative force variances. Variances $(V_{\Delta x}, V_{\Sigma_f})$ for the unfolded hairpin (blue) and folded (red) with their corresponding fits by Eqs. 9.13 and 9.19. Upper panels in normal scale and lower panels in log-log scale. (**a**) Displacement variance $V_{\Delta x}$. k_T is computed from the value of the plateau. (**b**) Cumulative force variance V_{Σ_f}.

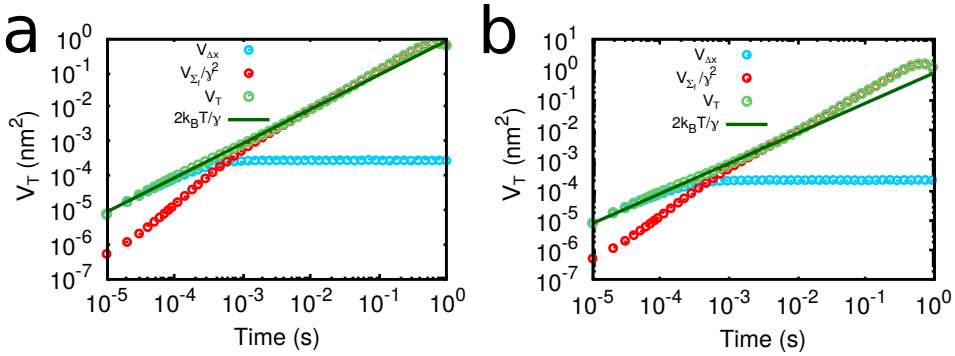

Figure 9.6: Sum of variances with the two contributions $(V_{\Delta x}, V_{\Sigma_f})$ for CD4 experiments. V_T (green circles), $V_{\Delta x}$(blue circles), and V_{Σ_f} (red circles). Dark green line represents the fit to Eq. 9.71 between 10^{-5}s and 10^{-2}s (**a**) Unfolded CD4 hairpin . (**b**) Folded CD4 hairpin .

By fitting Eq. 9.47 to the sum of the two variances for both unfolded and folded cases (between 10^{-5}s and 10^{-2}s where there is no drift effect and we observe a linear dependence with time), we obtain the total stiffness and the friction coefficient of the bead (Table 9.2)

	$k_T(pN/\mu m)$	$\gamma(10^{-2}pNs/\mu m)$
Unfolded	290(10)	9.4(2)
Folded	370(20)	10.3(3)

Table 9.2: Total stiffness and friction coefficient. Total stiffness, $k_T = k_b + k_m$, and friction coefficient, γ, obtained by fitting the sum of the two variances to the equilibrium case (Eq. 9.47).

The total stiffness k_T which is the sum of the trap stiffness and the stiffness of the molecular construct $k_T = k_b + k_m$, presents a significant dependence on the folding state of the hairpin (folded and unfolded). As the trap stiffness k_b takes the same value in both folded and unfolded states, the main difference between the total stiffness in the folded state k_T^F, and the total stiffness in the unfolded state k_T^U, is due to the stiffness of the molecular construct k_m. The molecular construct is formed by the hairpin and two handles in a series configuration. As reported in [53], $k_m^F > k_m^U$ (Table 9.2) due to the low stiffness of ssDNA. The total hairpin stiffness is computed as,

$$\frac{1}{k_m^U} = \frac{1}{k_{handles}} + \frac{1}{k_{ssDNA}} \tag{9.56}$$

for the unfolded state, and,

$$\frac{1}{k_m^F} = \frac{1}{k_{handles}} + \frac{1}{k_d} \tag{9.57}$$

for the folded state. In Eq. 9.57, k_d is the stiffness of the dipole representing the stem of the hairpin that has a diameter of $\sim$ 2nm.

The friction coefficient values shown in Table 9.2 ($\gamma \sim 9 - 11 \cdot 10^{-2}$pN $\cdot$ s/μm) are four times larger than the expected value for a single bead of 3μm of diameter ($\gamma \sim 2.5 \cdot 10^{-2}$pN $\cdot$ s/μm). In Chapter 3 Section 3.4, we report how γ increases as the distance between beads decreases. Table 9.2 shows $\gamma_F > \gamma_U$, which is consistent with AD and SA beads being closer in the folded state enhancing hydrodynamic

effects. Moreover, these values of γ are compatible with the bead-bead proximity model with a misalignment $x_0 = 0.1\mu$m (Chapter 3, section 3.4).

9.6 Entropy production, TUR and reversed-TUR

In steady states systems it has been proven that the entropy production (or its rate) satisfies the inequalities,

$$\frac{\langle s_t \rangle}{2k_B} \geq \frac{\langle J_t \rangle^2}{\sigma^2_{J_t}} \tag{9.58}$$

where J_T is the fluctuation current, or,

$$\sigma^2_{J_t} \geq \frac{2k_B \langle J_t \rangle^2}{\langle s_t \rangle} \tag{9.59}$$

where $\sigma^2_{J_t} = \langle J_t^2 \rangle - \langle J_t \rangle^2$. This is known as the thermodynamic uncertanty relation (TUR) [54, 55]. For time dependent potentials (being the case of a moving trap) this relation does not hold. In fact, the variance sum rule leads to a reverse inequality in Eq. 9.58, where $\langle s_t \rangle / 2k_B \leq \langle J_t \rangle^2 / \sigma^2_{J_t}$ for the case of $J = \Delta x$ and $J = s$. To show this we start for Equation 9.47, which implies the following inequalities,

$$V_{\Delta x} \leq 2Dt, \qquad V_{\Sigma_f} \leq 2\gamma^2 Dt \tag{9.60}$$

In the presence of a flow $V_{\Sigma_f} = V_W / v^2$, leading to,

$$V_W \leq 2\gamma^2 v^2 Dt \tag{9.61}$$

The average entropy production equals the average heat release to the environment due to the friction of the bead with the water,

$$\langle s_t \rangle = \frac{\langle Q_t \rangle}{T} = \frac{\gamma v^2 t}{T} \tag{9.62}$$

where T is the temperature. According to the first law of thermodynamics,

$$W_t - Q_t = \Delta U_t \tag{9.63}$$

giving $\langle \Delta U_t \rangle = 0$ and $V_{\Delta U} \sim O(1)$ or finite, so $V_{\Delta U}/V_W \to 0$ in the limit $t \to \infty$. This implies $\langle Q_t \rangle = \langle W_t \rangle$, and $\langle s_t \rangle = \langle W_t \rangle / T$ and,

$$V_s = \frac{V_W}{T^2} \tag{9.64}$$

Then we rewrite Eq. 9.61 as,

$$T^2 V_s \leq \frac{2T^2 \langle s \rangle^2 D}{tv^2} \tag{9.65}$$

where $D = k_B T/\gamma$,

$$\frac{\langle s_t \rangle}{2k_B} = \frac{\gamma v^2 t}{2k_B T} \leq \frac{\langle s_t \rangle^2}{V_s} \tag{9.66}$$

As $\langle s_t \rangle = \gamma v^2 t/T$ and $\langle W \rangle^2 / V_W = \langle s_t \rangle^2 / V_s$,

$$\frac{\langle s_t \rangle}{2k_B} \leq \frac{\langle W \rangle^2}{V_W} \tag{9.67}$$

leading to an upper bound for the entropy production.

9.6.1 The stochastic switching trap (SST) model

In this section, we consider a simple model of NESS. In particular, we consider a model of a stochastic switching trap introduced in [51] as a simple realization of an actively driven system. In the SST model, the optical trap randomly switches between two positions separated by $\Delta\lambda$. Therefore, the trap position λ separated by $\Delta\lambda$ follows a dichotomous behavior, flipping between two states ($\sigma = 0, 1$) with exponentially distributed lifetimes. The lifetime of state $\sigma = 0$ equals $\tau_0 = \tau_e/2m$, whereas that of $\sigma = 1$ equals $\tau_1 = \tau_e/2(1-m)$. For m =1/2 both levels of λ are equally probable and the lifetimes of both states are identical $\tau_\sigma = \tau_e$. Let m the probability of state $\sigma = 1$ and $1 - m$ that of $\sigma = 0$ for the dichotomous signal. Switching rates $K_{\sigma \to 1-\sigma}$ are then equal to $1/\tau_\sigma = \frac{2}{\tau_e}[m + \sigma(1-2m)]$. The total relaxation rate of SST being equal to $K_T = K_{0\to1} + K_{1\to0} = 2/\tau_e$. m is a useful parameter in the stochastic switching protocol. Notice that $m =< \sigma >= K_{0\to1}/K_T$.

The SST model can be exactly solved for a linear optical trap. Analytical expressions for $V_\lambda = \sigma^2_{\Delta\lambda}$, $V_{\Delta x}$ and V_W can be obtained,

$$V_\lambda = \frac{\Delta\lambda^2}{2}(1 - e^{-2t/\tau_e}) \tag{9.68}$$

$$V_{\Delta x}(t) = \frac{2k_BT}{k_b}(1-e^{-t/\tau_R})+\overbrace{\frac{\epsilon^2 m(1-m)}{k_b^2(1-\theta^2)}[\theta(1-e^{-t/\tau_R})-\theta^2(1-e^{-tK_T})]}^{E} \tag{9.69}$$

where $\epsilon = k_b\Delta\lambda$, $\theta = (K_T\tau_R)^{-1}$, with τ_R the bead relaxation time given in Eq. 9.14.

The variance of the cumulative force is expressed as,

$$\begin{aligned} V_{\Sigma_f}(t) &= 2k_BT\gamma t(1 - \frac{\tau_R}{\Delta t}(1 - e^{-t/\tau_R})) \\ &+ \underbrace{\frac{\epsilon^2 m(1-m)\tau_R^2}{(1-\theta^2)}[\theta(1-e^{-t/\tau_R})-\theta^2(1-e^{-tK_T})]}_{E} \end{aligned} \tag{9.70}$$

Combining Eq. 9.69 and 9.70, we obtain the expression for the variance sum rule,

$$V_T = \frac{2k_BTt}{\gamma} + \overbrace{\frac{\epsilon^2 m(1-m)}{k_b^2(1-\theta^2)}[\theta(1-e^{-t/\tau_R})-\theta^2(1-e^{-tK_T})]}^{E} \tag{9.71}$$

This protocol results in an extra term E respect the equilibrium expressions for position, cumulative force and sum of variances (Eqs. 9.13, 9.19 and 9.47).

Note that the additional term E on the rhs of Eq. 9.71 vanishes for $\epsilon = 0(\Delta\lambda = 0)$ and $m = 0, 1$. In these cases, there is no switching and we recover the previous result of the bead in a stationary trap.

In the SST model, the average entropy production can be analytically solved,

$$\frac{dS}{dt} = \frac{k_T(1-m)m\epsilon^2}{\gamma(k_T + k_b/\gamma)} \tag{9.72}$$

where $m =< \sigma >= K_{0\to1}/K_T$.

9.6.2 Experimental results

9.6.2.1 SST protocol

In this chapter, we study the variance relations of an optically trapped calibration bead in a NESS. Once the bead is optically trapped, the optical trap is moved stochastically between two positions with an amplitude $\Delta\lambda$. The lifetime at each trap position has been chosen to be equal to τ_e corresponding to $m = 1/2$ in the SST protocol. In the SST protocol, the trap stiffness $k_b = 60(5)\text{pN}/\mu\text{m}$, the bead friction coefficient $\gamma = 2.5(3)10^{-2}\text{pNs}/\mu\text{m}$ and the bead relaxation time $\tau_r = \gamma/k_b = 4.2(4)10^{-4}\text{s}$ are fixed parameters.

We design three different protocols by changing the values of $\Delta\lambda$ and τ_e, as shown in Table 9.3.

	$\Delta\lambda(\mu m)$	$\tau_e(s)$
$P1$	0.20	0.33
$P2$	0.27	0.20
$P3$	0.41	0.20

Table 9.3: SST protocols parameters. Trap amplitude $\Delta\lambda$, and lifetime τ_e, for three different SST protocols P1, P2 and P3.

In our optical tweezers setup we do not directly measure the bead position but rather we measure the force. In the SST protocol, bead's position must be measured relative to the frame set by the medium at rest to calculate the position variance, $\sigma^2_{\Delta x}$. As the trap switches between two positions while dragging the bead, its position relative to the medium is given by $x = \lambda + x_b$ where λ is the trap position and x_b the position of the bead relative to the center of the trap. In order to obtain bead's position x, we combine the force signal $f(t)$ (Fig. 9.7a), and the trap position $\lambda(t)$ (Fig. 9.7b) as,

$$x = \lambda + f/k_b \tag{9.73}$$

where the bead position respect to the center of the optical trap $x_b = f/k_b$ is shown in Figure 9.7c, and the bead position x is shown in Figure 9.7d.

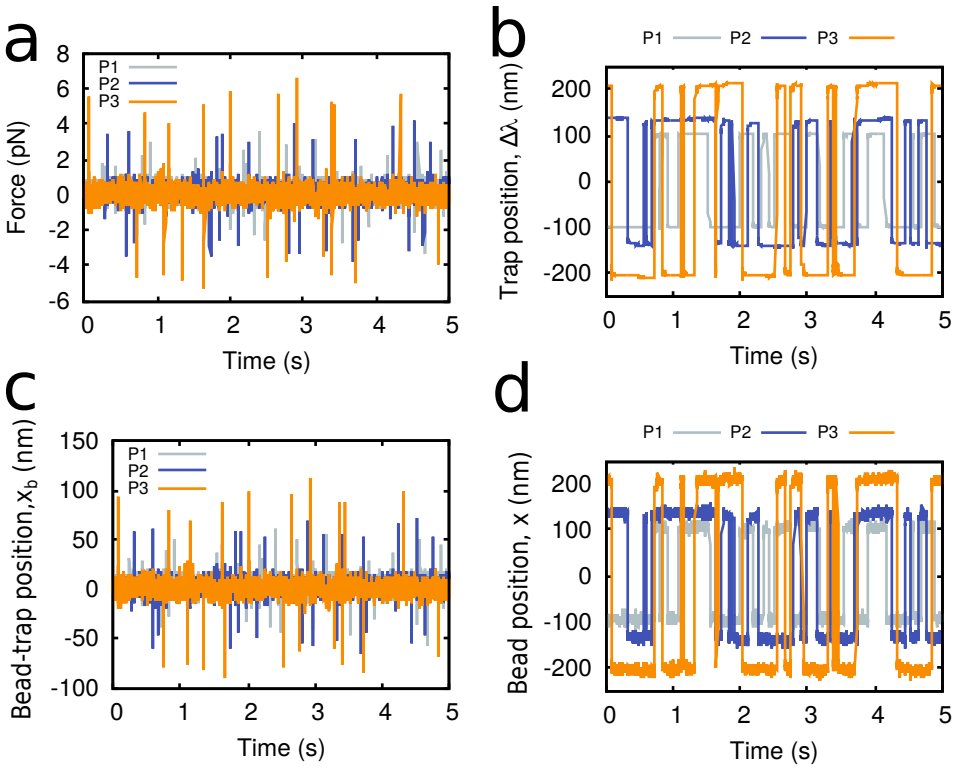

Figure 9.7: Force, trap position, bead-trap position and bead position signals for SST protocols. Each SST protocol is represented in a different color. The protocols' parameters are detailed in Table 9.3. (**a**) Force signals. (**b**) Trap position signals, also referred as position of the center of the trap. (**c**) Bead position respect to the center of the optical trap signals. (**d**) Bead position signals relative to the medium at rest.

9.6.2.2 Variances

First, we have tested the validity of the implemented SST protocol. In Figure 9.8a, we show the variance of the trap position for protocols P1, P2, and P3 together with their corresponding fits to Eq. 9.68. The variance of the trap position increases with $\Delta\lambda$ as expected from (Eq. 9.68). However, there are deviations between the expected behaviour (Eq. 9.68) and the experimental data at short times (between 10^{-5} and 10^{-4}) but also around 1ms where the $\sigma^2_{\Delta\lambda}$ exhibits a gentle plateau. The plateau arises due to the limitations of the piezo that controls the optical trap position. For trap position jumps $\Delta\lambda > 0.1\mu$m, the piezo

does this change in a finite number of steps (between two and three in our case) until reaching the $\Delta\lambda$ value. These shorter discrete steps are not considered in the SST model leading to the discrepancy between theory and experiments at short times.

As we will see below, and despite limitations of the protocol, the experimental results for the variances fit well to the SST model. From Eqs. 9.69, 9.70, and 9.71, the $V_{\Delta x}$, V_{Σ_f}, V_T have two terms, the equilibrium term and the extra one defined by E on the rhs of Eqs. 9.69, 9.70, and 9.71. The equilibrium term depends on the relaxation time of the bead in equilibrium, $\tau_R = 4.2(4)10^{-4}s$, whereas the extra term E depends on τ_R and the time τ_e.

The variance of the bead displacement, $V_{\Delta x}$, is in good agreement with the theoretical prediction in Eq. 9.69 (Fig. 9.8b). For short times ($t < \tau_R$ $t = 10 - 100\mu$s), the $V_{\Delta x}$ values overlap for the three protocols overlap being equal to equilibrium term in the rhs of Eq. 9.69. This term is given by $2k_BT(1-e^{-tk_b/\gamma})/k_b$ and takes the same value for any protocol as only depends on k_b and γ. For $t > \tau_R$, $V_{\Delta x}$ varies with the protocol due to the contribution of the extra term E, which depends on the control parameters $\Delta\lambda$, τ_e and m. For $t > \tau_e$, $V_{\Delta x}$ reaches a stationary value equal to $2k_BT/k_b + \epsilon^2 m(1-m)\theta/(k_b^2(1+\theta))$.

The variance of the cumulative force, V_{Σ_f} (Fig. 9.8c), also fits the theoretical prediction (Eq. 9.70). Notice that V_{Σ_f} shows a slight difference between protocols at intermediate times, however this tends to disappear at long times. From Equation 9.70, in the long time limit the correction term E is finite (whereas the equilibrium one grows linearly with time) making the relative difference between the two negligible in a vertical log scale.

Concerning the variance sum rule (Fig. 9.8d), we observe a deviation from equilibrium (black dash line) at intermediate times ($\tau_R < t < \tau_e$, shaded region). This difference is directly related to the system's entropy production (Eq. 9.72). In particular, we observe how the entropy production (reported in Table 9.4 and computed from Eq. 9.72) progressively increases for the different protocols $P1 < P2 < P3$, which is consistent with the increased deviation.

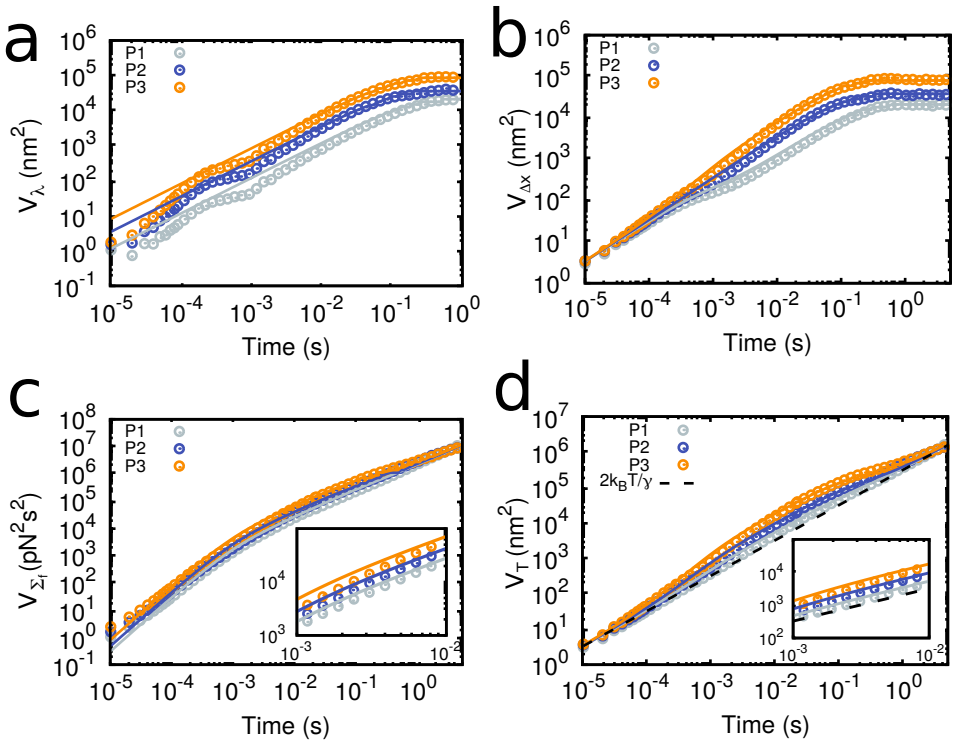

Figure 9.8: Time-dependent of variances for the SST protocol. Variances of P1, P2 and P3 protocols with their corresponding fits in log-log scale. Each protocol is represented with circles of different color. (**a**) Variance of the trap position. (**b**) Variance of the bead position. (**c**) Variance of the cumulative force. (**d**) Variance sum rule. Dash black line represents the equilibrium case.

	$P1$	$P2$	$P3$
$\sigma = \dot{s}(k_B T/s)$	880	2650	6110

Table 9.4: Entropy production of SST protocols. Entropy production computed from Eq. 9.72 for SST protocol P1, P2 and P3.

In Figure 9.9, we show the variance sum rule for protocols P1, P2, and P3 separately. Each plot contains contribution $V_{\Delta f}/k_b^2$ Eq. 9.69 (blue circles), the V_{Σ_f}/γ^2 Eq. 9.70 (red circles) and $V_{\Delta f}/k_b^2 + V_{\Sigma_f}/\gamma^2$ Eq. 9.71 (green circles). This kind of representation allows us to

identify the contributions of $V_{\Delta x}$ and V_{Σ_f} over five time decades. We observe three different regimes in the sum of the variances defined by the two characteristic times τ_R and τ_e. For short times ($t < \tau_R$), $V_{\Delta x}$ is the main contribution, for intermediate times ($\tau_R < t < \tau_e$), both $V_{\Delta x}$ and V_{Σ_f} contribute, while, for long times ($t > \tau_e$), the main contribution is V_{Σ_f} as $V_{\Delta x}$ saturates to a finite value.

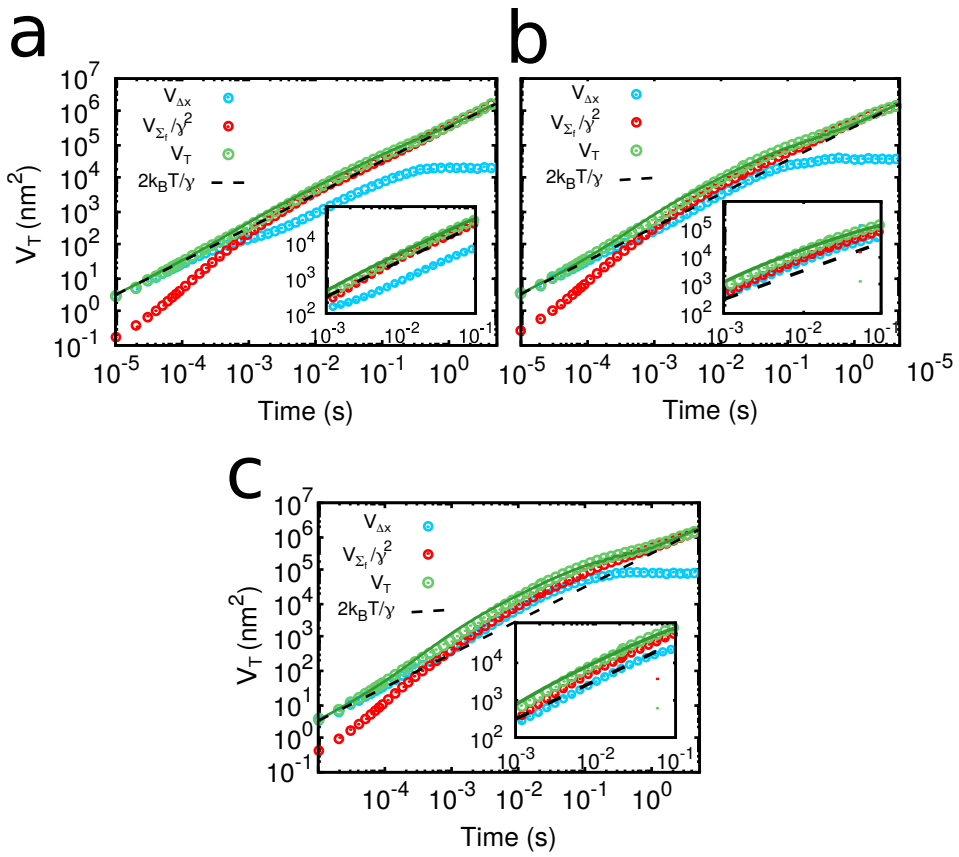

Figure 9.9: Sum of variances with the two contributions ($V_{\Delta x}$ and V_{Σ_f}) for SST protocols in log-log scale. $V_{\Delta f}/k_b^2$ (blue circles), V_{Σ_f}/γ^2 (red circles), and the sum of the two variances V_T (green circles). The fit to Eq. 9.71 is represented in dark green and dash black lines represent the equilibrium case. Intermediate regions have been zoomed for clarity. (**a**) P1 protocol. (**b**) P2 protocol. (**c**) P3 protocol.

9.7 Discussion and conclusions

In Part IV of this thesis, we have experimentally demonstrated the validity of the variance sum rule for three different systems. The first and simplest system is a single bead captured in an optical trap. The single bead fulfills the theoretical prediction at rest and in the presence of a flow. Moreover, the fitting parameters k_b and γ obtained from the variance of the displacement, the variance of the cumulative force, and the sum of variances are compatible between them and with the bead stiffness and friction coefficient computed from the power spectra analysis. In addition, the obtained values for γ coincide with the expected friction coefficient for a 3μm diameter bead in Milli-Q water at 298K.

The second system is a single bead in the optical trap, attached to a molecular construct formed by a CD4 hairpin and two dsDNA handles. In this case, the optical tweezers do not directly measure the bead's position and force signals. We study two different cases: the first one where the CD4 hairpin is folded (forces around 10 pN), and the second one, where the hairpin is unfolded (forces around 20 pN). In both cases, we recover equilibrium with a total stiffness being the sum of the trap stiffness and the stiffness of the molecular construct. Moreover, the friction coefficient is larger than for the single bead case due to the bead-bead hydrodynamic effect. Although we have observed some deviations from equilibrium at large times, we have attributed this effect to the micropipette drift, and, hence, we have also validated the sum rule of the hairpin in equilibrium in both unfolded and folded states.

The third system is a single bead in an optical trap in a non-equilibrium steady state (NESS). We achieve the NESS by applying a stochastic switching protocol (SST) that randomly moves the trap between two positions separated by an amplitude $\Delta\lambda$. We chose τ_e as the lifetime at each trap position. By changing the two parameters, $\Delta\lambda$ and τ_e, we design three different protocols. For each protocol, we quantify the system's deviation from the equilibrium case (single bead captured in an optical trap) by computing the system's entropy production.

Therefore, the variance sum rule is a new method to characterize a system's state through passive measurements. Unlike the fluctuation-

dissipation theorem, there is no need to measure the response function of a system in order to validate it. It is only required a force signal of the system of interest. Moreover, in the stochastic jump protocol, we have been able to quantify the deviation from the equilibrium behavior by measuring the system's entropy production. This approach opens a groundbreaking methodology to compute exactly the entropy production values of living systems.

9.8 Future Perspectives

As exposed in discussion and conclusions, the breakthrough feature of the variance sum rule is the possibility to compute exactly the entropy production value of the system only through a force signal. Hence, out of equilibrium systems such as cells, molecular motors, bacteria, etc. are excellent candidates to verify the variance sum rule. For that reason, we plan to apply this methodology to active red blood cells (RBC).

The RBCs have several advantages that make them excellent candidates to measure the entropy production from the variance sum rule. In the first place, RBCs are easy to obtain from a fingerprint of a healthy donor. Another advantage is that we can trap them directly with the optical trap as a single bead or measure them by attaching a force probe (bead) as in the CD4 hairpin case.

In Figure 9.10, we present preliminary results of the variance sum rule and the FPS analysis of a RBC directly captured in the optical trap. We observe that the RBC fulfills the variance sum rule with and without an applied flow. For each sum rule (Figure 9.10, a and b), fitting parameters k_{RBC} and γ are obtained and compared with the FPS results of RBC at rest (Table 9.5).

Although we do not observe any deviation from the sum rule, the fitting parameters k_{RBC} and γ remarkably increase with flow. The increase in γ agrees with the expected orientation of a discocyte RBC in the presence of a flow. The prolate orientation of the discocyte along the flow axis (where the major axis of an ellipsoid shape particle orients along the flow) introduces a correction factor on the friction coefficient of a sphere (the so-called Permin friction coefficient) which is larger than 1. In such case (Table 9.5) there is a factor of 1.6 between the

measured γ implying an axial ratio $p \sim (\gamma_{flow}/\gamma_{rest})^{3/2} \sim 2$. $p = a/b$ (a,b being the major and minus axis of the ellipsoid) then $a \simeq 2b$ while in RBC $p = 4$. Future work requires performing more experiments and analysis.

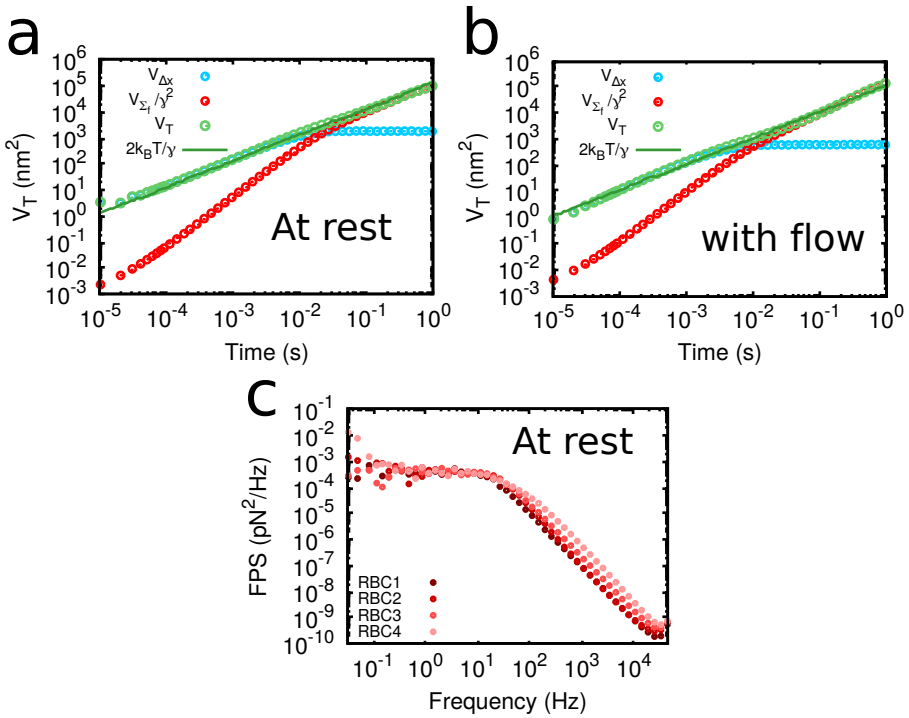

Figure 9.10: RBC Sum of variances. The RBC is captured by the optical trap directly, in contrast with experiments shown in Part III. (**a**) Sum of variances for a RBC at rest. (**b**) Sum of variances for a RBC in a flow ($f \sim 5pN$). (**c**) FPS of RBC at rest.

	V_T at rest	V_T with flow	FPS
k_{RBC}(pN/μm)	9.5(3)	14.0(4)	9.6(3)
$\gamma(10^{-2}$pN $\cdot$ s/μm)	6.3(3)	7.5(4)	6.0(3)

Table 9.5: k_{RBC} and γ of RBC from variance sum rule and FPS. Fitting parameters k_{RBC} and γ obtained from the variance sum rule of a RBC with and without an applied flow together with the extracted k_{RBC} and γ from FPS analysis.

Part V

Noise measurements of dsDNA molecules

Chapter 10

High-frequency force spectroscopy of dsDNA

10.1 Introduction

As discussed in Chapter 1, nucleic acids are the building blocks of life. In particular, DNA is the genetic material that encodes the instructions that determine our development and daily functions (genetic code). The human genetic code is located inside the nucleus of each cell of our body and is composed of approximately 6.4 billion base pairs. The double helix of DNA has a distance between base pairs of 0.34nm, measuring that the linear elongation of our genetic material is $6.4 \cdot 10^9 \text{bp} \cdot 0.34 \text{nm/bp} \sim 2\text{m}$. Keeping that in mind, the genetic code needs to be highly compacted to suit the tiny size of a cell nucleus. The chromosome is the structure where the DNA gets condensed by combining a DNA with packaging proteins called histones.

However, DNA has to be unpacked in order to interact with other molecules. In particular, DNA unwinding is critical for the replication and transcription processes. Moreover, several biological processes involve the stretching of DNA, and as has been already reported, the mechanical forces applied to nucleic acids play a significant role in their binding processes [56]. For that reason, studying the elastic properties of nucleic acids is key to understand how life works at the molecular and cellular levels.

As detailed in Chapter 2, the study of the elastic properties of polymers has provided several mathematical models such as the freely-

jointed chain (FJC), the extensible freely-jointed chain (exFJC) (applied for ssDNA), the worm-like chain (WLC), the extensible worm-like chain (exWLC), and the twistable worm-like chain (tWLC).

In the next chapter, we will study the molecular stiffness of dsDNA molecules. Four different molecular lengths will be studied (from 1kbp to 24kbp). The results show important dependences of the elastic parameters with the contour length that can be interpreted using single-molecule noise measurements using Laser Optical Tweezers (LOT).

10.2 Experimental results

In this chapter, we present the noise measurements of double stranded DNA (dsDNA) single molecules using Laser Optical Tweezers (LOT). In our experimental configuration a single molecule is attached to two micron-sized beads. Both beads are coated, one with streptavidin (SA bead), and the other with antidigoxigenin (AD bead) (coating of the beads is explained in detail in Appendix B). Streptavidin and antidigoxigenin are the specific binding proteins for biotin and digoxigenin respectively. The 3' ends of each DNA strand of the dsDNA are tailed with biotins and digoxigenins. The SA (lower) bead is fixed by air suction on the tip of a micropipette while the AD (upper) bead is optically trapped (Fig. 10.1a left inset).

The force-extension curve (FEC) of dsDNA molecules (Fig. 10.1a grey curve) consists of three different regimes. The first one, from 0pN to 65 pN, where force increases with extension that is modeled by an extensible worm-like chain model (exWLC) expressed as,

$$f = \frac{k_B T}{p}\left[\frac{1}{4}(1 - \frac{x}{L} + \frac{Y}{f})^{-2} - \frac{1}{4} + \frac{x}{L} - \frac{Y}{f}\right] \tag{10.1}$$

where f is the force and x the extension. k_B is the Boltzmann constant, T is the temperature, L is the contour length equal to $N_{bp} \cdot$ 0.34nm/bp in dsDNA, p is the persistence length whereas the Young modulus Y takes a value between 1000-1500pN [6, 57, 58].

The second one, around 65 pN, is the overstretching transition between B-DNA and S-DNA (S for stretched), where the FEC becomes almost flat. The observation of the overstretching plateau confirms that only a single molecule is being stretched. After the overstretching

($\sim$ 70pN), the elastic response of S-DNA, the third regime, takes place and the force increases again with extension.

10.2.1 Power-spectra analysis

The data acquisition consists on recording the noise signal for different force values (schematically represented with green points in Fig. 10.1a) along the three different regimes of the FEC. We measure a force signal of a few seconds at a sample frequency of 50kHz. Then, from the force signal (Fig.10.1b inset), the raw power spectrum (blue) is computed together with the boxcar average (red circles), as shown in Fig.10.1b. To perform the fits, we take the boxcar average of each signal instead of the raw power spectrum. For a single bead inside a quadratic potential, the power spectrum of the force presents a Lorentzian shape characterized by an amplitude(A), and a corner frequency (ν_c) as,

$$S_{ff}(\nu) = \frac{A}{(\nu^2 + \nu_c^2)} \tag{10.2}$$

In the particular case of an optical trap, the amplitude is expressed as,

$$A = \frac{k_B T k_b^2}{2\pi^2 \gamma} \tag{10.3}$$

where k_b is the trap stiffness and γ is the friction coefficient. On the other hand, the corner frequency,

$$\nu_c = \frac{k_T}{(2\pi\gamma)} \tag{10.4}$$

where k_T is the stiffness of the total potential that acts on the bead. Notice that, as our measurements correspond to fluctuations around equilibrium, the total stiffness acting on the bead will be the sum of the trap and the molecular stiffness, $k_T = k_b + k_m$ (See Appendix E). The value for the molecular stiffness $k_m = (dx/df)^{-1}$ is computed by the inverse implicit derivation of extension respect to force of Eq.10.1. Considering Eq. 10.3 and Eq. 10.4, the force power spectrum will be expressed as follows,

$$S_{ff}(\nu) = \frac{k_B T k_b^2}{2\pi^2 \gamma} \frac{1}{\nu^2 + \nu_c^2} \tag{10.5}$$

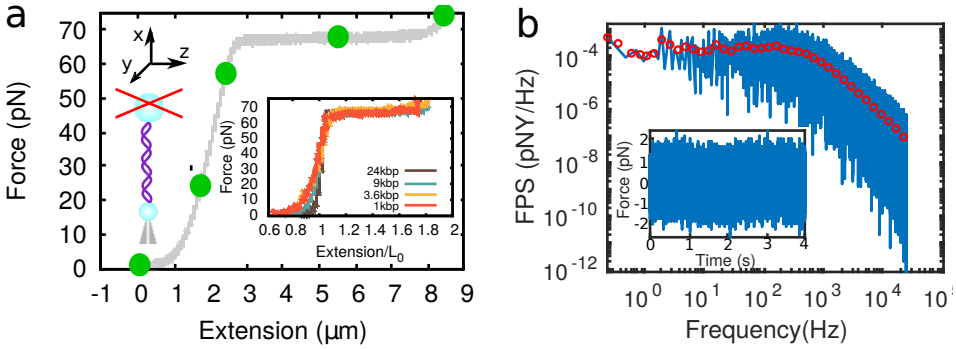

Figure 10.1: Experimental realization and force power spectrum (FPS). (**a**) Force extension curve (FEC) of a 24kbp molecule. In green points, the static positions where the measurements are performed. Inset left: experimental configuration where a dsDNA molecule is held between two beads. The lower bead is fixed on the tip of the micropipette and the upper one is optically trapped. Inset right: FEC measured for the four different molecular lengths. (**b**) Power spectrum of the 24kbp DNA molecule at zero force (blue) and the corresponding boxcar average (red points). Inset: Force signal at 0pN from which the power spectrum has been computed.

We have measured noise signals for four dsDNA molecules of different molecular lengths (24kbp, 9kbp, 3.6kbp and 1kbp - synthesis details described in Appendix F-). We could identify three different processes of different time scales: fast process at high frequencies (above 200Hz), an intermediate process around 100Hz, and a slow process at low frequencies (below 10Hz) (Fig. 10.2(a)). The shape of the power spectrum presents a strong dependence with the applied force (Fig. 10.2b) and the molecular length (Fig. 10.2c). Power spectra were fitted to the sum of three Lorentzians,

$$S_{ff}(\nu) = \frac{A_s}{(\nu^2 + \nu_{cs}^2)} + \frac{A_i}{(\nu^2 + \nu_{ci}^2)} + \frac{A_f}{(\nu^2 + \nu_{cf}^2)} \tag{10.6}$$

We observe that the slow process is compatible with pink noise which has been widely reported as experimental noise and presents a

$1/\nu$ behaviour at low ν in the power spectrum (Fig. 10.3a,b) [59].

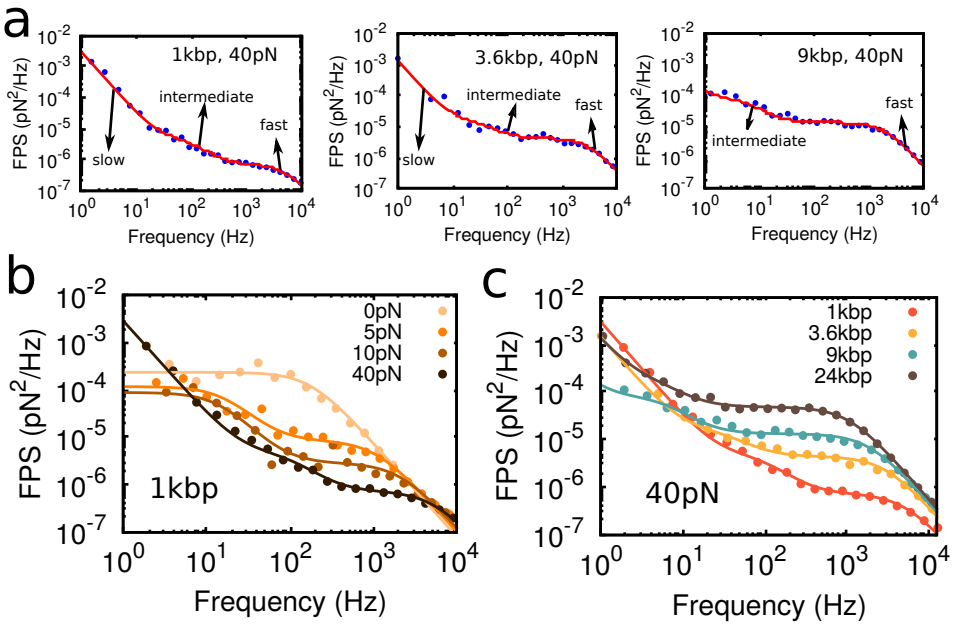

Figure 10.2: Dependences on force and molecular length. (**a**) Boxcar average of force signals for the 1kbp, 3.6kbp and 9kbp molecules around $\simeq$ 40pN where three different processes (fast, intermediate and slow) are observed. Red line represents the fit of the sum of three Lorentzians. (**b**) Power spectra of the 1kbp DNA at four different forces (0pN, 5pN, 10pN and 40pN). (**c**) Power spectra of four different molecular lengths (24kbp, 9kbp, 3.6kbp and kbp) taken at 40 pN force.

Regarding the intermediate process, we verify that is related to the axial fluctuations of the trapped bead in the z-axis where light propagates (Fig. 10.3c,d) as explained in detailed in [60]. This relation process is consequence of the misaligment of the tether out of the optical plane, and gives rose to a basculation of the bead in the optical axis (see below for more details). Therefore, the intermediate process has no contribution to the elastic properties of the molecular constructs.

Consequently, the only process that is related with the elastic response of the molecules is the fast one. The FPS of the fast process follows a Lorentzian shape characterized by an amplitude, A, and a corner frequency , ν_c, as indicated in Eq. 10.5. For all the molecular

lengths, the amplitude increases with force. Furthermore, the amplitude is proportional to the molecular length, being the longer molecule (24kbp) the one with the higher amplitude values (Fig. 10.4a).

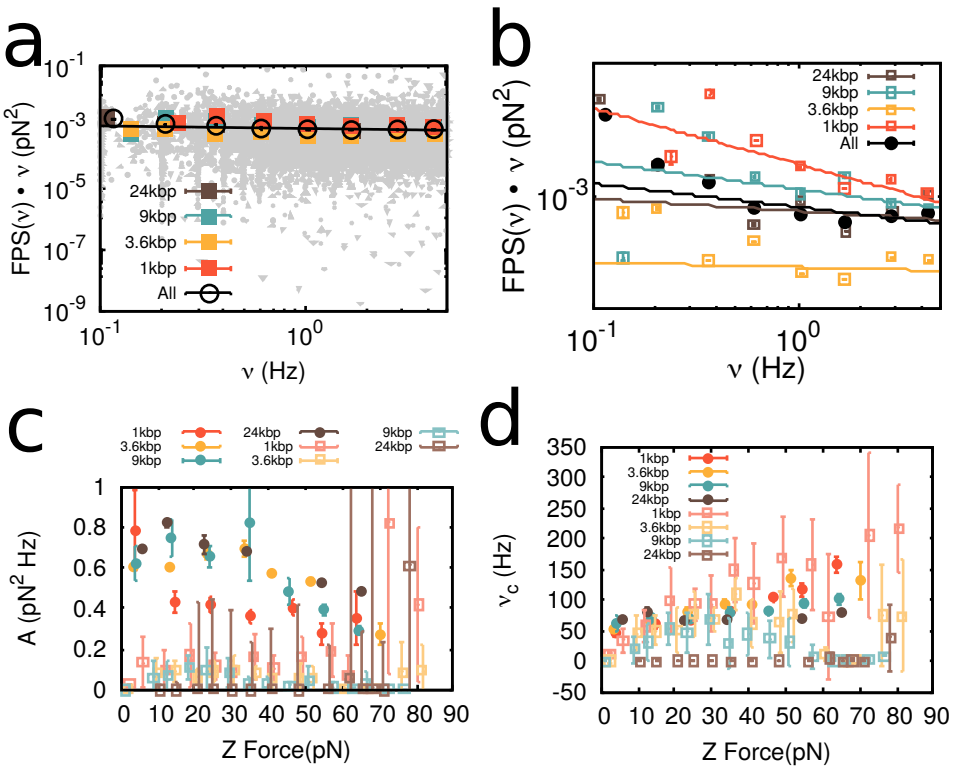

Figure 10.3: Slow and intermediate processes. (**a**) Force power spectra (FPS) multiplied by ν in the low frequency regime for all the molecules and forces (grey). In colored squares, the average of the four different molecules and, in black circles, the average over all the molecules. (**b**) (a) zoom of the averages with their corresponding fits.(**c**) Amplitude of the intermediate process in the x-axis for the four different molecules (empty squares) compared with the amplitudes obtained from the fluctuations in the optical z-axis (circles). (**d**) Corner frequency of the intermediate process in the x-axis for the four different molecules (empty squares) compared with the amplitudes obtained from the fluctuations n the z-axis (circles).

The amplitude of a single bead captured by the optical trap is expressed as Eq. 10.3, where the friction coefficient increases with the AD-SA beads proximity due to hydrodynamic effects (Fig. 10.5a,b).

The trap stiffness, k_b, increases with force due to non-linear effects (Fig. 10.5c). Considering these dependencies, the amplitude expression of Eq. 10.3 (Fig. 10.4a, solid lines) reproduces the experimental data shown in Figure 10.4a (circles).

On the other hand, as shown in Figure 10.2b and c, ν_c shows a strong dependence on both force and molecular length. For all the molecules, ν_c increases with force until it reaches a maximum value around 40pN after which it quickly decreases down to a minimum value in the overstretching regime ($\sim$ 65pN). Regarding the dependence with molecular length, ν_c shows a behaviour opposite to A, decreasing with the molecular length (Fig. 10.2b and Fig. 10.4b).

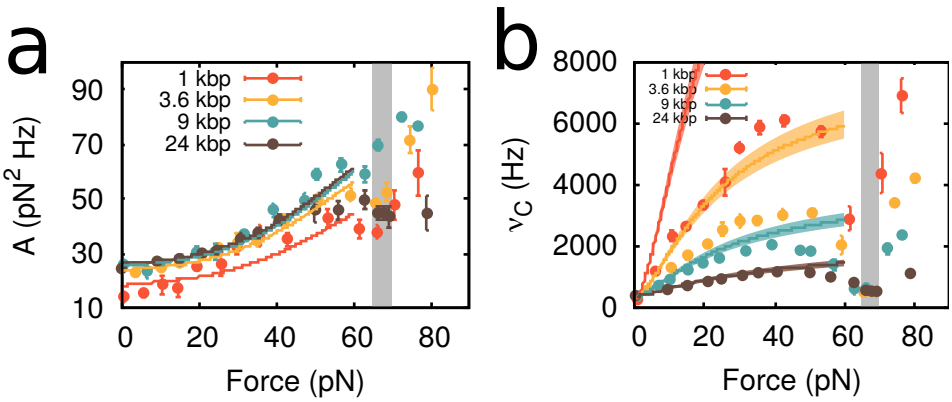

Figure 10.4: Amplitude (A) and corner frequency (ν_c) force dependence. Fits presented in this figure assume a bead-bead distance dependence for the friction coefficient of the optically trapped bead (Fig.10.5 a,b) and a force dependence for trap stiffness (Fig.10.5 c). (**a**) Amplitude versus force for the four molecular lengths with their corresponding fits. (**b**) Corner frequency versus force for the four molecular lengths with their corresponding fits.

Taking into account Eq. 10.4, the experimental values of trap stiffness and friction coefficient allow us to reproduce the experimental data for longer molecules (24kbp and 9kbp). However, the discrepancy between the experimental data and the values predicted by Eq. 10.4 increases as the molecular length decreases (Fig. 10.4b). This indicates there is a length dependence in the parameters of the WLC (Eq. 10.1) used to derive the values of the molecular stiffness k_m. This dependence is also confirmed by the fact that the rescaled FECs

of molecules of different length do not overlap suggesting that the elastic response of the dsDNA do not fully captured by an ideal elastic model (Fig. 10.1a right inset).

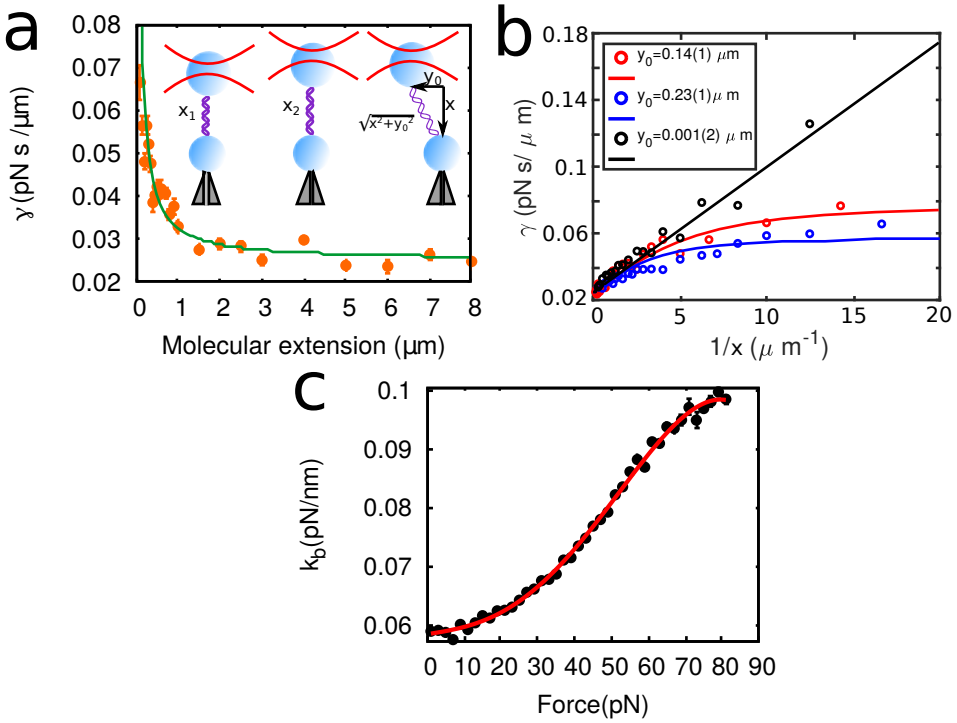

Figure 10.5: Friction coefficient and trap stiffness. (**a**) Friction coefficient as a function of bead-to-bead distance (orange points) with its corresponding fit to $\gamma_0 + A/x$ (green line). Inset: schematics of the measurements at different distances (left and center) and in the presence of misaligning (right). The results $\gamma(x)$ are assumed to be equal with and without molecule between the beads. This is why, we refer to the x-axis as molecular extension. (**b**) Friction coefficient as a function of the inverse of bead-to-bead distance for three different x_0 values with their corresponding fits to $\gamma_0 + A/\sqrt{(y_0^2 + x^2)}$ (For more details and fitting parameters see Chapter 3 section 3.4) (**c**) Trap stiffness versus force computed by deriving the force-distance curve (FDC) obtained by moving the trap over an immobilized bead on the tip of the micropipette (black points) and its corresponding fit to a non-linear quartic potential (red line).

10.2.2 Young modulus' molecular length dependence

Assuming the exWLC model as a valid approach to describe the elastic response of dsDNA, at least until 30pN, the only parameters that could depend on the molecular length are the persistence length p, and the Young modulus, Y. The dependence of the persistance length on the molecular length [61] has already been considered in the analysis presented above. This dependence is expressed as,

$$p(L) = \frac{p_\infty}{1 + a p_\infty / L} \tag{10.7}$$

where $p_\infty = 51.5(3)$nm is the persistence length value at infinite contour length, and $a = 2.78(12)$ is a geometric factor.

For that reason, we explore the possibility that also the Young modulus depends on the length of the molecules. To this aim, for each molecular length, we compute the value Y that better fits our experimental data as shown in Figure 10.6a. The results are shown in Figure 10.6b where the Young modulus is found to decrease for shorter molecules.

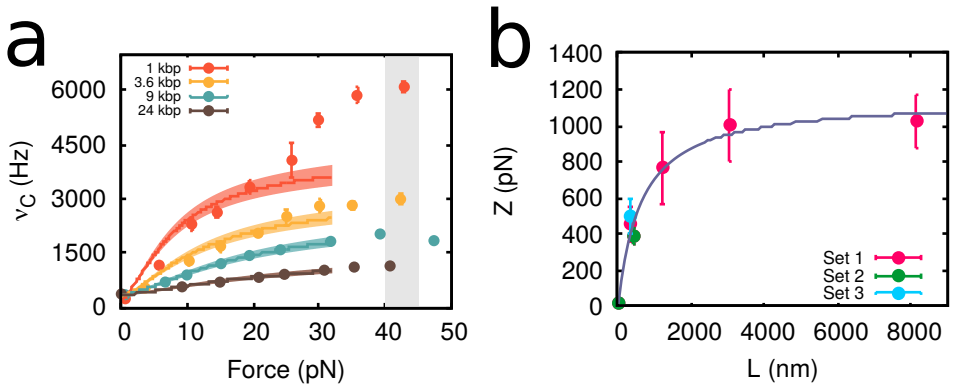

Figure 10.6: Young modulus' molecular length dependence. (**a**) Corner frequency versus force for the four different molecules taking into account the Young modulus dependence respect to molecular contour length. (**b**) Young modulus as a function of molecular contour length for the four different molecules (24kbp, 9kbp, 3.6kbp and 1kbp) in pink. Independent experimental studies with molecules of 1.3kbp and 58kbp [62] in green, and 1kbp [63] in blue are also shown.

For Y we use a relation similar to Eq. 10.7,

$$Y(L) = \frac{Y_\infty}{1 + bY_\infty/L} \tag{10.8}$$

where Y_∞ is the Young modulus for $L \to \infty$, b is a numerical factor. The fitting parameters obtained by fitting Eq. 10.8 to our data are,

$$Y_\infty = (1150 \pm 60)\text{pN} \qquad \text{b} = (0.55 \pm 0.08)\text{nm/pN} \tag{10.9}$$

Notice that Y_∞ is compatible with the values usually reported in literature [64]. Moreover, in Figure 10.6b it is possible to notice how the fitting curve perfectly agrees with the values of Young modulus reported in the literature for short molecules (58bp and 1257bp (Set 2) [62], 1000bp (Set 3) [63]).

10.3 Discussion and conclusions

The elastic properties of dsDNA have been extensively studied since the beginning of the investigation of single-molecule techniques in the 1970's (See Chapter 1 section 1.3). Most studies rely on measuring the FECs and fitting them to polymer models (such as the WLC model). However, the high resolution of Laser Optical Tweezers (LOT) setup and the noise measurement methodology, makes it possible to extract very accurate information about the molecular stiffness. In this chapter, we present noise measurments of the elastic properties of dsDNA molecules of different molecular length. We observe a significant deviation between our experimental data and the extensible worm-like chain model predicted values. This discrepancy shows a strong dependence on the molecular length, being negligible for longer molecules and large for shorter ones. Therefore, the discrepancy introduces a novel length dependence feature on the theoretical model. We interpret this disagreement by introducing a length dependence in the Young modulus. By letting the Young modulus change, we have observed a decrease of Y values for shorter molecules. These results are suportted by other independent experimental studies using LOT [52, 62], and magnetic tweezers [63].

We have proposed an analytical formula for the length dependence of the Young modulus following the one reported for the persistence length [61]. This expression is in excellent agreement with our experimental data and the results of other studies.

10.4 Future Perspectives

The exWLC model fails to reproduce the FECs of dsDNA above $\sim$ 30pN. The discrepancy between the experimental data and the model is due to the twist-stretch coupling contribution which, above 30pN, has to be taken into account. In 2011 , Gross et al. derived an expression of the twistable WLC model for high forces [6],

$$x_{tWLC}(f) = L_c \left(1 - \frac{1}{2}\sqrt{\frac{k_B T}{fp}} + \frac{C}{SC - g(f)^2} f \right) \tag{10.10}$$

where $L_c = N_{bp} \cdot 0.34 nm/bp$ is the contour length, p is the persistence length (Eq. 10.7), $C = 440\text{pN} \cdot \text{nm}^2$ is the twist rigidity, $S = 1500\text{pN}$ is the stretching modulus, and $g(f)$ is the twist-stretch coupling expressed as,

$$g(f) = g_0 + g_1 f \tag{10.11}$$

where $g_0 = -637\text{pN} \cdot \text{nm}$, $g_1 = 17\text{nm}$, and,

$$g(f) = \begin{cases} g(30) & f < 30 \\ g_0 + g_1 f & f \geq 30 \end{cases} \tag{10.12}$$

Notice that $g(f)$ has a constant value for $f < 30\text{pN}$, and for $f > 30\text{pN}$, it increases linearly with force. In Figure 10.7a, we compare the experimental corner frequency (colored points) with the predicted one ($\nu_c = k_b + k_m/(2\pi\gamma)$) computing k_m from Eq. 10.10 (solid lines). The presence of a maximum in the corner frequency represents a significant improvement of the tWLC respect to the exWLC. This maximum emerges from the fact that the tWLC is able to reproduce the change of concavity of the FEC. Moreover, the discontinuity observed in the 1kbp case around 30pN is compatible with the discontinuity predicted

by the tWLC. Nevertheless, the tWLC also fails to reproduce our experimental data.

Imposing the length-dependent Young modulus values to the tWLC, we obtain the results shown in Figure 10.7b. Although the model reproduces the experimental data for $f < 30$pN, above 30pN, the model diverges for the shorter molecules (1kbp and 3.6 kbp).

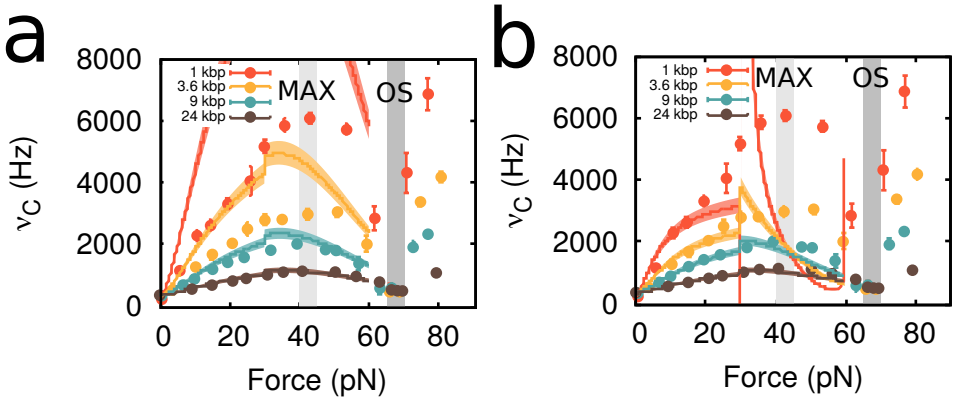

Figure 10.7: Twistable WLC. Corner frequency versus force together with the twistable-WLC fit (Eq. 10.10). Overstretching regime (OS) represented as a vertical dark grey band and maximum of the experimental data (MAX) in a light grey band. (**a**) Twistable-WLC model considering a constant stretching modulus $S = 1500$pN. (**b**) Twistable-WLC model considering a length dependent stretching modulus.

Comparing the exWLC with the high forces approximation of the tWLC (Eq. 10.10), we observe that the term multiplying the force, $1/(S - g(f)^2 C)$ can be treated as the inverse of an effective Young modulus $Y_{eff} = S - g(f)^2 C$. The decreasing of the Young modulus for short molecules observed in Figure 10.6b has two interpretations being the first one the one explored in this chapter: the stretched modulus decreases for shorter molecular lengths, $S(L)$, while the twist-stretch coupling only depends on the force $g(f)$. The second one assumes a constant stretched modulus S and a twist-stretched coupling that increases for shorter molecular lengths $g(f, L)$. In this case, it will be necessary to understand which term of the twisting-stretch coupling (g_0 or g_1, or both) presents the length dependence and which is the corresponding analytical expression $g(f, L)$. However, it is still needed a detailed study to validate this hypothesis.

Part VI

Conclusions

What is life and how does it works are the fundamental questions of biophysics. In the second half of the last century, non-equilibrium physics suffered a fructify revolution leading to information theory, complex systems, chaos theory, etc. These new theories faced the challenge of going a step forward in the characterization of living matter. Life operates far from equilibrium in the limit of chaos. In this non-linear regime, small perturbations could lead to large responses minimizing the amount of energy needed to accomplish a specific function. Therefore, the study of living systems fluctuations is vital in understanding and predicting non-linear life processes.

In this thesis, we employ noise-correlation force spectroscopy measurements using LOT to extract valuable information about the passive and active fluctuations of DNA molecules and red blood cells. We have chosen the laser optical tweezers (LOT) as the experimental setup because of its high resolution in both displacement ($\sim$ 1nm) and force ($\sim$ 0.1pN), and its versatility that allows us to measure DNA molecules and red blood cells (RBC).

In the Part I of this thesis, we introduce a biological framework for molecular and cellular systems. In particular, we summarize the biological function of nucleic acids and red blood cells together with a detailed explanation of their structure and composition. Moreover, we introduce the general concepts of polymer models by showing their analytical force-extension expression and specifying the polymers that better fit each model.

In the Part II, we introduce the noise measurements using LOT. First, we derive the expression for the power spectrum of a bead captured in an optical trap by performing the Fourier transform of its position correlation function. The analytical formula for the power spectrum allows us to fit the friction coefficient and the trap stiffness of the bead. In particular, this methodology can characterize the hydrodynamic effects of surface-bead and bead-bead proximity that increase the value of the friction coefficient. This result has to be taken into account when working with short molecules as DNA hairpins.

In the Part III, we study the mechanical deformability and active processes of RBC. We perform pulling experiments by stretching the RBC at a constant velocity from zero to 20pN force. The pulling curve characterizes the RBC stiffness and viscoelasticity. Moreover, we measure the stiffness change during membrane tether extrusion/retraction

quantifying the RBC configurational changes and defining two populations of RBC: tethered and untethered. In terms of the relaxation experiments, we perform four protocols characterized by the sign of the extension-jump (tensional or compressive) and the shape of the stepwise jump. Independently of the protocol or the population, we observed three relaxation processes, each defined by an amplitude and a relaxation time. The amplitudes show a linear dependence with force jump while the relaxation times have a constant value. The recovery force after the relaxation also shows a linear dependence with the force jump. However, each population presents a different slope, with a lower value for the untethered case. As the recovery force expected for purely elastic systems should be zero, the larger value for the tethered case indicates that this element introduces an extra viscous contribution to the RBC system. The results demonstrate that RBC exhibits three well-separated timescales spanning three orders of magnitude with a novel kind of stress and strain relaxational behavior that we call discrete-stretched exponential behavior. This new relaxation response is intermediate between the pure exponential relaxation observed in linear and two-level systems and the more complex stretched-exponential relaxation observed in polymers and glassy matter. As future work, we plan to perform relaxation experiments with disrupted RBC by depleting ATP or removing the 2D network to understand each element's contribution to both amplitudes and relaxation times.

In addition, we have introduced a soft-glass rheology model (the disordered blobs model) that reproduces the experimental RBC pulling and force relaxation curves measured with LOT. Moreover, the worm-like chain (WLC) model describes the force generated by the RBC and the stress behavior in continuous strain deformation (pulling) and strain jump deformation (relaxation) experiments. We have explored different initial distributions of the distances, x_i^m and $x_i^\dagger$, and the energies, $b_{i,0}$ and $\Delta g_{i,0}$ (Homogeneous, Gaussian and exponential). The combination of distance Gaussian distributions with exponential energy distributions is required to reproduce the pulling experimental curves. However, small deviations of these distributions can substantially change both the pulling and the relaxation curves. In the case of relaxation simulations, we recover the experimental linear relation between the pair of values ΔF_{rec} and ΔF. Moreover, the slope of the

linear relation is compatible with the untethered RBC as expected.

To measure the active processes ongoing on RBC fluctuations at rest, we measure a 60s force signal at a high sampling frequency ($\sim 50kHz$) at different trap stiffnesses. For each trap stiffness force singal the force signal at a specific trap stiffness, we compute the variance for five different time windows: 10s, 5s, 1s, 0.1s, and 0.01s. We divide the force signal in N sub-signals for each time window, being N the ratio between the trace duration and the time window. Then, the force variance for each time window is computed by averaging the variances of the N sub-signals. Once we compute the force variance from the equipartition theorem, we develop two methods to quantify the non-equilibrium effects and activity of the RBCs. In the first method, we express the force variance in terms of the inverse of the trap stiffness and fit a quadratic relation, being the numerical factor of the quadratic term the RBC stiffness. Therefore, the RBC viscoelasticity is characterized at each time window. In the second method, we compute the effective temperature of the RBC, assuming a constant RBC stiffness obtained from the pulling experiments. Both methods recover equilibrium for large values of k_b and present deviations as k_b decreases indicating the presence of active processes. In terms of viscoelasticity, we observe a softening of the RBC as the time window grows while the ratio between the effective temperature and the environmental one increases with the time window. We also propose to perform passive measurements with RBC under force. Preliminary results from power spectra analysis show promising deviations that could be related to RBC activity.

In the Part IV, we derive a new variance relation derived from the FDT, that holds for systems of N particles at non-equilibrium steady states subjected to arbitrary potentials. Moreover, this relation introduces for the first time two upper bounds to the entropy production rate. We also present a stochastic switching trap (SST) solvable model that returns an exact expression to quantify the entropy production rate. From an experimental point of view, we have studied three different systems: a single bead captured in an optical trap with and without flow, a CD4 hairpin in its folded and unfolded states, and a single bead optically trapped in a NESS achieved by randomly moving the trap between two positions separated by an amplitude $\Delta\lambda$ with a lifetime of τ_e at each trap position. From the single bead in the

optical trap case, we observe how the variance sum rule holds with and without flow as expected. Moreover, we recover compatible values for the trap stiffness and the friction coefficient of the bead with respect to the ones obtained by the FPS analysis. In the molecular case, we also obtain realistic values for the system stiffness and the friction coefficient. However, we observe a discrepancy for large times that we associate with the micropipette drift. In the SST protocol, the results show a deviation from equilibrium as expected, which we can quantify by computing the entropy production rate. Finally, we present preliminary results on the variance sum rule for RBC that does not present any deviation; however, the presence of the flow increases both trap stiffness and friction coefficient values.

In the Part V, we study the elastic properties of dsDNA molecules of different molecular lengths by measuring the fluctuations of the force. By computing the power spectrum of the force signal, we distinguish three processes at low, intermediate, and high-frequency regimes, which we identify as pink noise, axial fluctuation, and dsDNA fluctuations, respectively. Focusing on the high-frequency regime that characterized the molecules' elastic response, we observe a significant deviation between our experimental data and the extensible worm-like chain model predicted values. This discrepancy shows a strong dependence on the molecular length, negligible for longer molecules and large for shorter ones. Therefore, the discrepancy introduces a novel-length dependence feature on the theoretical model. We interpret this disagreement by introducing a length dependence in the Young modulus. By letting the Young modulus change, we have observed a decrease of Y values for shorter molecules. We have proposed an analytical formula for the length dependence of the Young modulus following the one reported for the persistence length. This expression is in excellent agreement with our experimental data and other independent experimental studies using LOT and magnetic tweezers.

Part VII

APPENDICES

Appendix A

Microfluidic chamber preparation

In this appendix, the steps to prepare the microfluidic chamber utilized in the Mini-tweezers experiments are described. In detail, the steps to prepare the chamber are:

1. The entrance and exit holes are drilled in one of the glass coverslips using a laser cutter. The coverslips are cleaned with a solution of 70% ethanol (although 100% ethanol can also be used, a 70% solution is preferred because it prevents the sporulation of some microorganisms).

2. The three channels are drawn in the two parafilm layers using a laser cutter.

3. One parafilm layer is attached on the drilled glass coverslip.

4. A glass micropipette with a diameter of $\sim 1\,\mu m$ is produced by heating and pulling a glass tube (King precision glass, Inc., inside diameter=$0.04\,mm$, outside diameter=$0.08\,mm$, length=$6.00\,mm$, glass type KG-33), as described in section A.1.

5. This glass micropipette is placed on top of the parafilm layer perpendicular to the channels with the tip positioned in the central channel, as shown in Figs. A.1a and A.1b.

6. The upper and lower channels are connected to the central one via glass dispenser tubes (King precision glass, Inc., inside diameter=$0.04\,mm$,

outside diameter=0.10 mm, length=6.00 mm, glass type KG-33) cut using a diamond-tip cutter to obtain a clean cut.

7. The second parafilm layer is placed on top and the chamber is closed using the second glass coverslip (previously cleaned with 70% ethanol), as shown in Fig. A.1b.

8. The chamber is sealed by heating it on a hot plate at 120°C while exerting a pressure of about 1 Kg in all the chambers' surface (either by placing a weight on top of the microfluidics chamber or, more simply, by exerting pressure by hand). To prevent the glass from breaking, it is recommended to sandwich the chamber between two thicker glass slides to homogenize the pressure applied to their surfaces.

9. The chamber is placed in the metallic mount. The correct alignment between the holes drilled in the glass coverslip and the holes in the mount is critical to ensure the flow in the chamber. It is also very important to tighten the screws to avoid buffer losses between the plastic tubes and the glass chamber, since this would cause flows inside the chamber. Do this carefully, because tightening the screws too much could break the glass coverslip.

10. The side of the micropipette coming out of the chamber is cut to get rid of the excess tube, leaving only about $\sim 3\,cm$, and is introduced into a polyethylene tube (polyethylene tubing, Warner Instruments, PE-10/100; outside diameter = 0.61 mm, inside diameter = 0.28 mm). This tube is then fixed to the mount with tape. The pipette is easily breakable, so the tube needs to be placed as straight as possible. The connection is then sealed by using a special glue (Norland, NOA-61; UV Curing Optical Adhesives). The glue is placed between the the glass tube of the pipette and the polyethylene tube to fill the void outer space between tube and pipette via capillarity. After observing that the glue has entered into the tube, the UV-curation is performed by leaving the whole chamber for $\sim 25\,min$ under a UV lamp. Since the glue could reach the end of the glass tube of the micropipette and block it, the chamber has to be placed under the UV-radiation as fast as possible. After the curation, a syringe

($1\,ml$ Luer Lock, HSW SOFT-JECT U100 Insulin Henke Sass Wolf) is inserted using a needle (BD Microlance $30G \times 1/2$" – $0.30\,mm \times 13\,mm$) at the end of the tube to create suction on the tip of the micropipette.

11. The holes of the mount are connected with silicone-rubber tubes (Tygon 3350, Saint-Gobain, .031 ID X .093 OD X 50 FT TYGON 335) via nylon socket screws (Nylon set $8 - 32 \times 3/8$", Product-Components, previously drilling a hole with a number 45 drill bit, of 0.82"), as shown in Fig. A.1b. A segment of $\sim 20\,cm$ polyethylene tube (Polyethylene tubing, Warner Instruments, PE-50/100: outside diameter = $0.97\,mm$, inside diameter = $0.58\,mm$) is inserted into the silicone-rubber tubes. The three exit tubes are connected to a trash (any small plastic container with a capacity volume $\sim 100\,ml$), while the three entry channels are connected to a syringe using a polyethylene tube (Polyethylene tubing, Warner Instruments, PE-50/100: outside diameter = $0.97\,mm$, inside diameter = $0.58\,mm$) which is inserted into the silicone-rubber tubes on one end, and a needle (HSW FINE-JECT $23G \times 1$" – $0.6\,mm \times 25\,mm$).

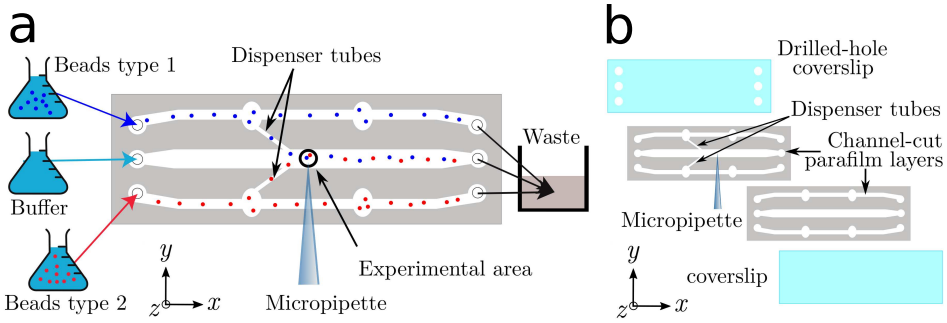

Figure A.1: Microfluidic chamber and channels. Schematic representations (**a**) of the microfluidics chamber (the flow goes from left to right, and the laser beams propagate perpendicularly to the surface of the chamber), (**b**) of the assembly procedure for the construction of the chamber,

A.1 Pipette making

A micropipette is used to hold a microparticle by air suction. The tip of this micropipette needs to have an inside diameter $\sim 1\,\mu m$, large enough to exert sufficient suction and small enough not to let the microparticles flow inside it. While one might use a commercial pipette puller to produce the pipettes, here, we will explain how a glass tube can be pulled to produce such micropipette using the homemade device shown in Fig. A.2 [17, 65].

This homemade pipette puller consists of a plastic platform with two parallel metallic bars, which hold a stage and along which a plastic weight can slide up and down. The two ends of the glass tube are fixed with screws to the stage and the weight, respectively. Thus, the

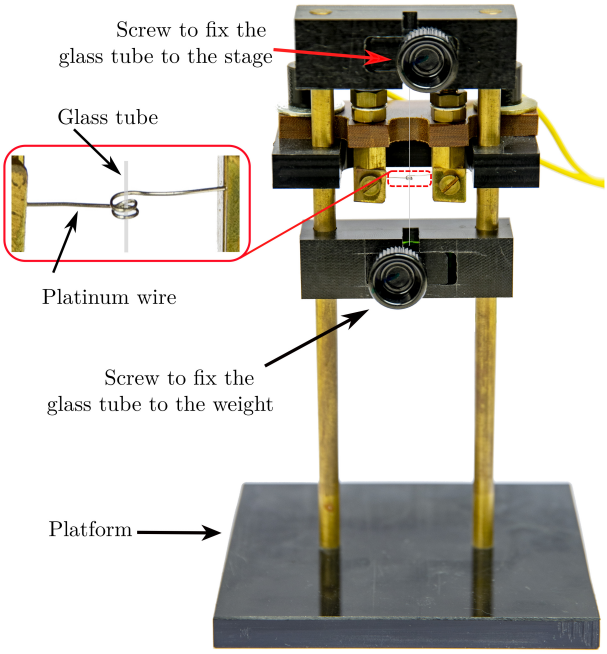

Figure A.2: Pipette puller. First, the glass tube is carefully centered within a coiled platinum wire, as shown in the inset. Then, one end of the tube is attached to the puller, while the other is attached to a weight that pulls the tube down. Finally, an electric current intensity ramp is applied through the platinum wire, heating the adjacent glass tube, which during the melting is pulled down, creating a micropipette.

glass tube is held in tension due to the pull exerted by gravity on the weight. The central part of the glass tube passes through a platinum wire; the two ends of the wire are connected to an electric supply, which provides a current ramp from 0 to $\sim 6\,A$ in $\sim 8\,s$. The exact maximum intensity and time of the ramp have to be tuned to get the appropriate diameter and shape of the pipette (in general, longer times and higher intensities correspond to smaller tips). Specifically, the steps required to produce a micropipette are:

1. Unplug the wire from the electric supply and place the pipette puller horizontally.

2. Insert the glass tube through the stage, the platinum coil, and the plastic weight.

3. Carefully center the glass tube within the platinum wire.

4. Screw the glass tube at the stage and plastic weight.

5. Place the platform vertically (as shown in Fig. A.2), carefully to avoid any sudden hit that may break the glass tube.

6. Apply the current ramp. The weight will drop into the platform. The geometry of the platinum wire is of a critical importance to obtain the proper shape and size of the micropipette. For that reason, when the weight drops into the platform, we have to ensure that the remaining glass tube of the stage is not touching the platinum wire, otherwise it would get stuck to it.

7. Unscrew the plastic weight and (with extreme caution and preferably with ethanol-cleaned tweezers) take the micropipette and place it into the chamber being built. The micropipette easily breaks or gets blocked by dust particles at the minimum contact of the tip of the glass tube with anything, so it needs to be handled with extreme care.

Appendix B

Preparation of the beads

In the following appendix, the preparation of the two types of beads used in single molecule experiments are detailed.

Biomolecules such as DNA, RNA and proteins are chains whose units are either nucleic bases or aminoacids [66]. These molecules can be conveniently manipulated through beads attached at their ends. Antigen-antibody connections can be used to attach a specific bead at each end, taking advantage of the fact that these connections are extremely specific [67]. In particular, avidin/streptavidin–biotin (streptavidin-biotin interaction is one of the strongest non-covalent interactions in Nature [68]) and digoxigenin–anti-digoxigenin connections are often employed in single-molecule force-spectroscopy experiments, because they can hold forces up to $\sim 100\,pN$ at typical optical-tweezers loading rates of $\sim 1\,pN\,s^{-1}$ [69].

Each bead is coated with a different molecule, which specifically binds to the cognate tails. Streptavidin-coated (SA) beads can be directly purchased (SPHERO streptavidin – polystyrene particles, $0.5\%\,w/y$, $2.17\,\mu m$, $5\,ml$). Anti-digoxigenin-coated (AD) beads are purchased as G-protein-coated polystyrene beads (Kisker Biotechnologies – G-coated polystyrene particles, $0.5\%\,w/y$, $3.18\,\mu m$, $5\,ml$), which must then be activated with anti-digoxigenin. The difference in size between these beads permits one to easily distinguish them by microscopy.

Buffers. The following buffers are required for the preparation of the beads:

PBS (pH 7.0) NaCl $0.14\,M$, KCl $2.7\,mM$, $K_2HPO_4 \cdot 3H_2O$ $61\,mM$,

KH_2PO_4 39 mM, NaN_3 (sodium azide) 0.02%. To prepare 50 ml: fill $\sim$ 40 ml of a 50 ml Falcon tube with Milli-Q water; add 0.406 g of NaCl, 0.01 g of KCl, 0.696 g of $K_2HPO_4 \cdot 3H_2O$, 0.265 g of KH_2PO_4, and 1 g of NaN_3; dissolve using a magnetic mixer; add Milli-Q water until reaching 50 ml; check the pH and add NaOH until the solution reaches a pH 7.0.

PBS (pH 7.4) NaCl 0.14 M, KCl 2.7 mM, $K_2HPO_4 \cdot 3H_2O$ 80.2 mM, KH_2PO_4 20 mM, NaN_3 (Sodium azide) 0.02%. For preparing 50 ml: follow the same procedure as for the previous buffer, adjusting to pH 7.4.

Antibody crosslinker buffer (pH 7.4) Na_2HPO_4 100 mM, NaCl 100 mM. To prepare 10 ml: fill $\sim$ 7 ml of a 10 ml Falcon tube with Milli-Q water; add 0.142 g of Na_2HPO_4 and 0.058 g of NaCl; shake well until the salts have dissolved; add Milli-Q water until the 10 ml of total volume is reached; check the pH and add NaOH until the solution reaches pH 7.4.

All salts can be acquired from any chemical distributor (e.g., Sigma Aldrich). All products have to be of a biomolecular grade of purity. The water for preparing all buffers has to be Milli-Q water. Milli-Q water is obtained by filtering the source water (usually distilled water) first through mixed bed ion exchange and organics (activated charcoal) cartridges, and then through a filter which removes any intact organisms. Usually a UV lamp completes the purification process. For the RNA experiments, use RNAse-free water for all preparations (and make sure the pHmeter is also cleaned with RNAse-free water).

SA beads. For the already coated SA beads, the protocol consists in exchanging the buffer where they are preserved with PBS (pH 7.4). The procedure ($\sim$ 30 min) for the preparation of 1 ml of SA beads (which should be sufficient to perform experiments for several months) is:

1. Homogeneously resuspend the SA beads. To do so, place the container with the purchased particles into a vortex mixer for several seconds. An additional step of several seconds of sonication further improves the resuspension.

2. Take $1\,ml$ of the resuspended SA beads and place it in a new Eppendorf tube.

3. Centrifuge the Eppendorf tube at $10000\,rpm$ for $5\,min$. The dense SA beads will precipitate, while the buffer will float above them.

4. Extract the overnatant buffer and add $1\,ml$ PBS (pH 7.4). Mix the SA beads and buffer. Sonicate a few seconds and centrifuge at $10000\,rpm$ for $5\,min$, again. Extract the overnatant, resuspend in $1\,ml$ PBS (pH 7.4) and sonicate during several seconds. This step is performed to exchange the buffer.

5. Aliquote in 20 tubes ($50\,\mu l$ each). This allows for an optimal sterile preservation of the beads.

6. Store at $4°C$ for up to ~ 6 months.

AD beads. The protocol for the preparation of the AD beads consists of three steps: (1) exchange the preservation buffer; (2) attach the anti-digoxigenin to the G-protein; (3) exchange the crosslinking buffer. The procedure ($\sim 90\,min$) for the preparation of $1\,ml$ of AD beads (which should be sufficient to perform experiments for several months) is:

1. (The first time the anti-digoxigenin batch is dissolved.) Add $200\,\mu l$ of PBS (pH 7.4) to dilute the dry anti-digoxigenin (sheep polycolonal anti-dig antibody, Roche 1333 089).

2. Prepare the dimethyl pimelimidate (DMP) crosslinker buffer by mixing $50\,mg$ DMP and $200\,\mu l$ antibody crosslinker buffer (pH 7.4). The DMP crosslinker buffer needs to be freshly prepared every time the AD beads are synthesized.

3. Homogeneously resuspend the G-coated beads. To do so, place the container with the purchased particles into a vortex mixer for several seconds. An additional step of several seconds of sonication improves the resuspension.

4. Centrifuge at $5000\,rpm$ for $2\,min$. The dense beads will precipitate, while the buffer float above them.

5. Extract the overnatant buffer and add $1\,ml$ antibody crosslinker buffer (pH 7.4). Mix the beads and the buffer, sonicate for a few seconds, and centrifuge at $5000\,rpm$ for $2\,min$.

6. Repeat the previous step (washing) and resuspend within $1\,ml$ antibody crosslinker buffer (pH 7.4).

7. Add $60\,\mu l$ of anti-DIG antibody and $30\,\mu l$ of freshly dissolved DMP crosslinker buffer. The volume of added anti-DIG antibody will depend on the coating of the beads: it may need to be higher if the vendor supplies the beads with a higher density of coating. Nevertheless, the proportions of anti-DIG and DMP crosslinker buffer have to be preserved (2:1).

8. Tumble at room temperature for $60\,min$.

9. Centrifuge at $5000\,rpm$ for $2\,min$.

10. Wash twice with $1\,ml$ PBS (pH 7.0), resuspend with the same buffer, and sonicate during several seconds.

11. Aliquote in 20 tubes ($50\,\mu l$ each).

12. Store at $4°C$ for up to ~ 6 months.

Molecular buffer. A typical molecular buffer for DNA pulling experiments consists of $10\,mM$ Tris pH 7.5 (Trizma, Sigma Aldrich), $10\,mM$ EDTA (EDTA, Sigma Aldrich), $1\,M$ NaCl, and 0.01% NaN_3 (sodium azide, to avoid bacterial growth). TRIS is used in the formulation of buffer solutions in the pH range between 7.5 and 8.5, while EDTA is widely used for scavenging metallic ions, including divalent ones, which most enzymes need to be active. For this reason, it is widely used as a food preservative or stabilizer. In our case, it inactivates DNAses and RNAses, preventing nucleic acid degradation. To facilitate the molecular buffer preparation, it is convenient to prepare stocks of:

1 M Tris pH 7.5 Fill $\sim 40\,ml$ of a $50\,ml$ Falcon tube with Milli-Q water. Add $6.05\,g$ of Tris-HCl. Dissolve using a magnetic mixer. Add Milli-Q water until reaching $50\,ml$. Check the pH and add

a solution of 25% HCl until the solution reaches pH 7.5. For longer storage, a final auto-cleavage can be performed.

EDTA 0.5 M pH 8.0 Fill $\sim$ $40\,ml$ of a $50\,ml$ Falcon tube with Milli-Q water. Add $7.306\,g$ of EDTA. Add NaOH to the solution (the EDTA does not dissolve in water if pH<7.5). Dissolve using a magnetic mixer. Add Milli-Q water until reaching $50\,ml$. Check the pH and add NaOH until the solution reaches pH 8.0.

5 M NaCl Fill $\sim$ $40\,ml$ of a $50\,ml$ Falcon tube with Milli-Q water. Add $14.49\,g$ of NaCl. Dissolve using a magnetic mixer and heat the tube to facilitate it. Add Milli-Q water until reaching $50\,ml$.

1% NaN_3 Fill $\sim$ $40\,ml$ of a $50\,ml$ Falcon tube with Milli-Q water. Add $0.5\,g$ of NaN_3. Dissolve using a magnetic mixer. Add Milli-Q water until reaching $50\,ml$.

After the stocks have been prepared, for preparing $50\,ml$ of the molecular buffer: Pour $\sim$ $30\,ml$ of Milli-Q water in a $50\,ml$ Falcon tube. Add $10\,ml$ of the $5\,M$ NaCl stock, $1\,ml$ of the $0.5\,M$ EDTA pH 8.0 stock, $0.5\,ml$ of the $1\,M$ Tris pH 7.5 stock, and $0.5\,ml$ of the 1% NaN_3 stock. Add Milli-Q water until reaching $50\,ml$ of volume. Mix the molecular buffer and filter it (Sterile Syringe Filter, $w/0.2\,\mu m$ Cellulose, Acetate Membrane, VWR International) introducing the filtered solution in a new $50\,ml$ Falcon tube.

Incubation of the beads. To finalize the preparation of the beads, incubate in an Eppendorf tube ($\sim$ $1.5\,ml$) $1\,\mu l$ of a solution of the biomolecule of interest(typically, the molecule is concentrated and needs to be diluted 1:10 to 1:100) mixed with $14\,\mu l$ of buffer (where the experiments are going to be performed) and $5\,\mu l$ of the previously prepared AD beads. After $\sim$ $25\,min$ have passed, add $1\,ml$ of the molecular buffer.

For the SA beads, no incubation is required, dilute $1\,\mu l$ of SA beads in $1\,ml$ of the molecular buffer in an Eppendorf tube.

Appendix C

Lasers alignment

In this appendix, we will detail the steps needed to align the two lasers in order to perform experiments with the Mini-tweezers device. Before any experiment, the setup needs to be aligned going through the following steps:

1. Remove any trapped object.
2. Move the chamber with the stepmotors so that the micropipette is a few micrometers away from the optical trap, in the so-called "working zone".
3. Remove any voltage applied to the piezoelectric motor.
4. Turn off the LED and remove the light filter, to be able to see the optical trap on the camera.
5. Decrease the laser power until it is possible to distinguish both lasers.
6. Using the screws of the kinematic mount, move the B laser (the one that has the real image shown on the screen) until it is superposed on the A laser.
7. Put back on the light filter, turn on the LED, and increase the laser power to its working value.
8. Set the current values recorded by the PSD as the zero force baseline along the x- and y-directions (center of the light spot) and along the z-direction (size of light spot).

9. Trap a bead with the optical trap by moving the chamber with the stepmotors close to the appropriate dispenser tube.

10. Bring the trapped bead to the working zone.

11. Fine-tune the alignment of the B laser using the screws of the kinematic mount controlling the wiggler of its fiber so that the xy-force signals from both force-PSDs are as close as zero as possible, i.e., both lasers exert an xy-force as close to zero as possible.

12. Fine-tune the position of one of the objectives along the z-directions so that the z-force from both force-PSDs is as close to zero as possible.

13. For both lasers, move the kinematic mount of the mirror that deflects the light that gets towards the position-PSD (between the aspherical lenses and the PSD) until its signal is zeroed (i.e., the light hits the center of the position-PSD).

Appendix D

RBC experiments using Mini-Optical Tweezers

Due to the biological laser damage [41] (section 4.2), some important considerations have to be taken into account when RBC experiments are performed using OT. In this appendix, the method to extract, suspend, trap and measure forces on RBC is detailed, and it corresponds, with few adaptations, to section 4.2 of the publication *Optical Tweezers - from calibration to applications: a tutorial* [70]. In particular, a pulling experiment is explained in order to present the analysis to obtain the force and the cellular extension from the Mini-Tweezers outputs.

D.1 Preliminary technical considerations

A very important issue to take into account when we are working with biological material is the physiological conditions. If the cell is not surrounded by the proper salt concentration, pH, temperature etc., different kinds of damage or even its death could be induced. Working with high focalized lasers, which are needed to create the optical trap, introduces another possible source of damage. This implies that we have to be very careful with the relative position between the cell and the optical trap in order to avoid the possible thermal- and photo-damage [41]. To minimize this damage, the cells can be trapped indirectly using optically trapped microparticles. This way, the laser is not in direct contact with the cell. Moreover, limiting the

laser power will also be necessary to prevent haemolysis (rupture of the RBC membrane) during our experiments. For instance, performing RBC experiments in a time window of $30\,min$, the maximum laser power that can be used without damaging the cell is $\sim 100\,mW$ [39].

D.2 RBC buffer preparation

The RBC buffer should mimic the physiological conditions found in human blood. It can be obtained as a solution of $130\,mM$ NaCl, $20\,mM$ K/Na phosphate buffer at $7.4\,pH$, $10\,mM$ glucose, and $1\,mg\,mL^{-1}$ BSA (Bovine Serum Albumin) [38]. It is convenient to prepare higher concentration stocks ($1\,M$) of every solution and store them in the fridge (higher concentration of salts together with low temperature will prevent microbial contamination), e.g., keeping them in $50\,mL$ falcon tubes for repeated use.

In the particular case of preparing a $50\,mL$ falcon tube containing the RBC buffer for the experiments, we should follow the next steps:

1. Add $6.5\,mL$ of $1\,M$ NaCl, $1\,mL$ of $1\,M$ K/Na phosphate buffer at $7.4\,pH$ [1] and $0.5\,mL$ of $1\,M$ glucose to an empty $50\,mL$ falcon tube.

2. Weigh $50\,g$ of BSA on a balance and add it to the falcon tube.

3. Add to the falcon tube $42\,mL$ of milliQ water.

4. Mix the RBC buffer and filter it (Sterile Syringe Filter, w/0.2μm Cellulose, Acetate Membrane, VWR International) introducing the filtered solution in another $50\,mL$ falcon tube.

All remaining unused RBC buffer in the experiments must be re-filtered again on a daily basis in order to prevent molecular aggregation or bacteria growing. After three days it is recommended to dispose of the RBC buffer because the re-filtering will not be enough to ensure proper conservation.

[1] The 1M K phosphate buffer at 7.4 pH is obtained by mixing 40.1 mL of 1M K2HPO4 and 9.9 mL of 1M KH2PO4. Note: For 1M Na Phosphate buffer at 7.4 pH, mix 38.7 mL of 1M Na2HPO4 and 11.3 mL of 1M NaH2PO4. All salts are available at Sigma-Aldrich.

D.3 Blood extraction

In order to obtain human blood, we will prick the finger of a healthy donor. Use of diabetic testing lancets will ensure sterilization of the pricking device. The extraction will be made following the next steps:

1. Disinfect the finger of the healthy donor with ethanol and dry it with handkerchief paper in order to remove any remaining liquid.

2. Prick the finger of the healthy donor with the lancet and apply some pressure on it to extract a drop of blood. A single drop of blood will be enough to perform experiments during an entire day.

3. With a $200\,\mu L$ pipette take $10\,\mu L$ of blood from the finger.

4. Dilute as fast as possible the drop in $1\,mL$ of RBC buffer inside a $1.5\,mL$ Eppendorf tube in order to prevent degradation of the RBCs.

D.4 Microparticle preparation

The simplest option to attach the microparticles to the RBCs is to take advantage of non-specific interactions between polystyrene microparticles and RBCs.[2] To do so,

1. Add $1\,mL$ RBC buffer in a $1.5\,mL$ Eppendorf tube.

2. Homogeneously resuspend the polystyrene microparticles. To do so, place the purchased Eppendorf of microparticles (Microbead NIST Traceable Particle Size Standard, 3.00μ, Polysciences, Inc.) into a vortex mixer for several seconds. An additional step of several seconds of sonication, improves the resuspension.

[2]There are several options to treat the microparticles and RBC to specifically attach them such as using the lectin protein Concanavalin A [32] or biotinylating the RBC [39]

3. Add $3\,\mu L$ of the microparticle stock solution to the Eppendorf tube.

It is recommended to have two Eppendorfs with microparticle solution available to ensure continued supply of the chamber with microparticles during the experiment.

D.5 Setup preparation

The experiment can be performed using the same microfluidic chamber employed for the single-molecule mechanics presented in section **??**. For this reason, we will follow the same procedure to build the chamber and to place it into the mount, as described in Section **??** . The only difference is that we will cut a larger plastic tube (40 cm) to connect one of the syringe to the entrance of the central channel. Once we have the chamber fixed into the mount with the syringes connected through the plastic tubes, we have to:

1. Flow $3\,mL$ of RBC buffer in each of the three channels in order to have an homogeneous environment in the chamber.

2. Identify which dispenser tube (upper/lower) has the most clear (the cut of the glass tube as perpendicular to the tube length as possible) exit to the central channel. This will facilitate the microparticles trapping.

3. Fill the syringe connected to the dispenser tube of the point 2) with the microparticles solution. More or less insert the half of the Eppendorf content to the syringe.

4. Fill the other syringe (upper/lower channel) with RBC solution. More or less insert the half of the Eppendorf content to the syringe.

5. Introduce the mount with the chamber between the two objectives of the LOT.

6. Connect the syringe with the larger plastic tube (the one of the central channel) to a pump in order to apply some controlled flow to the central channel when it is needed. We will use this

flow to separate the microparticle from the RBC and therefore prevent the possible thermal- and photo-damage of the cell.

D.6 Cell-bead configuration setup

In order to perform cellular pulling experiments, it is needed to orientate the cell to a certain cellular configuration. This configuration is represented in Fig. D.1(d). It consists in a RBC orientated vertically between two microparticles that are attached to the cell membrane on its opposites sides. The lower microparticle is immobilized by air suction of the pipette and the upper microparticle is held by the optical trap. It is important to emphasize that this procedure is created to minimize the direct exposition of the RBC to the laser. If we observe that at some point the RBC changes its shape we could assume that it has been damaged. In this situation we have to remove the cell and start over again. The procedure for obtaining the vertical configuration consists in the following steps:

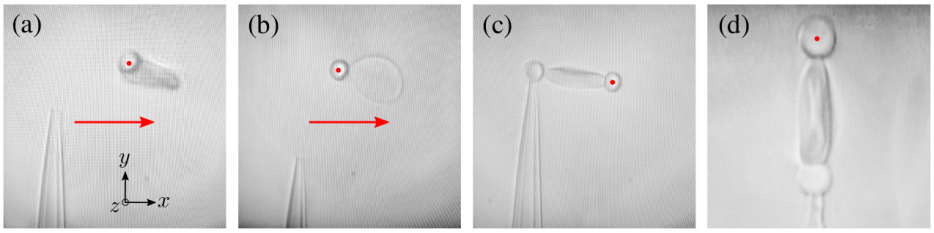

Figure D.1: Cell-bead configuration setup. Images of different steps to obtain the RBC configuration required for the experiment: (**a**) the RBC is attached to a bead and partially trapped by the lasers; (**b**) the bead is trapped, while the RBC is not trapped; (**c**) the second bead is attached to the other side of the RBC; (**d**) final experimental configuration at zero reading for the force along the y-direction. The diameter of the beads is $3\mu m$. The red dot represents the position of the optical trap. The red arrow in (a) and (b) represents the presence and direction of the fluid flow.

1. Align the lasers without a microparticle, as described in the first steps of Appendix C.

2. Identify the position of the pipette and the two dispenser tubes that connect the upper and the lower channels with the central one.

3. Move the chamber with the motors and place the optical trap close to the exit of the dispenser tube that contains the microparticle solution.

4. Flow some microparticle solution by hand (or with a pump connected to the syringe if you prefer) and try to trap a microparticle with the optical trap.

5. Move the trapped microparticle next to the pipette tip which will be the working zone.

6. Align the lasers with a microparticle, as described in the last steps of Appendix C.

7. Try different flow values with the pump connected to the syringe of the central channel until the force reaches $\sim$ 10pN due to the RBC buffer flow. This will be the approximate flow that we will need to separate the optically trapped microparticle from the RBC after we obtain an attachment.

8. Turn off the pump.

9. Move our trapped microparticle to the area of the blood dispenser tube exit. It is important to not put the microparticle exactly in the exit of the tube to prevent losing the microparticle due to the RBC solution flow.

10. Flow some RBC solution applying small pressure to the syringe by hand (or with a pump connected to the syringe if you prefer). RBCs will enter into the central channel.

11. Move the trapped microparticle close to a RBC and try to make a connection by touching the surface of the RBC with the microparticle.

12. The connection is formed when the RBC follows the trapped microparticle when moved.

13. Move the chamber motors to place the microparticle and the attached RBC next to the pipette.

14. Turn on the pump. The configuration should look like Fig. D.1(a). The RBC is attached to the microparticle and partially trap by the lasers.

15. If the flow is not enough to obtain the configuration of Fig. D.1(b), it will be necessary to move the motors in the horizontal direction to exert an extra X force and this way separate the RBC from the optically trapped microparticle.

16. Move the microparticle close to the tip of the pipette.

17. Carefully apply air suction to immobilize the microparticle. This step is critical because a large enough air suction force could absorb the RBC inside the pipette.

18. Move the optical trap away from the microparticle. If the microparticle is properly fixed to the tip of the pipette, the microparticle will stay there. If this is not the case, when the optical trap is moved the microparticle will follow it.

19. Do not turn off the pump flow on the central channel. In order to minimize the possibility of losing the microparticle attached to the RBC fixed on the tip of the pipette, do the following steps as fast as possible.

20. Decrease the flow in a factor of 2 to facilitate the trapping of the second microparticle. Check that the RBC stays separated from the microparticle, if this is not the case, increase the flow again to separate the cell from the microparticle.

21. Move the empty (without anything trapped, the microparticle is held by the pipette and RBC by the former) optical trap to the exit of the microparticle dispenser tube.

22. Flow microparticle solution and try to trap a microparticle. It will be harder due to the RBC buffer flow on the central channel. To catch a microparticle with the pump on, it is easier to stay at the exit of the dispenser tube without moving the trap. Wait for

the microparticle to fall into the optical trap instead of moving the trap around.

23. Once you have one microparticle trapped move the chamber to the pipette area.

24. Try to make a connection between the trapped microparticle and the RBC as in Fig. D.1(c). Notice that the two microparticles are in the opposite sides of the RBC.

25. Check that the new connection between the microparticle and the RBC is done by moving the optical trap to the same direction as the pump flow. If the RBC is deformed while moving the trap, the attachment is done.

26. Turn off the pump to remove the flow of the central channel

27. Nip very carefully the plastic tube that is connected to the entrance of the central channel with a clamp. This way there will not be flows due to the difference of pressure in both end of the plastic tubes.

28. Move the motors to obtain the vertical configuration of Fig. D.1(d). Try to get 0 pN force in Y direction.

D.7 Pulling Experiments

In this section we will explain how to mechanically stretch a RBC using a pulling protocol starting from the vertical configuration that we have obtained in the previous section. This vertical configuration consists of a RBC attached from opposites sides to two microparticles. The lower microparticle is immobilized in the pipette and the upper microparticle is optically trapped. We will move the optical trap in the vertical direction in order to move the upper microparticle and consequently, stretch the cell. This will allow us to obtain the force-extension curves from which we will extract the stiffness (deformability) of the RBC during the stretching and the releasing process. Pulling assays can be performed choosing the following parameters to define our stretching-releasing protocol:

1. Select the minimum force from which we will start stretching the RBC. In this case we choose 0 pN as the minimum force.

2. Select the maximum force at which the stretching of the cell will be interrupted in order to start the releasing process. In this case we choose a 20 pN maximum force.

3. Select the pulling velocity. In this case we impose 140 nm/s.

4. Select the refolding time which is the time window that the program will wait at the minimum force before starting a new cycle. In this case we take 0s as the refolding time.

Once we have selected these parameters, we will start the protocol from the final configuration of the previous section: the RBC vertically oriented with a 0 pN force in the Y axis. Starting from the minimum force, the RBC will be pulled at the constant pulling velocity until the maximum force. After reaching this maximum force, the RBC will be pushed at the same constant velocity to the minimum force. This circular process is called pulling cycle or trajectory.

Be aware that, depending on the laser power, it could be very hard to reach the 0 pN force as the RBC will be attracted to the optical trap. Above 20 pN, as we have not done any specific coating to the microparticle, it will appear a very thin membrane tube (tether) that will change our force-extension curves completely. As we are performing experiments with cells, take into account that you should have a range in your optical trap displacement of at least 8 μm. It is recommended to move the optical trap down, in the lower limit, before starting the pulling protocol. Recording 5 pulling cycles for each RBC will be enough. The magnitudes needed for the Data analysis will be Y force and Y trap displacement. In this particular single trap form by two counterpropagating lasers, we will have Y force and Y displacement for A trap and for B trap separately. We have to sum the forces but do the mean value of the displacements to obtain the correct values for total Y force and total Y displacement.

D.8 Data Analysis

Data analysis will consist in separate the different force-extension curves and compute the RBC stiffness knowing the stiffness of the optical trap. There are several ways to analyse pulling cycles.

1. Normally, the LOT user interface has the option to register the status during the protocols. In the pulling protocol the status will have a constant value for the stretching curves and a different constant value for the releasing curves. In this situation of having the status value, we simply have to identify which are the consecutive points that have different status value (we will call them changing points).

2. If we only have the values of the Y force, we have to identify which points are the ones that have the same value of the minimum and maximum force. In this case, these extreme force values will indicate the changing points.

Once we have identify the changing points, we will save in a different file each amount of points between two consecutive changing points. Following the experimental methodology explained in this section, the first file will contain the first stretching curve and the second file will contain the first releasing curve. In order to obtain a force-extension curve we have to represent a whole pulling cycle so one stretching and one releasing. It is recommended to plot the second pulling curve as the first one could present some especial behavior. For this reason we will plot the third and the fourth files which store the information for the second stretching and the second releasing curve.

In Fig. D.3(a) we present the force-cellular extension curve for the second pulling cycle for two different RBCs. Notice that in our experiment we measure trap displacement not cellular extension. Down below we will explain how to compute cellular extension from trap displacement and trap stiffness.

From schematics of Fig. D.2 we obtain the expression,

$$L = x_m + x_b \tag{D.1}$$

where L is the distance between the center of the microparticle attached to the tip of the pipette and the center of the optical trap,

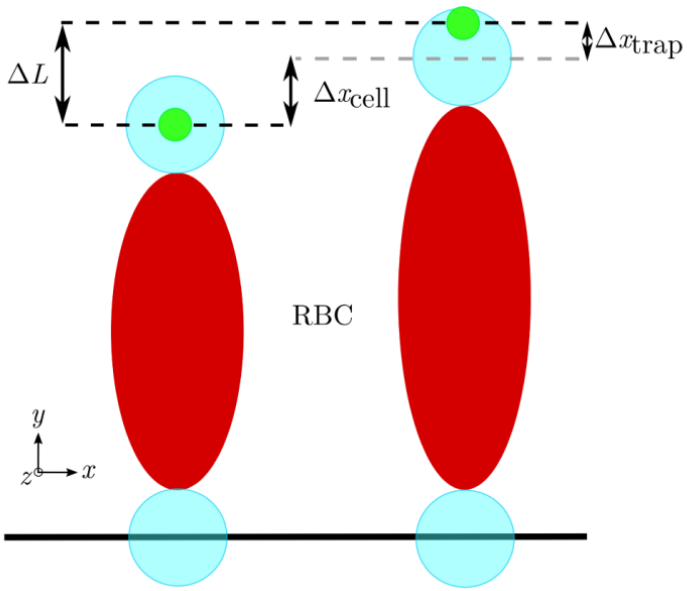

Figure D.2: Experimental configuration applying force. L is the distance between the center of the microparticle attached to the tip of the pipette and the center of the optical trap, x_m is the cell extension plus the microparticle diameter and x_b is the displacement of the center of the microparticle respect the center of the optical trap. The light blue circles represent the microparticles that is pulled by the same amount of force by the RBC and by the optical trap but in opposite directions.

x_m is the cellular extension plus the diameter of the microparticle and x_b is the displacement of the center of the microparticle respect to the center of the optical trap. Then, we divide equation D.1 by the force f applied to the microparticle by the RBC that is compensated by the optical trap,

$$\frac{L}{f} = \frac{x_m}{f} + \frac{x_b}{f} \tag{D.2}$$

As the stiffness of an object is defined as the force applied to it divided by its deformation, we are able to obtain the following relation,

$$\frac{1}{k_{Eff}} = \frac{1}{k_{RBC}} + \frac{1}{k_{trap}} \tag{D.3}$$

where k_{Eff} is what is called the effective stiffness of the system,

k_{RBC} is the RBC stiffness and k_{trap} is the stiffness of the optical trap.

Knowing the k_{trap} from tweezers calibration, we will be able to transform our measurement of trap displacement ($\Delta L = L2 - L1$) into change of cellular extension.

$$\Delta x_m = \Delta L - \Delta x_b \tag{D.4}$$

expressing x_b as a function of f and k_{trap} we finally obtain,

$$\Delta x_m = \Delta L - \frac{f}{k_{trap}} \tag{D.5}$$

the result of the force-cellular extension curve is shown in Fig. D.3(a).

From the force-extension curves we can extract the RBC stiffness by computing their slope. As can be observed in Fig. D.3(a), the force-extension curve it is not and straight line. This fact indicates that the stiffness of the RBC depends on the force applied to the cell. For this reason, we compute the slope for five different force windows which stiffness values are represented in Fig. D.3(b). The main conclusions that we can extract from Fig. D.3 are:

1. The stiffness of the RBC increases as we increase the applied force.

2. The stiffness curves of the stretching and realising cross each other between 6 pN and 10 pN.

3. The realising stiffness is higher than the stretching stiffness at high forces while is lower at low forces.

The dispersion between different RBCs, in terms of force-extension curves, can be huge. This is due to the fact that we are not separating RBC by density so RBC of different ages can be pulled [71]. Expected values for RBC stiffness in this specific geometry are in the range between 10 pN/μm and 3 pN/μm. Take into account that the pulling geometry can change in an order of magnitude the RBC stiffness values [32].

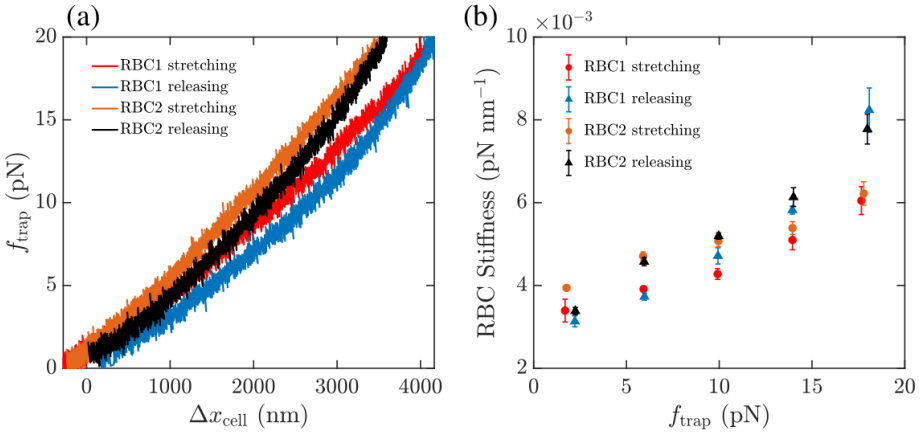

Figure D.3: RBC pulling experiments results. (**a**) FEC for two different RBCs. Each RBC is represented in a different color. Orange and red represent the stretching trajectory, and black and blue represent the corresponding realising trajectories. (**b**) Stiffness as a function of force obtained from the slope of the FEC in (a).

Appendix E

Equilibrium fluctuations

This appendix presents the mathematical derivation of the fluctuations at equilibrium for any object attached to a bead captured by an optical trap. This derivation has been used in Chapter 8 and 10.

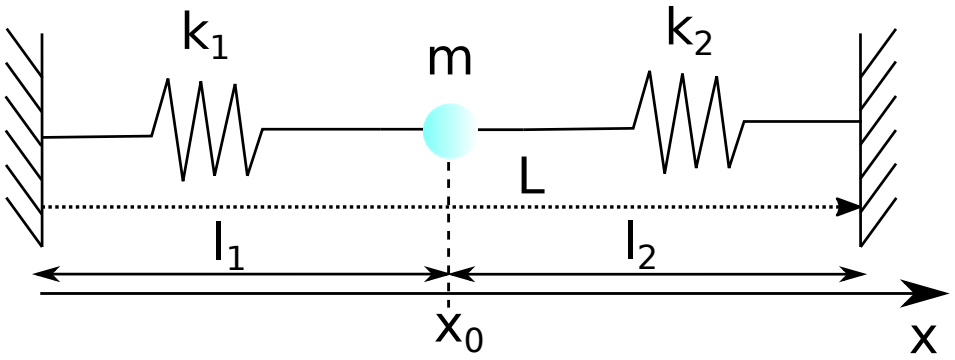

Figure E.1: Schematics of a bead between two springs at equilibrium. k_1 and k_2 are the spring stiffnesses, m is the mass of the bead, l_1 and l_2 are the extensions of the correspondig springs at equilibrium, x is the position of the bead (x=x_0 at equilibirum) and L is the distance between the fixed ends.

The force of the first spring assuming $x > l_1$ can be expressed as,

$$F_1 = -k_1(x - l_1) \tag{E.1}$$

For the second spring assuming $(L - x) > l_2$,

$$F_2 = k_2((L - x) - l_2) \tag{E.2}$$

So the total force applied to the is,

$$F_1 + F_2 = -k_1(x - l_1) + k_2((L - x) - l_2) \tag{E.3}$$

knowing that $L = l_1 + l_2$,

$$\begin{aligned} F_1 + F_2 &= -k_1(x - l_1) + k_2((l_1 + l_2 - x) - l_2) \\ &= -k_1(x - l_1) + k_2(l_1 - x) \\ &= -k_1(x - l_1) - k_2(x - l_1) \\ &= -(k_1 + k_2)(x - l_1) \end{aligned} \tag{E.4}$$

as the natural extension of the spring 1,l_1, is equal to the position of the mass at equilibrium x_0,

$$\begin{aligned} F_1 + F_2 &= -(k_1 + k_2)(x - x_0) \\ &= -k_T(x - x_0) \end{aligned} \tag{E.5}$$

then, the total stiffness (k_T) acting on the bead is the sum of the individual stiffness of each spring.

It is important not to confuse the total stiffness due to small fluctuations around equilibrium (k_T) with the effective stiffness (k_{eff}) obtained in the force extension curves explained on Appendix D.8.

Appendix F

Synthesis of dsDNA constructs

In this appendix, the steps to synthesize the dsDNA molecules to perform the noise experiments presented in Chapter 10 are detailed. The methods to build these four molecular constructs (24kbp, 9kbp, 3.6kbp, and 1kbp) are very similar. For that reason, in the first section it is explained the standard steps and the second one will be focused on the modulation of the molecular length.

F.1 Synthesis of dsDNA molecules

F.1.1 Comprehensive summary

The four dsDNA synthesis presented in this appendix start with the **digestion** of a linearized λ-DNA [1] (Fig. F.1, see also sections F.2.3, F.2.4, F.2.5 and F.2.6). In this first step, a restriction enzyme cuts the dsDNA molecule into different pieces. These enzymes can have single or multiple restrictions sites. We are only interested in one of the multiple segments generated by the restriction enzyme. In order to get

[1] Lambda (λ) is a large, temperate E. coli bacteriophage with a linear, largely double-stranded DNA genome. At each end, the $5'$ strand overhangs the $3'$ strand by 12 bases. These single-stranded overhangs are complementary and anneal to form a cos site following entry into a host cell. Once annealed, the genome is a circular, completely double-stranded molecule that serves as a template for rolling-circle replication [Restriction Maps, Lambda, *neb.com*].

rid of the rest of the dsDNA segments, a **purification** of the digested λ-DNA is required. The third step is the **tailing**, which consists in labeling the oligonucleotides with biotin and digoxigenin (both in 3' ends). This process allows the specific binding between the molecular constructs and the SA and AD beads (see Appendix B). Then, the **annealing** is performed, and the oligonucleotides (ssDNA) hybridize with the complementary sequences at the ends of the dsDNA segment of interest. In other words, the oligonucleotides form hydrogen bonds and become dsDNA with the ssDNA ends of the λ-DNA segment. The last step is the **ligation** reaction that joins, through two covalent phosphodiester bonds, the 3' hydroxyl group of one nucleotide and the 5' phosphate group of another. This way, all the pieces come together to obtain the dsDNA molecular construct.

A graphic scheme of all these five steps is shown in Fig. F.2.

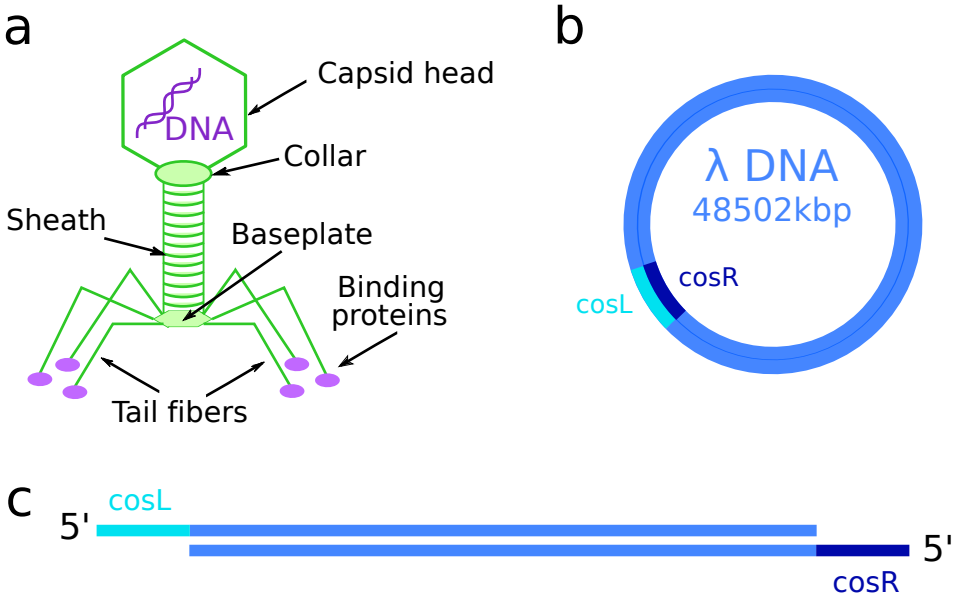

Figure F.1: Lambda-fage in its different forms. (**a**) Bacteriophage with its parts. (**b**) Circular plasmid of λ DNA where complementary cos sites (L from left and R of right) are represented with light and dark blue correspondingly. (**c**) Linearized λ DNA.

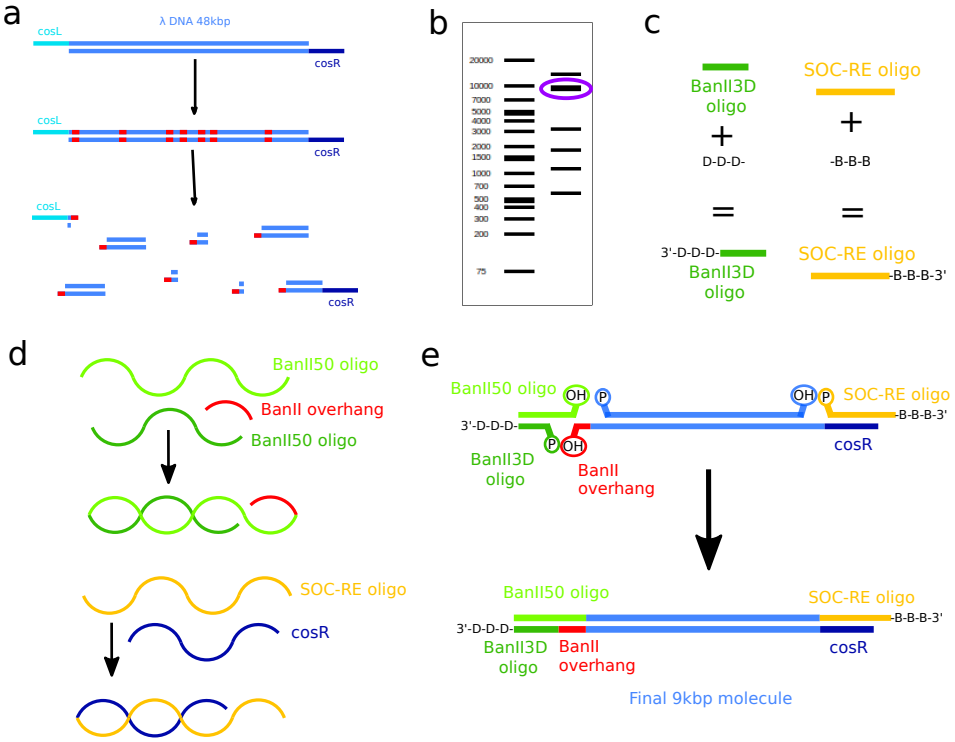

Figure F.2: dsDNA synthesis. (**a**) Digestion of the λ DNA with the restriction enzyme BanII where 8 segments are generated. (**b**) Gel electrophoresis where the fragment of interest (9kbp) is labeled with a purple circle. (**c**) Tailing of the oligonucleotides with digoxigenins and biotins. Each one of the oligos, corresponding to each one of the molecule ending, gets a different tailing to bind to each bead type specifically. (**d**) Annealing, formation of hydrogen bonds, of the oligonucleotides with the λ DNA segment (BanII overhang and cosR in this case). (**e**) Ligation reaction where the covalent bonds are formed to obtain the final dsDNA molecule.

F.1.2 Synthesis details

F.1.2.1 Digestion

The first step is the digestion, where the linearized λ -DNA (commercially available on New England Biolabs) is cut in different segments, depending on which restriction enzyme is used. The number of reactants needed and the time and temperature of the reaction are the following ones,

λ-DNA Digestion	
MiliQ water	62 μl
10X Reaction buffer	10 μl
100X BSA	1 μl
λ-DNA (0.5 $\mu g/\ \mu l$)	25 μl
Restriction enzyme	2 μl
Total volume:	100 μl
Incubate 3h at 37°C [2] [3]	

Table F.1: λ-DNA Digestion. Reactants, total final volume and time and temperature of the incubation.

F.1.2.2 Purification

There are two types of purification processes:

- **QIA PCR purification kit:** in this case everything except for DNA is removed from the sample. Therefore, all the digested segments remain in the solution. However, due to the tailing step, only the segment of interest will be attached to the beads during the experiments.

- **Gel purification:** in this case, we perform a gel, then we illuminate it with UV light, and, comparing the result with the gel electrophoresis scheme, we cut the segment of interest. Then, we perform a QIA gel purification kit to remove everything except from the segment of interest.

Hi ha dues maneres: o be 1) purificacio per gel (

[3]The temperature depends on the restriction enzyme. All the restrictions enzymes used in this appendix work at 37°C

[3]Notice that most of the restriction enzymes could be thermally inactivated by increasing the temperature to 65/80°C during 10'- 20' (the exact protocol appears in the technical details of the file). The thermal inactivation is recommendable as avoids the so called star activity (the restriction enzyme cuts randomly when the conditions are not ideals as change of temperature, salt concentration etc.).

F.1.2.3 Tailing

The third step consists in labeling the oligonucleotides with digoxigenin and biotin. The digoxigenin tailing will be performed to the oligonucleotide/oligo 1, and the biotin tailing will be performed to the oligonucleotide/oligo 2. Both reactions have to be incubated separately to ensure the specificity of each tailing type to the correct side.

Oligonucleotide 1 tailing reaction		Oligonucleotide 2 tailing reaction	
MiliQ water	8 μl	MiliQ water	8 μl
5X $CoCl_2$ solution	4 μl	5X $CoCl_2$ solution	4 μl
5X reaction buffer	4 μl	5X reaction buffer	4 μl
10mM dATP	1 μl	10mM dATP	1 μl
1 mM DIG-dUTP	1 μl	1 mM BIO-dUTP	1 μl
100 μM **oligonucleotide 1**	1 μl	100 μM **oligonucleotide 2**	1 μl
Terminal transferase (400U/μl)	1 μl	Terminal transferase (400U/μl)	1 μl
Total volume:	20 μl	Total volume:	20 μl
Incubate 15' at 37°C		Incubate 15' at 37°C.	
Quench reaction by adding 1 μl EDTA 0.5M.		Quench reaction by adding 1 μl EDTA 0.5M.	

Table F.2: Oligos tailing. Reactants, total final volume and time and temperature of digoxigenin and biotin tailing reactions of oligo 1 and oligo 2 correspondingly. A purification using QIA Oligonucleotide purification kit is performed to remove the dATP, DIG-dUTP, BIO-dUTP and the termnial transferase.

In order to stop these reactions, $1\mu l$ EDTA 0.5 M is added in each tailing and a purification step using the QIA Oligonucleotide purification kit is performed.

F.1.2.4 Annealing

Once the biotin and digoxigenin tailing are done, the annealing process is performed to attach the oligonucleotides to their complementary single-stranded DNA pieces on both endings of the dsDNA segment.

Annealing buffer:	
MiliQ water	890 μl
1 M Tris pH 7.5	100 μl(100 mM)
1 M $MgCl_2$	10 μl (10 mM)
Total volume:	1000 μl

Annealing of right-arm (biotin tag):	
oligo 2 biotin-tailed ($\sim$ 2 μM)	48 μl
oligo 3 (100 μM)	1 μl
Annealing buffer	5 μl
Total volume:	54 μl
1' at 95º and cool down from 80ºC to 10ºC in steps of 0.5ºC avery 10".	

Annealing of the molecular construct	
Digested λ-DNA (170 ng/μl)	40 μl
oligo 1 DIG-tailed ($\sim$ 2 μM)	5 μl
Annealing buffer	5 μl
Total volume:	50 μl
Incubate 10' at 72ºC. Add 10 μl of right-arm construct and incubate for 1h at 42ºC. Finally, let cool down to room temperature.	

Table F.3: Annealing reaction. Reactants and total final volume.

F.1.2.5 Ligation

The last step is the ligation reaction. The DNA ligase is responsible for forming the covalent bonds (3' hydroxyl group and 5' phosphate group) that will join the unconnected segments of ssDNA in both strands.

Ligation reaction:	
MiliQ water	7 μl
Annealing product	50 μl
10X T4 DNA ligase buffer	7 μl
10 mM ATP	3 μl
T4 DNA ligase (400 U/μl	3 μl
Total volume:	70 μl
Overnight reaction at 16°C	

Table F.4: Ligation reaction. Reactants and total final volume.

The overnight reaction, 10' at 65°C, thermally inactivate the ligase. After this step, the molecule can be safely stored in aliquots (usually of 1μm) and kept in the freezer.

F.2 Varying the molecular length

In this section, the procedure to synthesized a dsDNA molecule of a certain length is presented. In particular, four different examples are explained in detail.

F.2.1 Serial Cloner

The first step is to find a restriction enzyme that, incubated with λ-DNA, returns a fragment of the desire molecular length (for simplicity, the segment has to be attached on one of the two single-stranded ends of λ-DNA, cosR or cosL). *SerialCloner* is an OpenSource software that returns the output of the digestion of a certain molecule giving a specific restriction enzyme. In Fig. F.3, *SerialCloner* principal panel and Virtual cutter window are shown.

(a) Principal panel and acces to virtual cutter

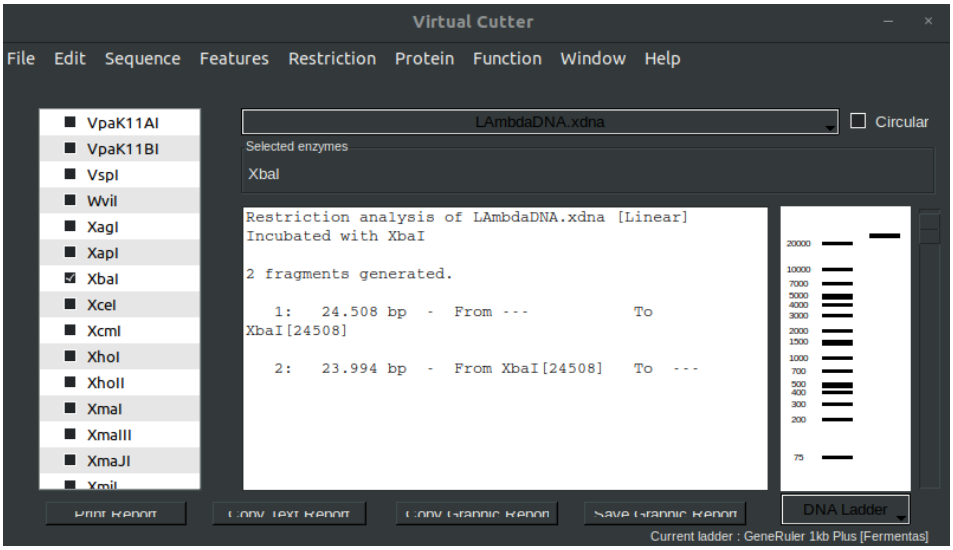

(b) Virtual cutter interface

Figure F.3: SerialCloner interface. (**a**) Principal panel with all the different windows. Virtual cutter in labeled with a red circle. (**b**) Interface of the virtual cutter window. On the top, the molecule to digest (LambdaDNA), on the left, the restriction enzymes library (XbaI), on the central panel, the specifications of the number (2) and molecular lengths (24508bp and 23994bp) of fragments obtained from the digestion reaction, and, on the right, a schematics of gel electrophoresis of the digested product.

Once the virtual cutter window is opened, the first step is to upload the sequence of the molecule that will be digested, in this case, *LambdaDNA.xdna*. Then, the restriction enzyme is selected, and the digestion product is shown as a summary of the molecular length of the λ-DNA fragments and a gel electrophoresis scheme.

F.2.2 Restriction enzymes and oligonucleotides

In this section, we specify how to synthesis the four molecular constructs. For this purpose, we show a figure with the output of the

SerialCloner software together with molecular synthesis schematics and a table with the sequence of the three oligonucleotides.

In order to synthesis a particular molecular construct, a restriction enzyme and three oligonucleotides are needed (Table F.5).

Important details to take into account:

- Notice that the **oligonucleotide name** is formed by three parts: 1) the name of the restriction enzyme, 2) the end of the DNA fragment they will be attached to (5' or 3'), and 3) the digoxigenin strand (D if they are attached to the digoxigenin strand an 0 if not). For example, **XbaI30** oligo is the oligonucleotide that will be used after digesting λ DNA with **XbaI**, it is located at the **3'** end and is **not** going to be tailed with any molecule.

- Notice that some oligonucleotides are phosphorylated, and others are not. After cutting the *lambda* DNA, all the restriction enzymes used in this section leave the 3' end with a hydroxyl group (OH) and the 5' end with phosphate (P). For that reason, the non-cut ends have to be previously phosphorylated.

Molecule	Restriction enzyme	oligo 1	oligo 2	oligo 3
24kbp	XbaI	SOC-LE	XbaI30	XbaI5D
9kbp	BanII	BanII3D	SOC-RE	BanII50
3.6kbp	EcoRI	EcoRI3D	SOC-RE	EcoRI50
1kbp	BspHI	SOC-LE	BspHI30	BspHI5D

Table F.5: Restriction enzymes and oligos for the 24kbp, 9kbp, 3.6kbp and 1kbp molecular constructs.

F.2.3 24kbp

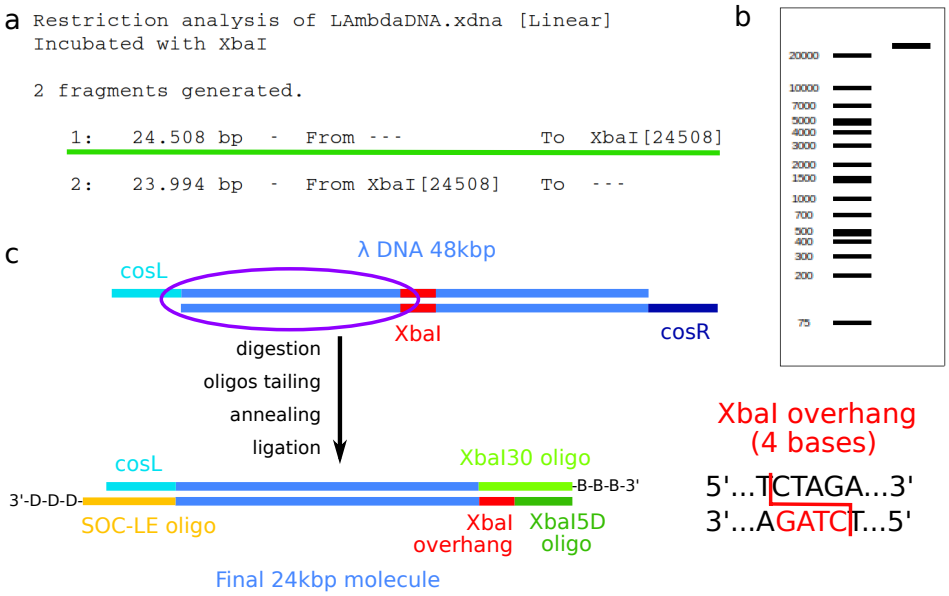

Figure F.4: XbaI restriction sites. (**a**) Outcome of SerialCloner software introducing the sequence of λ DNA and selecting XbaI as restriction enzyme. (**b**) Gel electrophoresis of the λ DNA incubated with XbaI. (**c**) Sketch of the linearized λ DNA with the restriction sites of XbaI.

24kbp	
Name	Oligonucleotide sequence
SOC-LE	5'-Pho-AGG TCG CCG CCC AAA AAA AAA AAA-3'
XbaI30	5'-Pho-**CTA GA**C CCG GGC TCG AGG ATC CCC-3'
XbaI5D	5'-GGG GAT CCT CGA GCC CGG GT-3'

Table F.6: Oligos sequence for 24kbp molecule. Notice that phosphorylation of the 5' is specified if needed. The complementary sequence of the restriction enzyme overhang is in bold.

F.2.4 9kbp

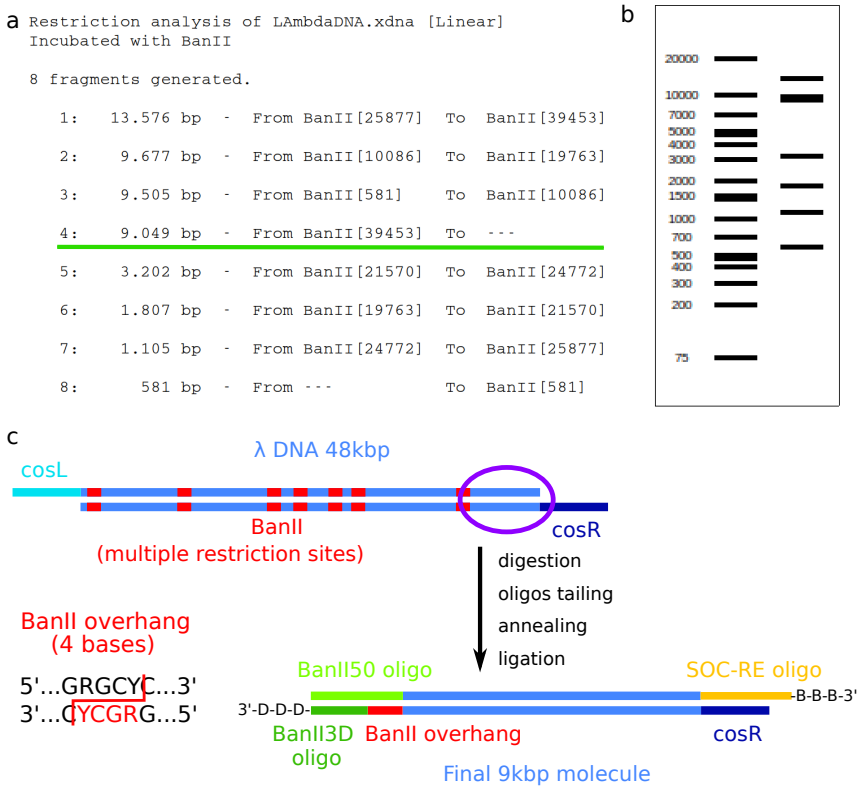

Figure F.5: BanII restriction sites. (**a**) Outcome of SerialCloner software introducing the sequence of λ DNA and selecting BanII as restriction enzyme. (**b**) Gel electrophoresis of the λ DNA incubated with BanII. (**c**) Sketch of the linearized λ DNA with the restriction sites of BanII.

9kbp	
Name	Oligonucleotide sequence
SOC-RE	5'-Pho-GGG CGG CGA CCT AAA AAA AAA AAA-3'
BanII50	5'-CCC CTA GGA GCT CGG GCC CA**R GCY**-3'
BanII3D	5'-Pho-TG GGC CCG AGC TCC TAG GGG-3'

Table F.7: Oligos sequence for 9kbp molecule. Notice that phosphorylation of the 5' is specified if needed. The complementary sequence of the restriction enzyme overhang is in bold.

F.2.5 3.6kbp

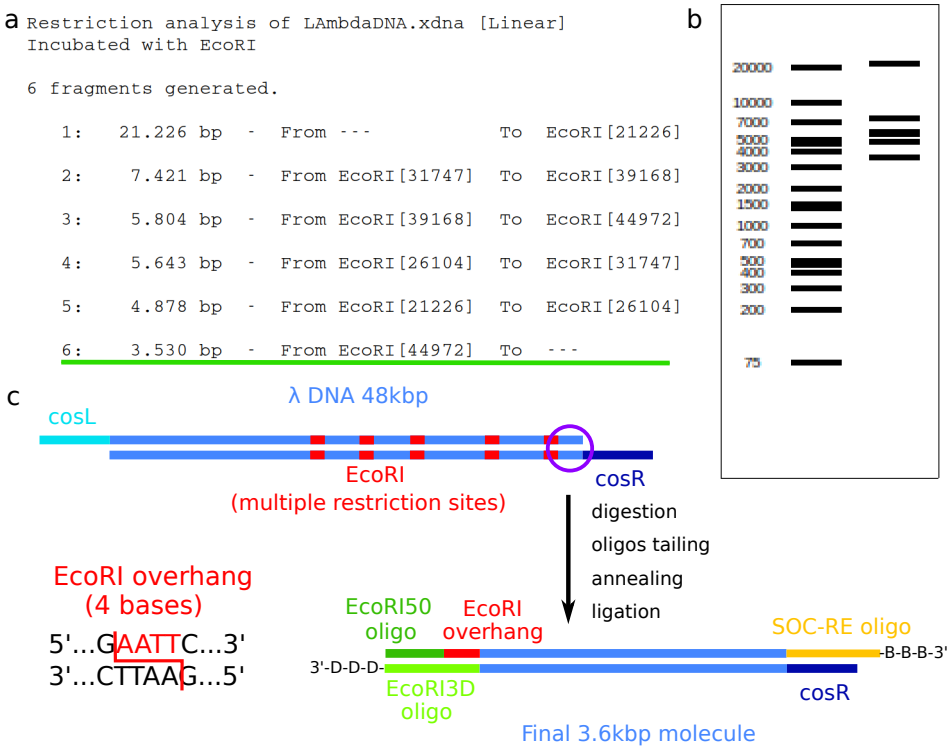

Figure F.6: EcoRI restriction sites. (**a**) Outcome of SerialCloner software introducing the sequence of λ DNA and selecting EcoRI as restriction enzyme. (**b**) Gel electrophoresis of the λ DNA incubated with EcoRI. (**c**) Sketch of the linearized λ DNA with the restriction sites of EcoRI.

3.6kbp	
Name	Oligonucleotide sequence
SOC-RE	5'-Pho-GGG CGG CGA CCT AAA AAA AAA AAA-3'
EcoRI50	5'-GGG GAT CCT CGA GCC CGG GT-3'
EcoRI3D	5'-Pho-**AAT T**AC CCG GGC TCG AGG ATC CCC-3'

Table F.8: Oligos sequence for 3.6kbp molecule. Notice that phosphorylation of the 5' is specified if needed. The complementary sequence of the restriction enzyme overhang is in bold.

F.2.6 1kbp

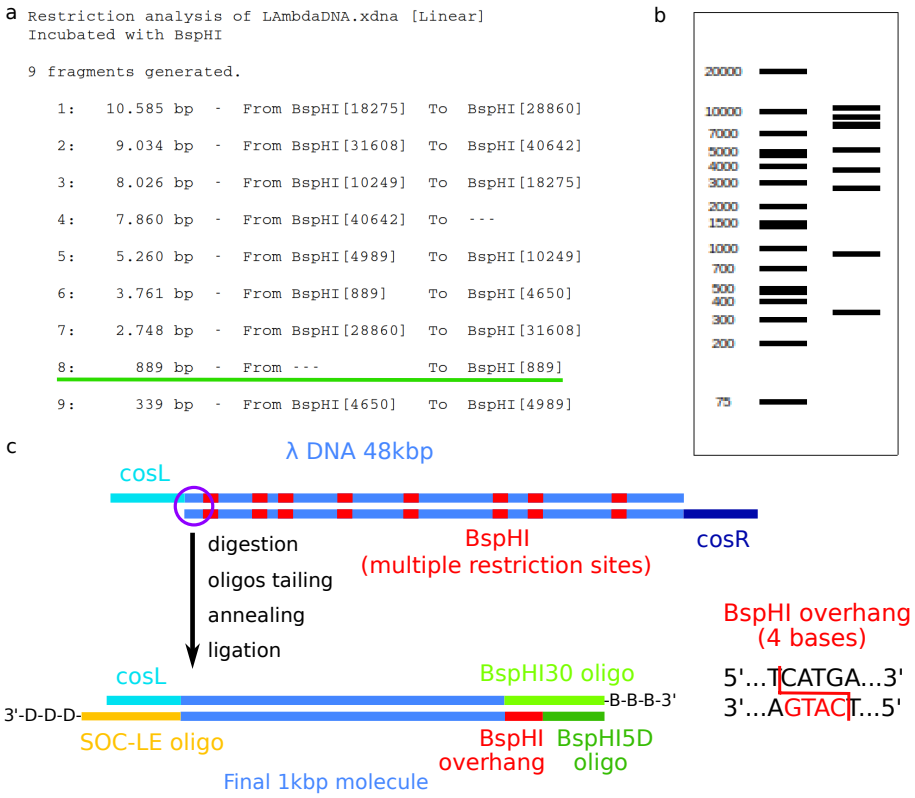

Figure F.7: BspHI restriction sites. (**a**) Outcome of SerialCloner software introducing the sequence of λ DNA and selecting BspHI as restriction enzyme. (**b**) Gel electrophoresis of the λ DNA incubated with BspHI. (**c**) Sketch of the linearized λ DNA with the restriction sites of BspHI.

1kbp	
Name	Oligonucleotide sequence
SOC-LE	5'-Pho-AGG TCG CCG CCC AAA AAA AAA AAA-3'
BspHI50	5'-Pho-**CAT G**AC CCG GGC TCG AGG ATC CCC-3'
BspHI5D	5'-GGG GAT CCT CGA GCC CGG GT-3'

Table F.9: Oligos sequence for 1kbp molecule. Notice that phosphorylation of the 5' is specified if needed. The complementary sequence of the restriction enzyme overhang is in bold.

Bibliography

[1] R. Schrodinger, E. Schrödinger, and E. S. Dinger, *What is life?: With mind and matter and autobiographical sketches*. Cambridge university press, 1992.

[2] H. F. Judson, *The eighth day of creation*. New York, 1979.

[3] F. Capra, *The web of life: A new synthesis of mind and matter*. Flamingo London, 1996.

[4] S. B. Smith, Y. Cui, and C. Bustamante, "Overstretching b-dna: the elastic response of individual double-stranded and single-stranded dna molecules," *Science*, vol. 271, no. 5250, pp. 795–799, 1996.

[5] J. F. Marko and E. D. Siggia, "Stretching dna," *Macromolecules*, vol. 28, no. 26, pp. 8759–8770, 1995.

[6] P. Gross, N. Laurens, L. B. Oddershede, U. Bockelmann, E. J. Peterman, and G. J. Wuite, "Quantifying how dna stretches, melts and changes twist under tension," *Nature Physics*, vol. 7, no. 9, pp. 731–736, 2011.

[7] W. Dean and M. O'Neill, "A slow motion of viscous liquid caused by the rotation of a solid sphere," *Mathematika*, vol. 10, no. 1, pp. 13–24, 1963.

[8] M. Cooley and M. O'NEILL, "On the slow rotation of a sphere about a diameter parallel to a nearby plane wall," *IMA Journal of Applied Mathematics*, vol. 4, no. 2, pp. 163–173, 1968.

[9] S. Kim and S. J. Karrila, *Microhydrodynamics: principles and selected applications*. Courier Corporation, 2013.

[10] A. Ashkin, "Acceleration and trapping of particles by radiation pressure," *Physical review letters*, vol. 24, no. 4, p. 156, 1970.

[11] A. Ashkin and J. M. Dziedzic, "Optical trapping and manipulation of viruses and bacteria," *Science*, vol. 235, no. 4795, pp. 1517–1520, 1987.

[12] A. Ashkin and J. Dziedzic, "Internal cell manipulation using infrared laser traps," *Proceedings of the National Academy of Sciences*, vol. 86, no. 20, pp. 7914–7918, 1989.

[13] K. Svoboda and S. M. Block, "Biological applications of optical forces," *Annual review of biophysics and biomolecular structure*, vol. 23, no. 1, pp. 247–285, 1994.

[14] E. J. Peterman, F. Gittes, and C. F. Schmidt, "Laser-induced heating in optical traps," *Biophysical journal*, vol. 84, no. 2, pp. 1308–1316, 2003.

[15] R.-J. Essiambre, "Arthur ashkin: Father of the optical tweezers," *Proceedings of the National Academy of Sciences*, vol. 118, no. 7, 2021.

[16] A. Ashkin, J. M. Dziedzic, J. E. Bjorkholm, and S. Chu, "Observation of a single-beam gradient force optical trap for dielectric particles," *Optics letters*, vol. 11, no. 5, pp. 288–290, 1986.

[17] S. B. Smith, Y. Cui, and C. Bustamante, "Optical-trap force transducer that operates by direct measurement of light momentum," in *Methods in enzymology*, vol. 361, pp. 134–162, Elsevier, 2003.

[18] M. Ribezzi-Crivellari, J. M. Huguet, and F. Ritort, "Counter-propagating dual-trap optical tweezers based on linear momentum conservation," *Rev. Sci. Instrumen.*, vol. 84, p. 043104, 2013.

[19] J. M. Huguet, *Statistical and thermodynamic properties of DNA unzipping experiments with optical tweezers*. PhD thesis, Universitat de Barcelona, 2010.

[20] L. Dean, "The abo blood group," in *Blood Groups and Red Cell Antigens [Internet]*, National Center for Biotechnology Information (US), 2005.

[21] R. S. Franco, "Measurement of red cell lifespan and aging," *Transfusion medicine and hemotherapy*, vol. 39, no. 5, pp. 302–307, 2012.

[22] J. Blom, *Monitoring of respiration and circulation*. CRC Press, 2003.

[23] G. B. Nash, C. S. Johnson, and H. J. Meiselman, "Mechanical properties of oxygenated red blood cells in sickle cell (hbss) disease," *Blood*, vol. 63, no. 1, pp. 73–82, 1984.

[24] J. M. Mauritz, A. Esposito, T. Tiffert, J. N. Skepper, A. Warley, Y.-Z. Yoon, P. Cicuta, V. L. Lew, J. R. Guck, and C. F. Kaminski, "Biophotonic techniques for the study of malaria-infected red blood cells," *Medical & biological engineering & computing*, vol. 48, no. 10, pp. 1055–1063, 2010.

[25] A. Vayá, R. Alis, M. Suescún, L. Rivera, J. Murado, M. Romagnoli, E. Solá, and A. Hernandez-Mijares, "Association of erythrocyte deformability with red blood cell distribution width in metabolic diseases and thalassemia trait," *Clinical hemorheology and microcirculation*, vol. 61, no. 3, pp. 407–415, 2015.

[26] M. H. Antonelou, A. G. Kriebardis, and I. S. Papassideri, "Aging and death signalling in mature red cells: from basic science to transfusion practice," *Blood Transfusion*, vol. 8, no. Suppl 3, p. s39, 2010.

[27] C. F. Arias and C. F. Arias, "How do red blood cells know when to die?," *Royal Society open science*, vol. 4, no. 4, p. 160850, 2017.

[28] S. Embury, M. Clark, G. Monroy, N. Mohandas, *et al.*, "Concurrent sickle cell anemia and alpha-thalassemia. effect on pathological properties of sickle erythrocytes.," *The Journal of clinical investigation*, vol. 73, no. 1, pp. 116–123, 1984.

[29] G. M. Artmann, K. Sung, T. Horn, D. Whittemore, G. Norwich, and S. Chien, "Micropipette aspiration of human erythrocytes induces echinocytes via membrane phospholipid translocation," *Biophysical journal*, vol. 72, no. 3, pp. 1434–1441, 1997.

[30] D. A. Fedosov, M. Peltomäki, and G. Gompper, "Deformation and dynamics of red blood cells in flow through cylindrical microchannels," *Soft matter*, vol. 10, no. 24, pp. 4258–4267, 2014.

[31] G. Ciasca, M. Papi, S. Di Claudio, M. Chiarpotto, V. Palmieri, G. Maulucci, G. Nocca, C. Rossi, and M. De Spirito, "Mapping viscoelastic properties of healthy and pathological red blood cells at the nanoscale level," *Nanoscale*, vol. 7, no. 40, pp. 17030–17037, 2015.

[32] R. Sorkin, G. Bergamaschi, D. Kamsma, G. Brand, E. Dekel, Y. Ofir-Birin, A. Rudik, **Gironella, Marta**, F. Ritort, N. Regev-Rudzki, *et al.*, "Probing cellular mechanics with acoustic force spectroscopy," *Molecular biology of the cell*, vol. 29, no. 16, pp. 2005–2011, 2018.

[33] M. Puig-de Morales-Marinkovic, K. T. Turner, J. P. Butler, J. J. Fredberg, and S. Suresh, "Viscoelasticity of the human red blood cell," *American Journal of Physiology-Cell Physiology*, vol. 293, no. 2, pp. C597–C605, 2007.

[34] G. Koster, M. VanDuijn, B. Hofs, and M. Dogterom, "Membrane tube formation from giant vesicles by dynamic association of motor proteins," *Proceedings of the National Academy of Sciences*, vol. 100, no. 26, pp. 15583–15588, 2003.

[35] F. Brochard and J. Lennon, "Frequency spectrum of the flicker phenomenon in erythrocytes," *Journal de Physique*, vol. 36, no. 11, pp. 1035–1047, 1975.

[36] H. Turlier and T. Betz, "Unveiling the active nature of living-membrane fluctuations and mechanics," *Annual Review of Condensed Matter Physics*, vol. 10, pp. 213–232, 2019.

[37] Y. Z. Yoon, J. Kotar, A. T. Brown, and P. Cicuta, "Red blood cell dynamics: from spontaneous fluctuations to non-linear response," *Soft Matter*, vol. 7, no. 5, pp. 2042–2051, 2011.

[38] T. Betz, M. Lenz, J.-F. Joanny, and C. Sykes, "Atp-dependent mechanics of red blood cells," *Proceedings of the National Academy of Sciences*, vol. 106, no. 36, pp. 15320–15325, 2009.

[39] H. Turlier, D. A. Fedosov, B. Audoly, T. Auth, N. S. Gov, C. Sykes, J.-F. Joanny, G. Gompper, and T. Betz, "Equilibrium physics breakdown reveals the active nature of red blood cell flickering," *Nature Physics*, vol. 12, no. 5, p. 513, 2016.

[40] J. C. Cluitmans, F. Gevi, A. Siciliano, A. Matte, J. K. Leal, L. De Franceschi, L. Zolla, R. Brock, M. J. Adjobo-Hermans, and G. J. Bosman, "Red blood cell homeostasis: pharmacological interventions to explore biochemical, morphological and mechanical properties," *Frontiers in molecular biosciences*, vol. 3, p. 10, 2016.

[41] R. Zhu, T. Avsievich, A. Popov, and I. Meglinski, "Optical tweezers in studies of red blood cells," *Cells*, vol. 9, no. 3, p. 545, 2020.

[42] Y.-Z. Yoon, J. Kotar, G. Yoon, and P. Cicuta, "The nonlinear mechanical response of the red blood cell," *Physical biology*, vol. 5, no. 3, p. 036007, 2008.

[43] S. Chikazumi and C. D. Graham, *Physics of Ferromagnetism 2e*. No. 94, Oxford University Press on Demand, 2009.

[44] J. Mills, L. Qie, M. Dao, C. Lim, and S. Suresh, "Nonlinear elastic and viscoelastic deformation of the human red blood cell with optical tweezers," *Molecular & Cellular Biomechanics*, vol. 1, no. 3, p. 169, 2004.

[45] M.-T. Wei, A. Zaorski, H. C. Yalcin, J. Wang, M. Hallow, S. N. Ghadiali, A. Chiou, and H. D. Ou-Yang, "A comparative study of living cell micromechanical properties by oscillatory optical tweezers," *Optics express*, vol. 16, no. 12, pp. 8594–8603, 2008.

[46] A. Lendlein and S. Kelch, "Shape-memory polymers," *Angewandte Chemie International Edition*, vol. 41, no. 12, pp. 2034–2057, 2002.

[47] J. M. Huguet, C. V. Bizarro, N. Forns, S. B. Smith, C. Bustamante, and F. Ritort, "Single-molecule derivation of salt dependent base-pair free energies in dna," *Proceedings of the National Academy of Sciences*, vol. 107, no. 35, pp. 15431–15436, 2010.

[48] G. Del Piero and L. Deseri, "Monotonic, completely monotonic, and exponential relaxation functions in linear viscoelasticity," *Quarterly of applied mathematics*, vol. 53, no. 2, pp. 273–300, 1995.

[49] Y. Yu, M. Wang, D. Zhang, B. Wang, G. Sant, and M. Bauchy, "Stretched exponential relaxation of glasses at low temperature," *Physical review letters*, vol. 115, no. 16, p. 165901, 2015.

[50] F. Ritort, C. Bustamante, and I. Tinoco, "A two-state kinetic model for the unfolding of single molecules by mechanical force," *Proceedings of the National Academy of Sciences*, vol. 99, no. 21, pp. 13544–13548, 2002.

[51] M. B. I. Di Terlizzi, M. Gironella and F. Ritort, "Variance sum rule for nonequilibrium systems," *In preparation.*

[52] N. Forns, S. de Lorenzo, M. Manosas, K. Hayashi, J. M. Huguet, and F. Ritort, "Improving signal/noise resolution in single-molecule experiments using molecular constructs with short handles," *Biophysical journal*, vol. 100, no. 7, pp. 1765–1774, 2011.

[53] A. Alemany, *Dynamic force spectroscopy and folding kinetics in molecular systems.* PhD thesis, Universitat de Barcelona, 2014.

[54] A. C. Barato and U. Seifert, "Thermodynamic uncertainty relation for biomolecular processes," *Physical review letters*, vol. 114, no. 15, p. 158101, 2015.

[55] P. Pietzonka, F. Ritort, and U. Seifert, "Finite-time generalization of the thermodynamic uncertainty relation," *Physical Review E*, vol. 96, no. 1, p. 012101, 2017.

[56] J. Camunas-Soler, A. Alemany, and F. Ritort, "Experimental measurement of binding energy, selectivity, and allostery using fluctuation theorems," *Science*, vol. 355, no. 6323, pp. 412–415, 2017.

[57] C. G. Baumann, S. B. Smith, V. A. Bloomfield, and C. Bustamante, "Ionic effects on the elasticity of single dna molecules," *Proceedings of the National Academy of Sciences*, vol. 94, no. 12, pp. 6185–6190, 1997.

[58] J. R. Wenner, M. C. Williams, I. Rouzina, and V. A. Bloomfield, "Salt dependence of the elasticity and overstretching transition of single dna molecules," *Biophysical journal*, vol. 82, no. 6, pp. 3160–3169, 2002.

[59] K. Berg-Sørensen and H. Flyvbjerg, "Power spectrum analysis for optical tweezers," *Review of Scientific Instruments*, vol. 75, no. 3, pp. 594–612, 2004.

[60] M. Ribezzi-Crivellari, A. Alemany, and F. Ritort, "Universal axial fluctuations in optical tweezers," *Optics letters*, vol. 40, no. 5, pp. 800–803, 2015.

[61] Y. Seol, J. Li, P. C. Nelson, T. T. Perkins, and M. Betterton, "Elasticity of short dna molecules: theory and experiment for contour lengths of 0.6–7 μm," *Biophysical journal*, vol. 93, no. 12, pp. 4360–4373, 2007.

[62] M. Ribezzi-Crivellari and F. Ritort, "Force spectroscopy with dual-trap optical tweezers: molecular stiffness measurements and coupled fluctuations analysis," *Biophysical journal*, vol. 103, no. 9, pp. 1919–1928, 2012.

[63] M. J. Shon, S.-H. Rah, and T.-Y. Yoon, "Submicrometer elasticity of double-stranded dna revealed by precision force-extension measurements with magnetic tweezers," *Science advances*, vol. 5, no. 6, p. eaav1697, 2019.

[64] C. Bustamante, S. B. Smith, J. Liphardt, and D. Smith, "Single-molecule studies of dna mechanics," *Current opinion in structural biology*, vol. 10, no. 3, pp. 279–285, 2000.

[65] U. di Parma, "Assemblies: Pipette Puller." `http://tweezerslab.unipr.it/cgi-bin/mt/assemblies.pl/Show?_id=7c1b`. [Accessed: 2019-12-12].

[66] P. Nelson, *Biological physics*. New York: WH Freeman, 2004.

[67] I. Sela-Culang, V. Kunik, and Y. Ofran, "The structural basis of antibody-antigen recognition," *Frontiers Immunol.*, vol. 4, p. 302, 2013.

[68] C. E. Chivers, A. L. Koner, E. D. Lowe, and M. Howarth, "How the biotin–streptavidin interaction was made even stronger: investigation via crystallography and a chimaeric tetramer," *Biochem. J.*, vol. 435, pp. 55–63, 2011.

[69] F. Pincet and J. Husson, "The solution to the streptavidin-biotin paradox: the influence of history on the strength of single molecular bonds," *Biophys. J.*, vol. 89, no. 6, pp. 4374–4381, 2005.

[70] J. Gieseler, J. R. Gomez-Solano, A. Magazzù, I. P. Castillo, L. P. García, **Gironella-Torrent, Marta**, X. Viader-Godoy, F. Ritort, G. Pesce, A. V. Arzola, *et al.*, "Optical tweezers—from calibration to applications: a tutorial," *Advances in Optics and Photonics*, vol. 13, no. 1, pp. 74–241, 2021.

[71] S. Piomelli and C. Seaman, "Mechanism of red blood cell aging: relationship of cell density and cell age," *American journal of hematology*, vol. 42, no. 1, pp. 46–52, 1993.

[72] I. Tadeo, E. Gamero-Sandemetrio, A. P. Berbegall, **Gironella, Marta**, F. Ritort, A. Cañete, G. Bueno, S. Navarro, and R. Noguera, "Lymph microvascularization as a prognostic indicator in neuroblastoma," *Oncotarget*, vol. 9, no. 40, p. 26157, 2018.

List of publications

- I. Tadeo, E. Gamero-Sandemetrio, A. P. Berbegall, **Gironella, Marta**, F. Ritort, A. Cañete, G. Bueno, S. Navarro, and R. Noguera, "Lymph microvascularization as a prognostic indicator in neuroblastoma," *Oncotarget*, vol. 9, no. 40, p. 26157, 2018

- R. Sorkin, G. Bergamaschi, D. Kamsma, G. Brand, E. Dekel, Y. Ofir-Birin, A. Rudik, **Gironella, Marta**, F. Ritort, N. Regev-Rudzki, *et al.*, "Probing cellular mechanics with acoustic force spectroscopy," *Molecular biology of the cell*, vol. 29, no. 16, pp. 2005–2011, 2018

- J. Gieseler, J. R. Gomez-Solano, A. Magazzù, I. P. Castillo, L. P. García, **Gironella-Torrent, Marta**, X. Viader-Godoy, F. Ritort, G. Pesce, A. V. Arzola, *et al.*, "Optical tweezers—from calibration to applications: a tutorial," *Advances in Optics and Photonics*, vol. 13, no. 1, pp. 74–241, 2021

List of abbreviations

Capital letters

T — Temperatura (K).

Lowercase

k_B — Boltzmann constant.
k_b — Trap stiffness.

Greek letters

Σ_f — Cumulative force.
γ — Friction coefficient.
ν — Frequency.

List of Acronym

Capital letters

AFM	—	Atomic Force Microscopy.
BC	—	Boxcar.
CW	—	Continuous Wave.
DBM	—	Disorder Blobs Model.
FPS	—	Force power spectrum.
FDC	—	Force distance curve.
FDT	—	Fluctuation-Dissipation Theorem.
FEC	—	Force extension curve.
FJC	—	Freely Jointed Chain.
FRC	—	Force relaxation curve.
NA	—	Numerical Aperture.
PBS	—	Phosphate Buffered Saline.
PCR	—	Polymerase Chain Reaction.
PSD	—	Position Sensing Detector.
RBC	—	Red Blood Cells.
SGM	—	Soft-glass mechanical.
SNR	—	Signal-to-Noise Ratio.
SST	—	Stochastic Switching Trap.
WLC	—	Worm-Like Chain.

Lowercase

bp	—	base pairs.
dsDNA	—	double stranded DNA.
ssDNA	—	single stranded DNA.